National Library of Canada
Acquisitions and Bibliographic Services Branch
395 Wellington Street
Ottawa, Ontario
K1A 0N4

Bibliothèque nationale du Canada
Direction des acquisitions et des services bibliographiques
395, rue Wellington
Ottawa (Ontario)
K1A 0N4

Your file Votre référence

Our file Notre référence

NOTICE

The quality of this microform is heavily dependent upon the quality of the original thesis submitted for microfilming. Every effort has been made to ensure the highest quality of reproduction possible.

If pages are missing, contact the university which granted the degree.

Some pages may have indistinct print especially if the original pages were typed with a poor typewriter ribbon or if the university sent us an inferior photocopy.

AVIS

La qualité de cette microforme dépend grandement de la qualité de la thèse soumise au microfilmage. Nous avons tout fait pour assurer une qualité supérieure de reproduction.

S'il manque des pages, veuillez communiquer avec l'université qui a conféré le grade.

La qualité d'impression de certaines pages peut laisser à désirer, surtout si les pages originales ont été dactylographiées à l'aide d'un ruban usé ou si l'université nous a fait parvenir une photocopie de qualité inférieure.

Canada

MEASUREMENT AND MODELLING OF THE RADIATION BUDGET OF ALPINE TUNDRA, PLATEAU MOUNTAIN, ALBERTA, CANADA

by

Huo Zonghui
B.Sc., Nanjing Institute of Meteorology, 1983

THESIS SUBMITTED IN PARTIAL FULFILLMENT OF THE REQUIREMENTS FOR THE DEGREE OF MASTER OF SCIENCE

in the Department of Geography

Simon Fraser University
May 1991

ISBN 0-315-78218-8

APPROVAL PAGE

Name: Zonghui Huo

Degree: Master of Science

Title of Thesis: Measurement and Modelling of the Radiation Budget of Alpine Tundra, Plateau Mountain, Alberta, Canada

Examining Committee:

Chair: I. Hutchinson, Associate Professor

W.G. Bailey
Associate Professor
Senior Supervisor

S.T. Wong
Professor

R.D. Moore
Assistant Professor

R.J. Williams
External Examiner
Senior Science Advisor
B.C. Ministry of Environment

Date Approved: May 22, 1991

PARTIAL COPYRIGHT LICENSE

I hereby grant to Simon Fraser University the right to lend my thesis, project or extended essay (the title of which is shown below) to users of the Simon Fraser University Library, and to make partial or single copies only for such users or in response to a request from the library of any other university, or other educational institution, on its own behalf or for one of its users. I further agree that permission for multiple copying of this work for scholarly purposes may be granted by me or the Dean of Graduate Studies. It is understood that copying or publication of this work for financial gain shall not be allowed without my written permission.

Title of Thesis/Project/Extended Essay

Measurement and Modelling of the Radiation Budget of

Alpine Tundra, Plateau Mountain, Alberta, Canada

Author:

(signature)

Zonghui Huo

(name)

May 22, 1991

(date)

ABSTRACT

A knowledge of net radiation on mountain slopes has utility in a range of climatological, hydrological and biological applications. A field experiment was conducted on Plateau Mountain, Alberta, Canada in the summer of 1989, in which all components of the radiation budget were measured on both horizontal and sloping surfaces.

A broad range of atmospheric conditions provided an opportunity to examine atmospheric and surface controls on the radiation budget. Global solar radiation and net solar radiation exhibited large fluctuations throughout the study period. On the contrary, the variability of longwave radiation components was conservative. Surface albedo also showed a conservative variation during the period, except on one occasion when there was a snow shower. Therefore, the magnitude of the radiation budget was principally controlled by atmospheric transmissivity which was in turn influenced by the amount and duration of cloud cover. The large differences of global solar radiation between the horizontal surface and sloping surfaces were mainly the result of the differences in the receipt of the direct beam solar radiation, which is determined by solar radiation, slope orientation, slope self-shading and surrounding terrain shading. Longwave radiation components play a smaller role in the differences between the net radiation regimes.

A number of models were tested for their applicability. These include models for separating global solar radiation into direct beam and diffuse radiation, models for estimating atmospheric radiation, and models for transposing global solar radiation and atmospheric radiation data from horizontal surfaces to sloping surfaces. The results illustrate that the models for separating global solar radiation into direct beam and diffuse radiation require modification to alpine conditions prior to application. The transposition models can predict global solar radiation within 15% of the values measured on sloping surfaces. The longwave radiation models can predict the longwave radiation within 11% of the measured values on horizontal surfaces and within 15% of the measured values on

sloping surfaces. Using these approaches, a flux-by-flux net radiation procedure can predict net radiation on sloping surfaces to an accuracy of about 20% of the measured values and the empirical model to 16% of the measured values.

ACKNOWLEDGEMENTS

I would like to thank my supervisor, Dr. W. G. Bailey, Department of Geography, Simon Fraser University, for his guidance and assistance throughout the field experiment and the writing of thesis. I would also like to acknowledge the valuable advice and comments given by Mr. R. J. Williams, British Columbia Ministry of Environment, Dr. R. D. Moore and Dr. S. T. Wong, both of Department of Geography, Simon Fraser University.

This research was funded by the Natural Sciences and Engineering Research Council of Canada (Operating Grant A2614 held by WGB). I wish to acknowledge the Ministry of Energy and Natural Resources of the Province of Alberta for permitting access to Plateau Mountain for research purposes. Thanks are also due to Dr. T. R. Oke (Department of Geography, University of British Columbia) and Mr. P. F. Mills (Agriculture Canada Research Station, Beverlodge, Alberta) for the use of field instruments.

I wish to thank Mr. E. J. Weick and Dr. I. R. Saunders for assistance in the preparation and the conducting of the field experiment. Also, thanks to Mr. Guo Yingping for the preparation of the field instrumentation.

Finally, I am particularly grateful to my wife, Liu Changlin, for her consistent assistance and encouragement which went into the making of this thesis.

TABLE OF CONTENTS

LIST OF FIGURES

LIST OF TABLES

Chapter 1

INTRODUCTION

1.1 The Radiation Budget in Alpine Environments

In alpine environments, the radiation budget or net radiation is the major input to the surface energy budget and therefore an important contribution to the energy available for hydrological, geomorphological and biological processes (Price, 1981; Price, 1988; Blumen, 1990).

In the study of hydrology, net radiation can be used in a model to predict snowmelt, or used in conjunction with a digital terrain model to provide estimates of the spatial variations of snow melting. Further application of the radiation budget can assist in the development of runoff models which could be used in the prediction of flooding and reservoir operations. In the study of alpine microclimatology, solar radiation falling on different facets of terrain surfaces produces a variety of microclimates. These microclimates have far-reaching effects on the ecosystems in these regions.

The radiation budget of a surface involves four components: global solar radiation, reflected solar radiation, incoming and outgoing longwave radiation. The relative importance of the four components is different for different surface conditions although the incoming solar radiation usually is the most important input. Determination of net radiation requires accurate measurements or estimates of the four components, especially global solar radiation. The radiation budget of a surface varies greatly, both spatially and temporally, depending upon climatic, topographic and surface conditions, particularly in mountainous regions at mid- and high-latitudes. Slope inclination and orientation will enhance these variations between slope facets. The surrounding topography also affects the radiation budget of a given slope through horizon effects and radiation reflected and emitted from surrounding terrain. Therefore, both topographic and surface characteristics of a site must

be considered in order to obtain representative values for short and longer temporal interval estimates.

Alpine areas consist of horizontal surfaces and sloping surfaces with different inclinations and orientations. In most applications, the radiation budget for a wide range of slope and slope orientations is required. However, measurements of the radiation budget are characteristically related to horizontal surfaces. There are at least two reasons for this discrepancy. The first is that standardization of exposure is more easily achieved if the sensors are horizontal. Only in this orientation can one reasonably assume that all sensors in a network have the same field of view. It is then possible to make comparisons between the values measured at separate locations. Secondly, it would be economically and practically impossible to provide measured data to represent adequately all angular radiation (Hay, 1986). The measurements on a horizontal surface, as a readily fixed and spatially representative orientation, provide the best basis for estimating radiation on sloping surfaces.

By recognizing the logistical difficulties in field measurements, a number of studies have been conducted toward the modelling of radiation budget components on sloping surfaces (Dozier and Outcalt, 1979; Hay and McKay, 1985). Among these studies, most are directed to engineering applications (Rowe and Willmott, 1984) and only a few are for climatological and hydrological purposes. Solar radiation has drawn great attention in the modelling of radiation budget because of its dominant role during the day and its utility in engineering applications. The longwave components of the radiation budget, however, have received relatively little attention (Barry, 1981; Price, 1981; Muller, 1985; Saunders, 1990). Although longwave radiation components are often of secondary importance in the radiation budget, their relative contribution to net radiation increases when a snow cover exists and when topographic influences are important (Olyphant, 1986a; Whiteman et al., 1989; Saunders, 1990).

Although a number of models of radiation budget components on sloping surface have been developed, very few studies have brought these components together and provided a complete modelling of the radiation budget. Further, to the author's knowledge, very few field measurements of sloping surface radiation budget have been undertaken in North American alpine areas. This leaves most of these models untested for alpine environments.

1.2 Objectives of the Current Research

It is clear from the foregoing comments that the alpine radiation budget is very important and that it has a variety of applications. A number of models for radiation budget components have been developed (Hay and McKay, 1985; Hay, 1986; Idso, 1981) but most of them still remain untested with broad alpine radiation data since few measurement projects of radiation budget have been conducted in alpine environments, especially on sloping surfaces. Therefore, the objectives of the current study are: 1) to describe the measurements of radiation budget on both horizontal and sloping surfaces of an alpine tundra, 2) to examine the performance and utility of physically based and empirical models of radiation budget components, and 3) to suggest and test approaches for estimating net radiation on alpine slopes of any inclination and orientation. The procedure taken is, at first, to include descriptive approaches to offer overviews of the atmospheric and surface controls of radiation transfer. This is then complemented by modelling of the radiation budget components. The modelling includes testing the performance of available models and deriving relations from the present data set.

1.3 Thesis Organization

This thesis is organized into nine interdependent chapters. Following a general introduction in Chapter 1, a literature review is presented in Chapter 2, which reviews past work on the measurement of radiation budgets in alpine areas and the modelling of radiation budget components on horizontal and sloping surfaces. Chapter 3 describes the

results of radiation budget measurements on horizontal surfaces and Chapter 4 summarizes the differences in radiation budget components between a horizontal surface and sloping surfaces.

All the modelling chapters (Chapter 5 through 8) follow a similar format which includes theoretical background, model description and model validation. Chapter 5 is concerned with the models for estimating direct beam and diffuse solar radiation from measured global solar radiation. Chapter 6 describes models for estimating solar radiation on sloping surfaces. The longwave radiation modelling is described in Chapter 7 and net radiation modelling in Chapter 8. Finally, Chapter 9 summarizes the main findings of this study, points out the existing problems and examines directions for possible future work.

1.4 The Field Sites

The experiment was conducted on Plateau Mountain, which is located in the Livingstone Range of the Rocky Mountains in southwestern Alberta, Canada (50°15' N and 114°31' W, see inset in Figure 1.1), at an elevation of 2475 m a.s.l. Figure 1.1 shows a topographic map of Plateau Mountain. The summit topography of Plateau Mountain is characterized by an extensive area of flat to gently rolling terrain well above the local tree line. This area runs south to north about 7 km with width being from 0.5 to 1.0 km. Surrounding this flat summit area are sloping surfaces oriented south, north, east and west with inclinations of 10° - 40°.

The locations of the five instrumentation sites are shown in Figure 1.1. Figures 1.2a - 1.2e show photographs of the horizontal site on the summit area and the four sloping sites situated on south, north, east and west slopes. The characteristics of each site are summarized in Table 1.1. The site altitudes in Table 1.1 were measured with an altimeter. Slope inclination and orientation were measured by a transit and an inclinometer. Vegetation, rock and bare ground coverages were determined by visual estimation. The sky view factor represents the openness of the site and is defined as the ratio of sky and

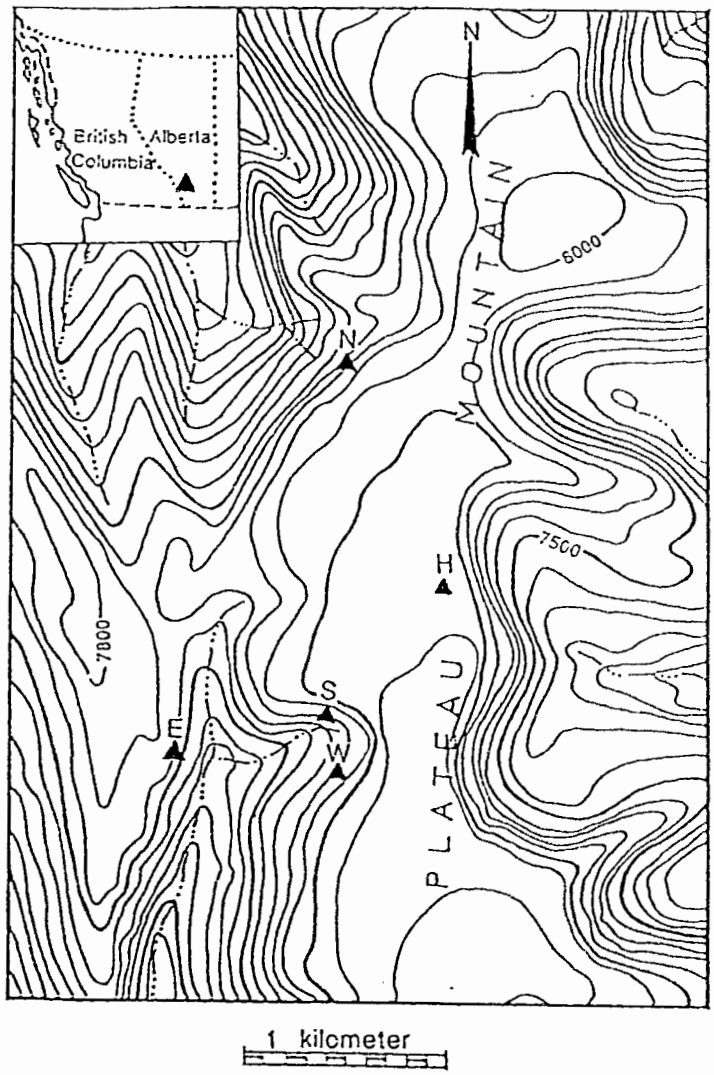

Figure 1.1 Map showing Western Canada (inset map) and the topography of the Plateau Mountain (contour interval in 100 feet). H: horizontal site, S: south sloping site, N: north sloping site, E: east sloping site and W: west sloping site.

Table 1.1 Summary of the Site Characteristics

Site	Date of Operation	Altitude (m asl)	*Azimuth (degree)	Slope (degree)	Sky View Factor	Vegetation (%)	Rock & Bare Ground (%)
Horizontal	6/20-7/24	2475	–	–	1.00	60	40
North slope	6/20-6/29	2326	164	31	0.87	95	5
South slope	7/9-7/15	2393	41	22	0.87	50	50
East slope	7/16-7/22	2297	292	30	0.83	95	5
West slope	6/30-7/8	2399	117	21	0.90	65	35

* Measured clockwise from true south.

viewing hemisphere, or the fraction of sky seen by horizontal or sloping surfaces. Therefore it was estimated by

$$f = 1 - 0.028 \sum_{i=1}^{36} \sin h_i . \qquad (1.1)$$

where h_i (i = 1, 2, ..., 36) is the elevation angle in the direction of i × 10°.

The horizontal site was located in the unobstructed summit area (Figure 1.2a). This area has a slight northwest aspect. The average slope of a 100 m transect running from southeast to northwest through the middle of the site is approximately 3%. In the area of instrumentation, 40% of the surface was dominated by frost mounds that were 2 - 4 m in diameter. The top of the mounds were generally covered with bare gravels and lichens. The vegetation was dominated by mat forming species and turf as described by Bowers (1988). Most vegetation was less than 100 mm in height.

The east sloping site was located on a east facing slope (30°) and had a relatively small sky view. This slope site was mostly covered by turf similar to that found at the horizontal site. Vegetation height was from 50 mm to 100 mm (Figure 1.2b).

The west sloping site was situated at a semi-vegetated west facing slope. On this site, the vegetation cover was lower (65%) and the vegetation height was less (0 - 50 mm). This slope has a relatively homogeneous surface type (Figure 1.2c).

At the south sloping site, the surface was half vegetated and half scree. The rock was mostly covered by lichens and therefore had a blackish colour. The vegetation species was similar to those found at the horizontal site and the height was 50 - 100 mm (Figure 1.2d).

The characteristics of the north sloping site were basically the same as those of the east sloping site except the orientation (Figure 1.2e).

Figure 1.2a Photograph showing the horizontal site and the instruments, looking to the east.

Figure 1.2b Photograph showing the east sloping site and the instruments, looking to the north.

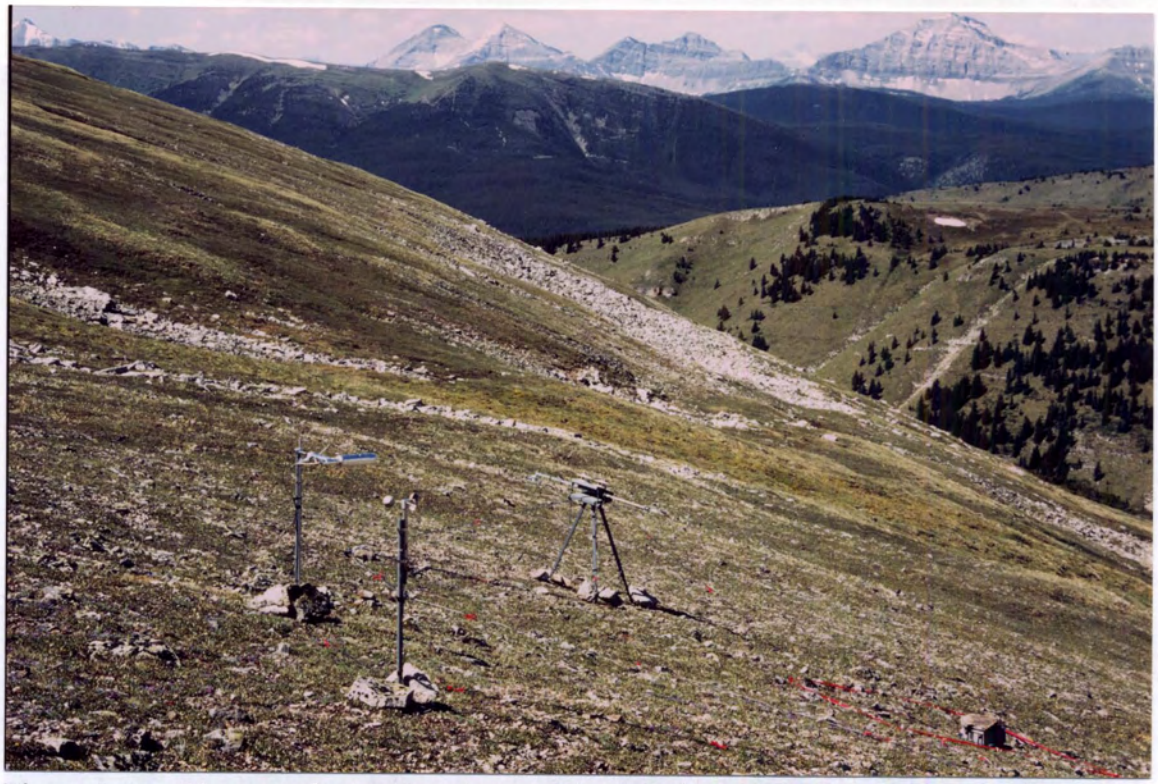

Figure 1.2c Photograph showing the west sloping site and the instruments, looking to the south.

Figure 1.2d Photograph showing the south sloping site and the instruments, looking to northwest.

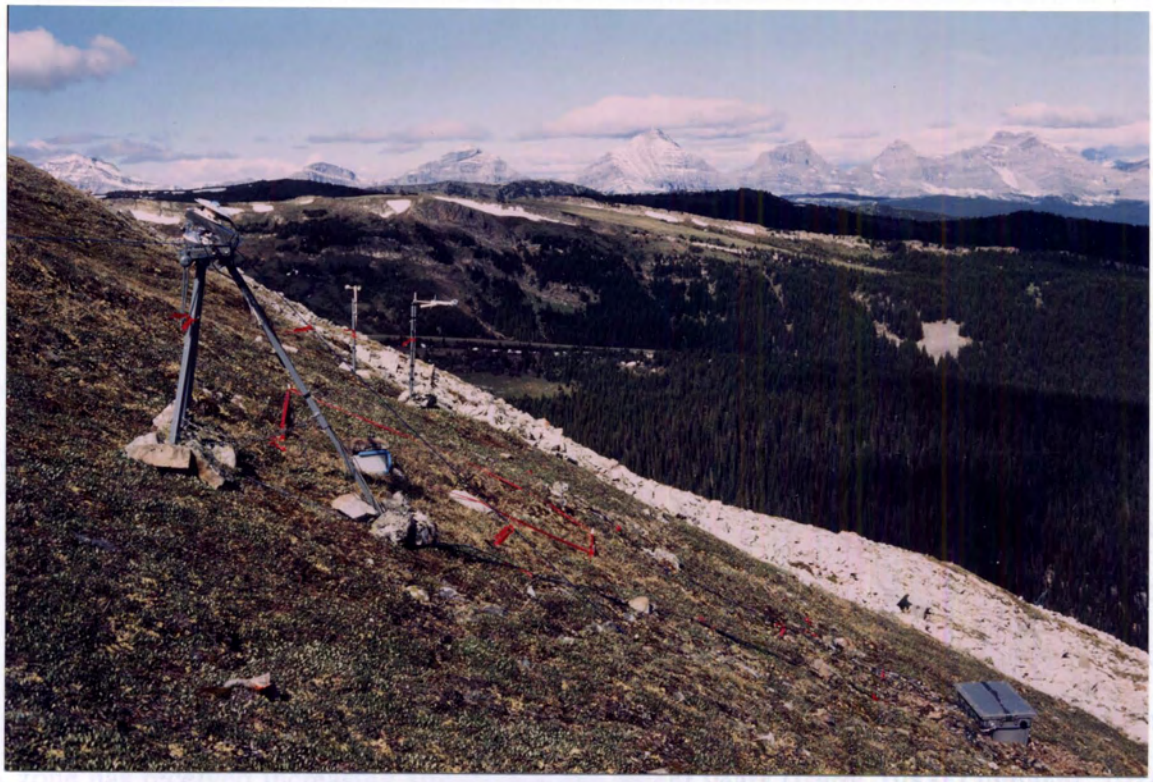

Figure 1.2e Photograph showing the north sloping site and the instruments, looking to the west.

Chapter 2

REVIEW OF RADIATION BUDGET STUDIES IN ALPINE ENVIRONMENTS

2.1 Introduction

Solar radiation is the ultimate driving force behind radiation transfers on the earth's surface. In alpine environments, the radiation budget is the major input to the surface energy budget and hence an important contribution to the energy available for various hydrological and biological processes. Therefore, radiation budget research in the alpine zone has received increasing attention in the recent years (Isard, 1983; Olyphant, 1984, 1986a, 1986b; Bowers, 1988; Bailey et al., 1989; Whiteman et al., 1989; Saunders, 1990). However, compared with other environments, the alpine radiation budget has received little attention. Especially scant is the attention given to the radiation budget on alpine sloping surfaces. This chapter reviews the radiation budget measurement and modelling studies in alpine regions on both horizontal and sloping surfaces, with the emphasis on the modelling of radiation budget components for sloping surfaces.

2.2 Theoretical Background

Alpine areas are an assemblage of horizontal and sloping surfaces of different inclinations and orientations. As for the term "alpine', Love (1970) suggested that it be reserved for treeless terrain above the krummholz zone. Therefore, the radiation budget study should be conducted on both horizontal and sloping surfaces. The radiation budget of an area is a function of the surface's inclination and orientation as well as its surrounding terrain characteristics. In this section, the radiation budget on a horizontal surface will be considered, after which sloping surfaces will be examined.

(1) Radiation Budget of a Horizontal Surface

The net radiation of an unobstructed horizontal surface, Q^*, results from the balances of solar radiation components and longwave radiation components:

$$Q^* = (K\downarrow - K\uparrow) + (L\downarrow - L\uparrow)$$
$$= K\downarrow (1 - A) + (L\downarrow - L\uparrow) \qquad (2.1)$$

where $K\downarrow$ is the global solar radiation, $K\uparrow$ reflected solar radiation (which is determined by surface albedo A), and $L\downarrow$ and $L\uparrow$ are respectively the incoming and outgoing longwave radiation.

Global solar radiation $K\downarrow$ is composed of two components, the direct beam solar radiation S_h and the diffuse solar radiation D_h

$$K\downarrow = S_h + D_h . \qquad (2.2)$$

Incoming longwave radiation can be estimated by the Stefan-Boltzmann law based on atmospheric temperature and effective emissivity. Outgoing longwave radiation can be determined with the knowledge of surface temperature T_s and surface emissivity

$$L\uparrow = \varepsilon \sigma T_s^4 + (1 - \varepsilon) L\downarrow \qquad (2.3)$$

where σ is the Stefan-Boltzmann constant (5.67×10^{-8} W m^{-2} K^{-4}) and ε is the surface emissivity. ε ranges from 0.90 to 0.99 for alpine tundra with an average of 0.95 for snow-free tundra surfaces (Saunders, 1990). Therefore $(1 - \varepsilon)$ becomes a negligible term.

(2) Radiation Budget of a Sloping Surface

Like the radiation budget of a horizontal surface, the radiation budget on a sloping surface Q_s^* is the balance of solar radiation components and longwave radiation components

$$Q_s^* = (K_s\downarrow - K_s\uparrow) + (L_s\downarrow - L_s\uparrow)$$
$$= K_s\downarrow (1 - A) + (L_s\downarrow - L_s\uparrow). \qquad (2.4)$$

The definitions of the terms in equation 2.4 are the same as the corresponding ones of a horizontal surface except that the subscript s refers to the sloping surface.

Solar radiation of a slope $K_s\downarrow$ is composed of three components

$$K_s\downarrow = S_s + D_s + K_t \tag{2.5}$$

where S_s is the direct beam solar radiation to the slope, D_s the diffuse solar radiation to the slope and K_t the solar radiation due to the reflection from surrounding terrain.

Incoming longwave radiation on a slope $L_s\downarrow$ includes two components

$$L_s\downarrow = L_{as} + L_{ts} \tag{2.6}$$

where L_{as} is the longwave radiation from atmosphere and L_{ts} longwave radiation from the surrounding terrain. Both L_{as} and L_{ts} can be estimated by the Stefan-Boltzmann law. However, the estimation of L_{as} is much more complex since the atmospheric emissivity is difficult to model. Outgoing longwave radiation $L_s\uparrow$ is determined by surface temperature and surface emissivity

$$L_s\uparrow = \varepsilon \sigma T_s^4 + (1 - \varepsilon) L_s\downarrow . \tag{2.7}$$

2.3 Radiation Measurements in Alpine Environments

Although about 20% of the earth's land surface consists of mountainous terrain and a greater area is affected by mountains (Barry, 1981), the radiation budget research in alpine areas has received limited attention (Barry, 1981; Saunders, 1990). The extreme weather conditions and lack of proper equipment may account for this. Along with the rapid developments in climatological equipment and computerized data acquisition systems, research activities in alpine area have increased. This section will provide a brief summary of the measurement results.

As mentioned in Chapter 1, the ideal site for a representative measurement of radiation budget is the one with surface homogeneity and a minimum obstruction to the sky hemisphere unless the object is to determine terrain effects on the radiation budget. Some mountain radiation measurements have been made on sloping surfaces or on valley floors where heavy shading effects of the surrounding terrain exist (Marks and Dozier, 1979; Olyphant, 1986a; Whiteman et al., 1989).

Measurement of all the radiation budget components is generally straightforward when using radiometers. Discussions of instrumentation are presented by Latimer (1972), Walton (1982) and Oke (1987). The errors in direct measurement tend to be small (within 10%) but increase when residuals are involved (Saunders, 1990).

In the past, a number of radiation measurement programs have been conducted in alpine environments. Amongst them, the majority has been accomplished in the European Alps (Barry, 1981). This relatively long history of measurements on glaciers has been analyzed and reviewed by Muller (1985). From a North America perspective, while acknowledging the existence of the large body of European results, Saunders (1990) presented a comprehensive review of the radiation budget measurements in North America. By referring to the previous reviews, the salient aspects are summarized as follows:

(1) Solar Radiation

Since solar radiation plays a dominant role in the radiation budget of alpine environments, it is widely studied. All the past radiation budget measurements included solar radiation. The decrease of atmospheric pressure with altitude implies theoretically the increase of solar radiation with altitude. The increase in solar radiation with altitude has been proved by numerous alpine radiation measurements and described in detail by Barry (1981).

Diffuse solar radiation decreases with altitude in cloudless sky conditions, but increases with cloud amount. Direct beam solar radiation increases with altitude in cloudless conditions. It decreases greatly with increasing cloud amount.

Although very few measurements have been made for alpine sloping surfaces, the work of Whiteman et al. (1989) has clearly shown the strong effect of slope inclination and orientation on the radiation budget during a cloudless day. Surrounding terrain shading is another important factor influencing the radiation budget components, especially direct beam solar radiation and longwave radiation.

Reflected solar radiation depends on surface albedo. For snow-free tundra, moraine and fellfield surfaces, the albedoes are similar and characterized by 0.15 to 0.20. Subalpine grass meadows have a slightly higher albedo of 0.25 (Halbsguth et al., 1984). For snow and ice surfaces, the albedoes possible on glacier surfaces range from 0.85 for fresh snow to 0.15 for very dirty ice (Muller, 1985). The diurnal trend of albedo has been discussed by a number of authors (Choudhury and Chang, 1981; Bailey et al., 1989; Whiteman et al., 1989).

(2) Longwave Radiation

Compared with solar radiation, there are fewer longwave radiation measurements, and most of those reported are from European Alps (Barry, 1981; Muller, 1985). Data reviewed by Barry (1981) and Muller (1985) confirmed that the decrease in temperature and atmospheric mass with higher altitudes leads to smaller incoming atmospheric radiation. As a consequence of the lower surface temperature, outgoing longwave radiation tends to be lower too. Therefore, net longwave radiation changes little with altitude.

Diurnal changes in incoming longwave radiation is well defined on cloudless days, with an early morning minimum and an afternoon maximum (Olyphant, 1986a; Bailey et al., 1989; Saunders, 1990). Increases in cloud amount results in increases in longwave radiation, and some authors developed relations between $L\downarrow$ and cloud amount (Bolz, 1949; Unsworth and Monteith, 1975).

Some mountain radiation studies have focused on the modification of the longwave irradiance induced by surrounding terrain (Marcus et al., 1981; Olyphant, 1986a; Whiteman et al., 1989). Their results clearly show the enhancement of $L_s\downarrow$ by surrounding terrain under cloudless sky conditions since their experimental sites have a smaller sky view factor.

(3) Net Radiation

Few studies pertaining only to net radiation have been done in mountain environments. However, the general conclusions from them show the decrease of net radiation with altitude and with cloud amount (Muller, 1985).

The conservative characteristics of albedo and net longwave radiation of snow-free alpine surfaces suggest the well defined relationship $Q^* = f(K\downarrow)$ (Terjung et al., 1969; Storr, 1972; Bailey et al., 1989). However, this relation becomes poor during the winter period of snow cover (Saunders, 1990).

Most of the results discussed above are derived from the data on horizontal surfaces. Even though sloping surfaces abound in mountainous areas, relatively few studies have been directed towards the radiation budget of sloping surfaces. In North America, the major field research pertaining to the radiation budgets of sloping surfaces has been concentrated in Colorado. The topographic influences on the radiation budget components are clearly shown on cloudless days (Whiteman et al., 1989). The possible influence on radiation budgets under cloudy sky conditions has yet been studied. An initial study by Isard (1989) suggests that the solar radiation differences induced by topography are offset by the diffusing effects of clouds and enhancement of longwave radiation. These suggestions still need further confirmation.

2.4 Methods for Estimating the Radiation Budget of Sloping Surfaces

The radiation budget of a surface consists of global solar radiation, reflected solar radiation, and incoming and outgoing longwave radiation. Global solar radiation, composed of direct and diffuse components, is the largest component and is the driving force in one way or another for the other components. It exhibits the greatest variation with topographic relief (Garnier and Ohmura, 1968; Whiteman et al., 1989). The longwave radiation components, however, are relatively conservative.

In the calculation of solar irradiance for sloping surfaces, it is common to commence with either measured or calculated values of the direct and diffuse irradiances for a horizontal surface. While there is a general availability of radiation data for horizontal surfaces (either directly measured or estimated using models), there is also a largely unsatisfied need for data from sloping surfaces. Since there are few direct measurements of sloping surface irradiance, numerical procedures have been used to arrive at estimates derived from horizontal surface values.

Over the past 30 years, a lot of work has been done on modelling the radiation budget components on horizontal and sloping surfaces, but few studies were directed towards the alpine environments, especially mountain slopes. Nevertheless, these methods could be used in alpine environments if they are properly tested. In this section, these models for different radiation budget components will be reviewed.

(1) Direct Beam Solar Radiation

Direct beam solar radiation has drawn the greatest attention in past studies since it has a vector character and plays a dominant role in the radiation budget. The estimation of direct beam solar radiation on sloping surfaces can be approached by solving a set of precise equations based on the geometrical relationship between the sun and the sloping surfaces. Quite a number of studies have been devoted to the calculation of direct solar radiation to different sloping surfaces (Kondratyev, 1969, 1977; Hay and Davies, 1980). All the methods are essentially one fundamental approach. Derivation of the appropriate relationships are provided by Kondratyev (1977) and will be presented in Chapter 6. The direct beam radiation for an arbitrarily oriented sloping surface S_s can be expressed by the direct solar radiation flux to an unobstructed horizontal surface S_h by using

$$S_s = S_h \cos i / \sin h_o \qquad (2.8)$$

where i is the incident angle of solar rays on a given surface and h_o is solar elevation angle. Both i and h_o can be calculated by a set of astronomical formulas. Therefore, using

equation 2.8 and with the given S_h, the direct solar radiation on sloping surface S_s can be estimated. Several computer programs have been written which give the direct solar radiation on horizontal surfaces, vertical walls and sloping surfaces (Buffo et al., 1972). Since the equations rely completely on the geometrical relationship between the sun and the sloping surface and no assumptions or simplifications are involved, they are considered universally valid. However, since the denominator in equation 2.8 will tend to zero near the sunrise and sunset, excessively high estimates of the slope's direct radiation can result. In Hay's (1977) consideration, this problem is avoided by commencing calculations at the full hour following sunrise and ending them at the full hour preceding sunset.

In calculating the direct solar radiation on sloping surfaces of alpine area, it is also worthwhile to note the screening effect of the surrounding terrain (Williams et al., 1972; Isard, 1983), Considering this, a binary coefficient can be included in equation 2.8. The binary coefficient is set equal to zero whenever the receiving surface is shadowed by the surrounding terrain.

(2) Diffuse Solar Radiation

On a cloudless day at sea level, typically about 15 - 20 % of the daily total incoming solar radiation is the diffuse component (Miller, 1981). In high altitudes, the diffuse fraction becomes small (Olyphant, 1984; Whiteman et al., 1989). However, the diffuse component becomes more dominant with increasing cloud cover. In the calculation of diffuse radiation on sloping surfaces, the methods are far less precise than that for direct beam radiation, and of necessity involves assumptions on the distribution of diffuse radiance over the sky hemisphere. If the distribution function of diffuse radiation in the sky hemisphere is known, the diffuse solar radiation on any surface can be easily obtained by integrating this distribution function over the sky domain viewed by the surface. The angular distribution functions have been studied by Hooper and Brunger (1980), and recently by Coombes and Harrison (1988). Unfortunately, those models are limited to

overcast conditions. Further studies are needed before they can be used for the present purpose.

Based on the assumptions of diffuse radiance distribution over the sky hemisphere, two kinds of models have been developed: isotropic models and anisotropic models. Here one isotropic model (Kondratyev, 1977) and several anisotropic models will be considered.

Isotropic model

The simplest distribution is that of a uniform irradiance over the sky hemisphere, the assumption of isotropy, and yielding the isotropic model. Kondratyev (1969, 1977) and numerous others have provided the mathematical derivation of the isotropic model for calculating the diffuse radiation of a sloping surface.

In deriving the model, it is assumed that the diffuse radiation in the sky hemisphere is isotropic, and the surface of the slope and the surface in front of it are absolutely black. Then, it is possible to neglect the radiation reflected from the horizontal surface to the slope and the effects of multiple reflection. The diffuse radiation to an unobstructed sloping surface can then be derived as

$$D_s = 0.5\,\pi\, I\,(1 + \cos\alpha) \qquad (2.9a)$$

$$= 0.5\, D_h\,(1 + \cos\alpha) \qquad (2.9b)$$

where I is the intensity of diffuse radiation and $D_h = \pi I$ is the diffuse radiation on a horizontal surface. Equation 2.9 is the isotropic model for diffuse solar radiation on an unobstructed sloping surface. When there exists horizon obstruction, D_s will be reduced. The reduction can be handled successfully by multiplying a surrounding terrain shading index. The derivation of the terrain shading index is presented in Appendix II.

Despite the popularity of the isotropic model (primarily due to its simplicity), there is ample direct and indirect evidence of its inappropriateness. As expected, this model underestimates the real diffuse radiation for south-facing slopes due to the inappropriate

isotropic assumption (Hay, 1977). Considering this fact, Buglar (1977), Klucher (1979), Hay and Davies (1980) and others have proposed their anisotropic models.

Anisotropic Models

Buglar (1977) argued that the anisotropy could be accommodated through an increase in the direct radiation by 5 percent, effectively yielding the sky diffuse radiation on a sloping surface

$$D_s = 0.5\, D_h\, (\, 1 + \cos\alpha\,) + 0.05\, S_s. \qquad (2.10)$$

In this form, the model ignores the fact that a portion of the isotropic radiation is also treated as directional. Hence a more consistent formulation should be (Hay and McKay, 1985)

$$D_s = 0.5\, (\, D_h - 0.05\, S_h\,)\, (\, 1 + \cos\alpha\,) + 0.05\, S_s\,. \qquad (2.11)$$

Although these two models incorporate the anisotropy by adding 5% of the direct radiation, the physical basis is not clear. Further, they are limited to cloudless skies. Therefore, more appropriate models have been developed.

(a) Klucher's anisotropic model

Klucher's anisotropic model (Klucher, 1979) is based on the model proposed by Temps and Coulson (1977). He extended Temps-Coulson cloudless sky model to all-sky conditions. In the Temps-Coulson model, two correction factors are combined with the isotropic model to account for each of the two regions of anisotropy in the diffuse radiation field. They determined that a factor, $1+\sin^3(\alpha/2)$, accounts for the increase in sky light near the horizon during cloudless days. Similarly, the sky brightening observed near the sun could be approximated by the factor $1+\cos^2 i\, \sin^3 Z$, where i and Z are the incident angle of the sun's ray to sloping surface and solar zenith angle respectively. Then the Temps-Coulson anisotropic clear sky model has the form of

$$D_s = 0.5\, D_h\, (\, 1 + \cos\alpha\,)\, (\, 1 + \sin^3(\,\alpha/2\,)\,)\, (\, 1 + \cos^2 i\, \sin^3 Z\,). \qquad (2.12)$$

Klucher's model introduced an anisotropic function

$$F = 1 - (D_h / K\downarrow) \qquad (2.13)$$

into Temps-Coulson anisotropic cloudless sky model to account for all-sky conditions (i.e. cloudless, partly cloudy and overcast). Then Klucher's all-sky anisotropic model takes the form

$$D_s = 0.5\, D_h\, (1 + \cos \alpha)\, [\, 1 + F \sin^3 (\alpha / 2)\,]\, [\, 1 + F \cos^2 i \sin^3 Z\,]. \qquad (2.14)$$

Equation 2.14 shows that under cloudless conditions, the ratio of diffuse to total solar radiation is very small, i.e. $F \approx 1$. Then equation 2.14 approximates the Temps-Coulson cloudless sky model (equation 2.12).

(b) Hay's anisotropic model

Hay (1979) and Hay and Davies (1980) have presented another anisotropic slope diffuse radiation model which is similar to Klucher's anisotropic model. The derivation was based on the following premises: *a*) when no direct beam solar radiation is observed in an hour (direct transmission is zero), the sky is essentially overcast and the isotropic model is approximate for the hour; *b*) in the absence of an atmosphere, all the radiation is direct beam (i.e. the direct transmission is 1.0) and in this limiting case all the radiation can be treated according to equation 2.8; *c*) for the case when the direct transmission is between these two extremes, the assumption is made that hourly integrated direct radiation will define the portion of diffuse radiation to be treated as isotropic and the portion to be treated as circumsolar. Therefore, the direct transmission is used to define an anisotropic index k as

$$k = S_h / K_0 \qquad (2.15)$$

where K_0 is extraterrestrial radiation on horizontal surface.

With equation 2.15, the diffuse radiation treated as isotropic (D_s') is

$$D_s' = 0.5\, D_h\, (1 + \cos \alpha)\, (1 - k) \qquad (2.16)$$

and the portion treated as circumsolar (D_s'') is evaluated as

$$D_s'' = D_h\, (k \cos i / \cos Z). \qquad (2.17)$$

The form of equation 2.17 is similar to that of equation 2.8 except that equation 2.17 is for circumsolar radiation. Then the diffuse radiation intercepted by the sloping surface is the sum of isotropic portion (2.16) and circumsolar portion (2.17)

$$D_s = D_h [0.5 (1 + \cos a) (1 - k) + k \cos i / \cos Z] . \qquad (2.18)$$

Equation 2.18 is Hay's all-sky condition anisotropic model. It will be noted that when the sky is overcast and no direct solar radiation observed, Hay's anisotropic model will treat all the diffuse radiation as isotropic. This is similar to Klucher's model.

Both Klucher's and Hay's anisotropic model are basically the same. The only difference between these models is the assumed distributions for clear sky radiance and the nature of the anisotropic factors ($F=D_h/K\downarrow$ for Klucher and $k=S_h/K_0$ for Hay). In another paper, Hay and McKay (1985) compared these two models using the data from Vancouver, British Columbia. They concluded that Hay's model performs better than Klucher's on all sloping surfaces, while Klucher's model works well only for south-facing slopes.

(c) Perez's anisotropic model (Perez et al., 1987)

This model describes the diffuse radiation from the sky as the superposition of an isotropic distribution, a circumsolar zone and a luminous horizon band. This is actually an attempt to replicate circumsolar and horizon brightening. The anisotropy may vary depending on meteorological conditions and is related to the following parameters which are used as model inputs, the amount of diffuse radiation on a horizontal plane and the ratio

$$\rho = (S_m + D_h) / D_h. \qquad (2.19)$$

The basic Perez model is expressed as

$$D_s\downarrow = D_h \{ 0.5 (1 + \cos \alpha) (1- F_1)+ F_1 (a/c) + F_2 \sin \alpha\} \qquad (2.20)$$

where a is the solid angle corresponding to the circumsolar zone as seen from the slope and c denotes the solid angle corresponding to the circumsolar zone as seen from the horizontal surface. F_1 and F_2 are luminosity coefficients for the circumsolar zone and horizon band, respectively. The determination of a, c, F_1 and F_2 is given by Perez et al. (1987).

(3) Reflected Irradiance for a Sloping Surface

As a result of its simplicity and the lack of observation data, the approach used to calculate the reflected irradiance for a sloping surface has generally been based on the assumption of isotropic reflection from an infinite horizontal surface in front of the slope. This allows the derivation of the isotropic models. Following Kondratyev (1977) and Davies and Hay (1980), this model can be derived theoretically

$$K_t = 0.5\, K\uparrow\, (\, 1 - \cos\alpha\,) \,. \qquad (2.21)$$

If the surrounding surface is not horizontal but has a slope angle α', then the term $\cos\alpha$ in equation 2.21 should be written as $\cos(\alpha + \alpha')$, and $K\uparrow$ be replaced by $K_s\uparrow$ (Hay, 1971)

$$K_t = 0.5\, K_s\uparrow\, [\, 1 - \cos(\alpha + \alpha')\,] \,. \qquad (2.22)$$

Equations 2.21 and 2.22 are the basic isotropic models for reflected irradiance to a sloping surface. These models are suitable for most surfaces like grass and bare ground where directional reflectance is not obvious. Problems do arise from the fact that some surfaces (such as water and snow surfaces) exhibit strong directional reflection (Dirmhirn and Eaton, 1975; Eaton and Dirmhirn, 1979; Paltridge and Platt, 1976). The directional reflection is found to be a function of both solar zenith angle and the azimuth angle between the sun and the sloping surface (Temps and Coulson, 1977). Considering this, Temps and Coulson (1977) proposed a correction factor to accommodate the anisotropy of the surface reflectance under cloudless sky such that

$$K_t = 0.5\, K\uparrow\, [\, 1 - \cos\alpha\,]\, [\, 0.5\, (\, 1 - \cos Z\,)]\, [\, \cos(\, \psi_o - \psi_\alpha\,) - b'\,] \qquad (2.23)$$

where b' is a coefficient. As a consequence of the lack of data, the performance of this model has not yet been assessed.

In practical use, most authors have adopted an isotropic model (Hay, 1977; Olyphant, 1986b). Finally, it should be noted that for most surfaces K_t is very small compared to the direct and diffuse solar radiation.

(4) Longwave Radiation

In the radiation budget equation, the longwave radiation is composed of two components: outgoing longwave radiation and incoming longwave radiation.

Outgoing Longwave Radiation

If reliable measurements of surface temperature and surface emissivity are available, outgoing longwave radiation can be estimated by the Stefan-Boltzmann law (equation 2.3). Representative measurements of surface temperature are usually difficult to obtain. Therefore, Saunders (1990) proposed another approach which uses air temperature and incoming solar radiation as inputs. Based on his data, he obtained

$$L\uparrow = \sigma T_a^4 + 0.1\ K\downarrow \qquad (2.24)$$

for a snow-free alpine tundra. This approach has the advantage that the inputs are routinely observed. The apparent assumption of equation 2.24 is that, at night there is no significant difference between surface temperature and air temperature and during the daytime, the influence of surface radiative heating on $L\uparrow$ can be accounted for by adding 10% of $K\downarrow$ to σT_a^4.

Incoming Longwave Radiation from the Atmosphere

Incoming longwave radiation from the atmosphere is more problematic to model. A number of models have been developed. All these models need screen level values of temperature or vapour pressure or both as inputs. These models have been of two basic types (Table 2.1): those purely empirical, based on correlations with actual measurements of the longwave radiation (Brunt, 1932; Swinbank, 1963; Idso and Jackson, 1969; LeDrew, 1975), and those more analytical, derived on apparent physical grounds (Brutsaert, 1975; Marks and Dozier, 1979; Idso, 1981).

Brunt (1932) first proposed that the emittance under cloudless skies could be approximated from the water vapor content and temperature at screen level. He used

Table 2.1 Selected Incoming Longwave Radiation Models

Model	Equation Form	Equation
Brunt (1932)	$L\downarrow = \sigma T_a^4 \, (0.604 + 0.048 \sqrt{e})$	(2.25)
LeDrew (1975)	$L\downarrow = \sigma T_a^4 \, (0.491 + 0.067 \sqrt{e})$	(2.26)
Swinbank (1963)	$L\downarrow = \sigma T_a^4 \, (0.92 \times 10^{-5} T_a^2)$	(2.27)
Idso-Jackson (1969)	$L\downarrow = \sigma T_a^4 \, \{ 1 - 0.261 [-7.704 \times 10^{-4} (273 - T_a)^2] \}$	(2.28)
Berdahl-Martin (1984)	$L\downarrow = \sigma T_a^4 \, [0.711 + 0.56 (T_{dp}/100) + 0.73 (T_{dp}/100)^2]$	(2.29)
Brutsaert (1975)	$L\downarrow = \sigma T_a^4 \, [1.24 (e / T_a)^{1/7}]$	(2.30)
Idso (1981)	$L\downarrow = \sigma T_a^4 \, [0.179 \, e^{1/7} \exp(350/T_a)]$	(2.31)
Marks-Dozier (1981)	$L\downarrow = \sigma T_a^4 \, [1.24 (e' / T_a')^{1/7}] [P_0/1013]$	(2.32)

Symbols: T_a = air temperature (K), T_{dp} = dew point temperature (C), e = vapour pressure (10^{-1} kPa), $e'=RHe_s(T')$, $T'= T_a + (0.0065\ z)$, P_0 = station air pressure (10^{-1} kPa), RH = relative humidity at station (%), e_s = saturation vapour pressure (10^{-1} kPa), z = elevation of station (m).

regression analysis to develop his empirical model (equation 2.25). The coefficients given by Brunt in equation 2.25 are those applicable to the Northern Hemisphere. Following Brunt's suggestion, there were many attempts to develop a more universal relationship. But most individuals have utilized local empirical adjustment for estimating longwave radiation. LeDrew (1975) examined the performance of four longwave radiation models at a high altitude alpine site and presented his modified form of Brunt model (equation 2.26) by using the high altitude data. In his conclusion, he suggested the preference to use models based on observations of both vapour pressure and temperature in alpine environments.

The Swinbank (1963) model and Idso and Jackson (1969) model require only air temperature as input with the explicit assumption being that the surface vapour pressure is correlated with air temperature.

Brutsaert (1975) proposed another model to predict incoming longwave radiation at ground level under a cloudless sky. By integrating Schwarzschild's atmospheric transfer equation under the assumption of a standard atmosphere, he was able to show the good agreement of his results with those obtained by an empirical formula based on water vapor and temperature. However, his model has the advantage of being physically based, without the need for empirical parameters from radiation measurements. Following the Brutsaert model, Marks and Dozier (1979) and Idso (1981) proposed models which also require both air temperature and vapour pressure as inputs. In the Marks and Dozier model, an extrapolation of air temperature to a sea level equivalent value and pressure-correction of the calculations of emissivity are incorporated to account for the high altitude.

Of all these models mentioned above, only LeDrew's used alpine data while the Marks and Dozier model is proposed for alpine environments. The others used non-alpine data as the basis for verification. It should be noted that all the longwave radiation models in Table 2.1 are cloudless sky models. The cloudless sky assumption is obviously not true for

mountain environments. To accommodate the sky cloudiness, corrections to the cloudless sky model were proposed, such as those developed by Bolz (1949)

$$L_c\downarrow = L\downarrow (1+ a_1 n^2) \tag{2.33}$$

and Unsworth and Monteith (1975)

$$\varepsilon_c = \varepsilon_a + 0.84\, n\, (1 - \varepsilon_a) \tag{2.34}$$

where $L_c\downarrow$ is cloudy sky longwave radiation, $L\downarrow$ is cloudless sky longwave radiation, n is the fraction sky covered by clouds ($0 < n < 1.0$) and a_1 is a variable contingent on cloud type. Oke (1987) has listed its values for different clouds. Since only cloud amount was observed in the experiment, an average of a_1 for all cloud types (0.21) is used in this study. ε_c and ε_a are respectively the atmospheric emissivity for cloudy sky and cloudless sky. Given ε_c, the calculation of $L_c\downarrow$ is straightforward.

Longwave Radiation on Sloping Surfaces

A large portion of the mountain area is made up of sloping surfaces. Therefore, in the longwave radiation budget, the longwave radiation on sloping surfaces seems more important than on horizontal surface. Unfortunately, to the author's knowledge, few studies were directed to this aspect.

The incoming longwave radiation on sloping surface comes from two sources: the atmosphere and surrounding terrain. Very few studies addressed the longwave radiation from surrounding terrain since it is difficult to parameterize the surrounding terrain and very few field measurements were made (Olyphant, 1986a). The incoming longwave radiation from the atmosphere was addressed by Kondratyev (1977) and Unsworth (1975). Assuming that longwave radiation from the atmosphere is isotropic

$$L_{as} = 0.5\, L\downarrow (1 + \cos \alpha) \tag{2.35}$$

where $L\downarrow$ can be calculated by using the models in Table 2.1. However, the longwave radiation from the sky is also anisotropic (Robinson, 1947, 1950; Unsworth and Monteith,

1975; Kondratyev, 1977). Under the anisotropic assumption, Unsworth proposed a model to calculate L_{as}

$$L_{as} = \varepsilon_{as} \sigma T_a^4 \tag{2.36}$$

where

$$\varepsilon_{as} = \underbrace{\frac{1}{2}\varepsilon_a (1 + \cos\alpha) - \frac{1}{4} b (1 + \cos\alpha)}_{I_1} + \underbrace{\frac{2b}{\pi}\int_0^{\pi}\int_{h_1}^{\pi/2} f \ln(\text{cosec } h)\, dh\, d\psi}_{bI_2}.$$

$$= I_1 + bI_2 \tag{2.37}$$

The first term (I_1) on the right hand side of (2.37) corresponds to an isotropic distribution of atmospheric emittance, and the remaining term (bI_2) represents the anisotropic component which can be evaluated numerically without any inputs (b = 0.088).

Although this model is theoretically improved over the isotropic model, it has not been tested against measurement. We should also keep in mind that mountainous areas are characterized by cloudy sky conditions. This anisotropic characteristic may be masked by cloud effects. In this case, the simple isotropic model may be appropriate.

2.5 Conclusions

Despite the fact that there is an increased number of publications about the radiation budget of alpine environments, relatively little effort has been spent on field measurements in alpine areas. Furthermore, most of the measurement work has been conducted in the summer season. In fact, there still is a dearth of field measurements of the radiation budget, particularly for sloping surfaces.

A variety of slope irradiance models have been developed in the past two decades. This chapter discussed only the models commonly used. From this discussion it should be apparent that the accurate computation of radiation incident on sloping surfaces is possible as long as the criteria for each model are treated properly. The models for direct solar radiation are universal. The diffuse radiation models still need to be validated in alpine environments. Longwave radiation models are more limited to their study areas due to the

empirical coefficients included in them. The reflected irradiance on a slope has, more or less, a directional component for all kinds of surfaces. Therefore the isotropic model may not be appropriate. This is particularly the case for snow covered surfaces and water surfaces which have high directional reflection. The cloud factor, which is very important for longwave radiation, has not been taken into account in the longwave radiation models. This could be done by the analysis of simultaneousiy obtained incoming longwave radiation measurements and cloud observations. However, the major problem at hand is the lack of field measurements for validating and refining these models.

Chapter 3

THE SUMMER RADIATION BUDGET OF ALPINE TUNDRA, PLATEAU MOUNTAIN, ALBERTA, CANADA

3.1 Introduction

From the previous two chapters it is apparent that the need still exists for basic data collection and further research in order to quantitatively describe the radiation budget regimes of mountain environments. A research program was conducted on Plateau Mountain in the summer of 1989. This chapter presents the results of radiation budget measurements during the data collection period of 1989. Representative days (clear, partly cloudy, cloudy and a day following snow) are chosen for analyzing the diurnal behavior of radiation budget components in this alpine tundra. Finally, relationships between global solar radiation and net radiation and the relationship between global solar radiation and the photosynthetically active radiation (PAR) will be discussed in detail.

3.2 Theoretical Background

Net radiation Q^* on a surface is a result of the net exchanges in solar and longwave radiation

$$\begin{aligned} Q^* &= K^* + L^* \\ &= (K\downarrow - K\uparrow) + (L\downarrow - L\uparrow) \end{aligned} \tag{3.1}$$

where net solar radiation K^* is the difference between global solar radiation $K\downarrow$ and reflected solar radiation $K\uparrow$, net longwave radiation L^* is the difference between incoming longwave radiation $L\downarrow$ and outgoing longwave radiation $L\uparrow$.

Global solar radiation $K\downarrow$ is governed by the extraterrestrial radiation K_0 and atmospheric transmissivity t

$$K\downarrow = K_0\, t\,. \tag{3.2}$$

K_0 is related to the solar constant I_0 by

$$K_0 = I_0 \cos Z / R^2 \qquad (3.3)$$

where Z is the solar zenith angle and R is the length of the radius vector.

Global solar radiation can be separated into direct beam solar radiation S_h and diffuse solar radiation D_h

$$K\downarrow = S_h + D_h \qquad (3.4)$$

where the subscript h denotes the components are on a horizontal surface. The ratio of K↑ to K↓ is defined as albedo ($A = K\uparrow / K\downarrow$). Hence reflected solar radiation can be expressed as

$$K\uparrow = A\, K\downarrow . \qquad (3.5)$$

Incoming longwave radiation can be estimated by the Stefan-Boltzmann law. But this necessitates the estimation of atmospheric transmissivity. Outgoing longwave radiation can be calculated from the Stefan-Boltzmann law

$$L\uparrow = \varepsilon \sigma T_s^4 + (1 - \varepsilon) L\downarrow \qquad (3.6)$$

where ε is surface emissivity, σ the Stefan-Boltzmann constant (5.67×10^{-8} Wm^{-2} K^{-4}) and T_s is the surface temperature in Kelvin.

3.3 Observational Procedure

The experiment was conducted on Plateau Mountain, southwestern Alberta, Canada (about 50°15'N and 114°31'W). Chapter 1 gave a detailed description of the sites. The horizontal site was located on an unobstructed summit area and at an elevation of about 2475 m a.s.l. This area has a slight northwest aspect, with the average slope less than 3%. The measurement program started on June 20 and ended on July 24, 1989. On the horizontal site, solar radiation K↓ was measured by an Eppley Precision Spectral pyranometer (Eppley PSP). Another Eppley PSP with shadow band (constructed according to the dimensions of an Eppley diffusograph) was used to measure the diffuse solar radiation. Shadow band correction was made following the procedure of Latimer (1972). Data analysis shows that the diffusograph worked well. When it was overcast, all the

incoming solar radiation was diffuse. Figure 3.1 shows the agreement between the diffuse radiation measured with the diffusograph and K↓ sensor during the overcast period. The high quality diffuse radiation measurements enable the separation of K↓ into direct and diffuse solar radiation using equation 3.4. Reflected solar radiation K↑ measurements were made by a downward-looking Middleton CN-7 pyranometer. In the first week of the experiment, this sensor failed, and was replaced by another inverted Eppley PSP.

Incoming longwave radiation L↓ was measured by an Eppley pyrgeometer. Net radiation Q^* measurement was made with a Middleton CN-1 net pyrradiometer. The outgoing longwave radiation L↑ was calculated as a residual from equation 3.1. Surface temperature T_s was measured with two thermocouple arrays (each has ten thermocouples connected in parallel). Unfortunately, some thermocouples were partially exposed directly to the sun. They overestimated the T_s during partly cloudy and clear periods because of radiative heating. But during night and overcast period, they gave good temperature measurement. The calculated L↑ by equation 3.6 (emissivity 0.95) with T_s corresponded to that estimated from equation 3.1 by residual (Figure 3.2).

On the horizontal site, another Eppley PSP equipped with a RG-695 filter hemisphere was used to measure the non-photosynthetically active radiation (i.e. the wavelength larger than 0.7 μm). The photosynthetically active radiation (PAR) was evaluated as the difference between global solar radiation and this measurement.

All the radiation sensors (except the diffusograph) were mounted on a tripod 1.5 m above the ground. All measurements were collected and processed by a Campbell Scientific 21X datalogger. The 21X was programmed to sample once every 10 seconds and output half-hourly averages.

3.4 Daily Radiation Components during the Experiment Period

The measurement period during 1989 encountered variable weather that was representative of the summer climate of the mountain area. Data from the field will be

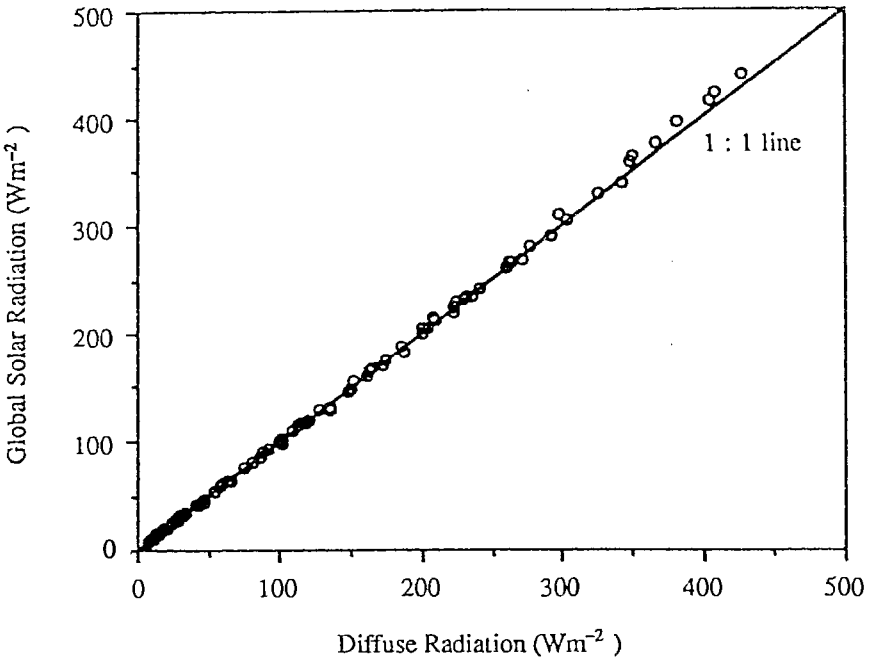

Figure 3.1 Half-hour average diffuse radiation measured with diffusograph against half-hour average global solar radiation during overcast period (a =0, b =1.0, r^2 = 1.0).

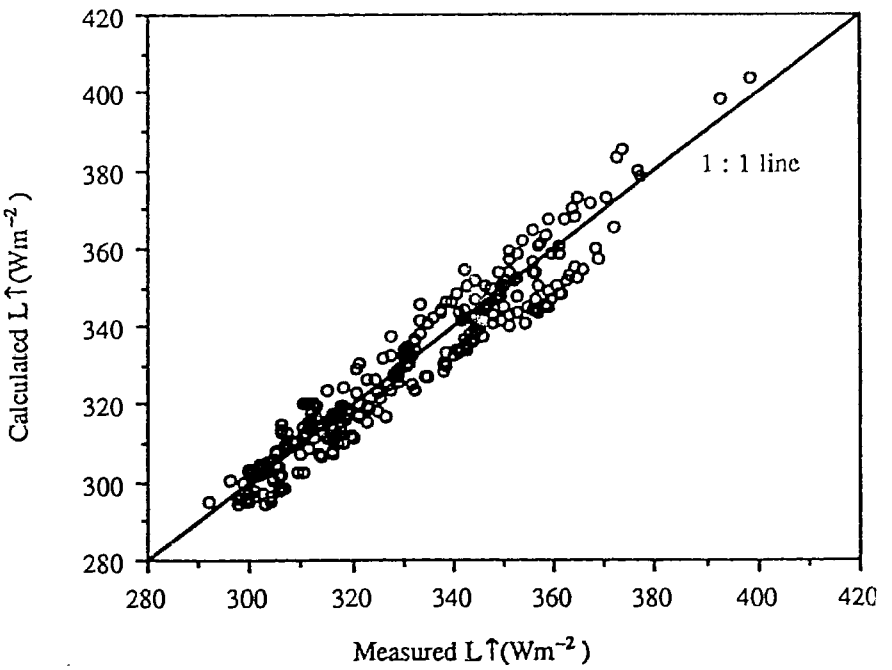

Figure 3.2 Measured outgoing longwave radiation versus calculated values from the Stefan-Boltzmann law (a =0, b =1.0, r^2 = 0.985).

presented in this section to illustrate the day-to-day variation of the radiation budget during the period.

Figure 3.3 and Figure 3.4 present the trends of daily radiation components, transmissivity and albedo during the period. Table 3.1 lists the daily values of radiation components. The means, maxima and minima of daily radiation components in the period of observation are summarized in Table 3.2. The standard deviations and coefficients of variation are also presented in Table 3.2. The coefficient of variation, defined as the ratio of the standard variation to the mean, is a measure of relative variation of the radiation components.

(1) Solar radiation budget components

The observation period began at the summer solstice. As the daylight period was getting shorter, the daily extraterrestrial radiation decreased steadily from 41.8 to 39.2 $MJm^{-2}d^{-1}$. As reflected in Figure 3.3, the period experienced variable weather conditions from overcast (daily transmissivity t = 0.19) to cloudless (t = 0.80). The coefficient of variation for the transmissivity was as high as 0.30. Daily transmissivity exceeded 0.75 on 4 days, lower than 0.45 on 8 days and approached 0.19 one day. These high daily t values have also been measured in other middle latitude alpine sites (Terjung et al., 1969; Isard, 1983; Olyphant, 1984; Bailey et al., 1989; Saunders, 1990). The very low daily t, however, was caused by the very heavy clouds accompanied with a slowly moving frontal system. The daily K↓ changed with transmissivity, consequently with the cloud amount. The coefficient of variation for K↓ was 0.293, close to that of t. When cloud coverage increased, direct solar radiation decreased. On the contrary, diffuse solar radiation increased with the increasing cloud coverage. The coefficient of variation for diffuse solar radiation was more extreme (0.655). The loss of direct solar radiation on a cloudy day is only partly compensated by an increase in diffuse solar radiation, resulting in a net decrease in K↓.

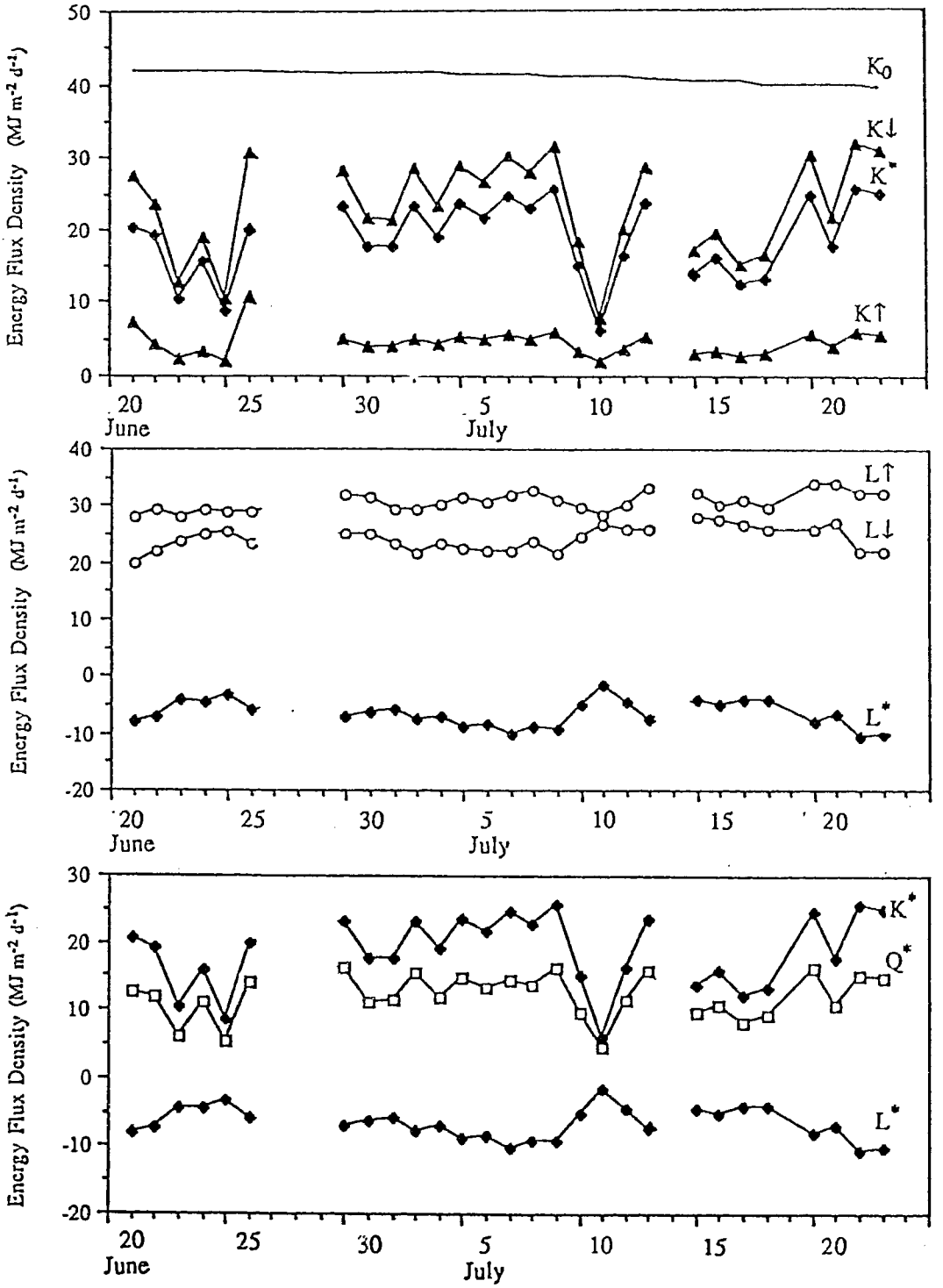

Figure 3.3 Daily radiation budget components, Plateau Mountain, June and July 1989.

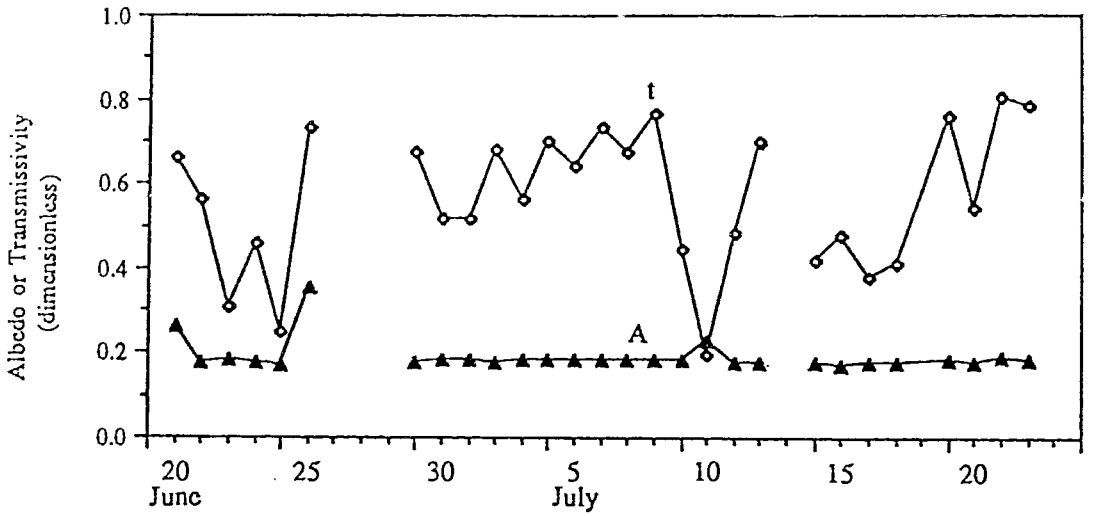

Figure 3.4 Daily average albedo and transmissivity, Plateau Mountain, June and July 1989.

Table 3.1 Daily Radiation Components, Albedo and Transmissivity for Plateau Mountain, June 20 - July 22, 1989

Day	K_0	K↓	D	t	K↑	A	K*	L↓	L↑	L*	Q*
June 20	41.8	27.6	–	0.66	7.2	0.26	20.4	19.9	27.8	-7.9	12.5
21	41.8	23.4	22.7	0.56	4.2	0.18	19.3	22.2	29.5	-7.3	11.9
22	41.8	12.9	9.3	0.31	2.4	0.19	10.5	23.8	28.1	-4.3	6.2
23	41.8	19.0	10.6	0.45	3.3	0.17	15.7	25.0	29.4	-4.5	11.2
24	41.8	10.5	9.1	0.25	1.8	0.17	8.7	25.3	28.7	-3.4	5.3
25	41.8	30.6	5.9	0.73	10.7	0.35	19.9	23.1	28.8	-5.7	14.2
26	-	-	-	-	-	-	-	-	-	-	-
27	-	-	-	-	-	-	-	-	-	-	-
28	-	-	-	-	-	-	-	-	-	-	-
29	41.6	28.0	7.1	0.67	4.9	0.17	23.1	24.8	31.8	-7.0	16.1
30	41.6	21.6	10.7	0.52	3.9	0.18	17.7	24.9	31.4	-6.4	11.3
July 1	41.5	21.3	12.2	0.51	3.9	0.18	17.5	23.1	29.1	-6.0	11.4
2	41.5	28.3	5.1	0.68	5.0	0.18	23.2	21.7	29.3	-7.6	15.6
3	41.4	23.3	9.1	0.56	4.2	0.18	19.1	23.1	30.2	-7.1	12.0
4	41.3	28.8	7.3	0.70	5.2	0.18	23.6	22.4	31.3	-8.9	14.7
5	41.2	26.5	5.8	0.64	4.9	0.18	21.7	22.1	30.6	-8.5	13.2
6	41.2	30.1	5.6	0.73	5.6	0.19	24.6	21.8	31.9	-10.1	14.5
7	41.1	27.8	5.8	0.68	5.0	0.18	22.8	23.6	32.7	-9.0	13.8
8	41.0	31.4	5.2	0.77	5.8	0.18	25.6	21.7	30.9	-9.3	16.3
9	40.9	18.3	13.8	0.45	3.4	0.19	15.0	24.7	29.9	-5.2	9.7
10	40.8	7.9	7.4	0.19	1.8	0.23	6.1	26.9	28.4	-1.5	4.6
11	40.7	19.8	11.6	0.49	3.5	0.18	16.3	25.8	30.3	-4.5	11.7
12	40.6	28.5	5.5	0.70	5.1	0.18	23.4	25.8	33.1	-7.4	16.0
13	-	-	-	-	-	-	-	-	-	-	-
14	40.3	16.9	9.4	0.42	3.0	0.18	13.8	27.9	32.2	-4.3	9.6
15	40.2	19.2	6.5	0.48	3.3	0.17	15.9	27.5	32.7	-5.2	10.7
16	40.1	15.1	8.9	0.38	2.7	0.18	12.4	26.9	30.9	-4.1	8.4
17	39.6	16.2	10.2	0.41	2.9	0.18	13.2	25.8	29.9	-4.0	9.2
18	-	-	-	-	-	-	-	-	-	-	-
19	39.6	30.0	4.1	0.76	5.4	0.18	24.5	26.0	34.2	-8.2	16.4
20	39.6	21.5	7.8	0.54	3.8	0.18	17.6	27.3	34.2	-6.9	10.8
21	39.4	31.6	2.3	0.80	5.9	0.19	25.6	21.9	32.3	-10.2	15.3
22	39.2	30.8	2.4	0.79	5.7	0.19	25.0	22.0	32.3	-10.3	14.7

Note: Units for all radiation components are MJ m^{-2} d^{-1}. Albedo (A) and transmissivity (t) are dimensionless. The data on June 26-28 are missing because of instrumentation difficulties, and are incomplete for July 13 and 18, 1989.

Table 3.2 Summary of the Daily Radiation Budget Components, Albedo and Transmissivity for Plateau Mountain during June 20 - July 22, 1989

Components	Maximum	Minimum	Mean	Standard Deviation	Coef. of Var.
K_0	41.8	39.2	40.9	–	–
$K\downarrow$	31.6	7.9	23.1	6.770	0.293
t	0.80	0.19	0.57	0.168	0.296
D	30.9	2.3	9.0	5.900	0.655
$K\uparrow$	10.7	1.8	4.4	1.810	0.407
A	0.35	0.17	0.19	0.036	0.189
K^*	25.6	6.1	18.6	5.370	0.288
$L\downarrow$	27.9	19.9	24.2	2.150	0.089
$L\uparrow$	38.4	27.8	31.0	2.270	0.073
L^*	-1.5	-10.0	-6.6	2.300	0.348
Q^*	16.4	4.6	12.0	3.310	0.275

Reflected solar radiation depends on the surface albedo. Daily albedo varied between 0.17 and 0.19 for 90% of the days, depending on the surface characteristics. The results of this experiment are slightly higher than the values presented by Bailey et al. (1989). The higher albedoes on June 20 and June 25 were caused by the partly snow covered surface.

The essentially constant albedo resulted in the transmissivity controlling the daily net solar radiation K^*. The coefficient of variation for K^* was 0.288, also close to that of t. This conclusion has also been described by a number of other research in arctic areas (Rouse, 1984) and in high altitude areas (Bailey et al., 1989; Whiteman et al., 1989).

(2) Longwave radiation budget components

Incoming longwave radiation is the largest daily energy supplier to earth's surface. It ranged between 19.9 and 27.9 $MJm^{-2}d^{-1}$ during the observation period (Table 3.2). Its coefficient of variation (0.089) was low relative to variations in the other radiation quantities. However, the subtle variation reflected the changing atmospheric moisture and cloud amount.

Outgoing longwave radiation is the largest of all daily averaged radiative fluxes (Figure 3.3), ranged from 27.8 to 38.4 $MJm^{-2}d^{-1}$. Like $L\downarrow$, its coefficient of variation was 0.073. The slight increasing trend of $L\uparrow$ over the experiment period reflected the seasonal increase in surface temperatures.

Since the outgoing longwave radiation is partly counter-balanced by incoming longwave radiation, the net longwave radiation L^* is much smaller than net solar radiation and the coefficient of variation (0.348) is much higher than that of $L\downarrow$ and $L\uparrow$. During heavy cloud days, L^* tended towards 0 $MJm^{-2}d^{-1}$.

(3) Net radiation

As the net longwave radiation is much smaller than net solar radiation, net solar radiation controls the net radiation Q^*. Consequently, the coefficient of variation in Q^*

(0.275) was close to that of K^* and K↓. The daily Q^* shows a strong relationship with K↓ (which will be discussed in Section 3.6).

3.5 Diurnal Variation in Radiation Budget Components

The 1989 observation period provided a good opportunity to examine the radiation components under different weather conditions. Among the 28 usable days only 4 days were clear and 3 fully overcast. About 70% of the days were partly cloudy. Therefore examination of the radiation regime of alpine environment should include not only those clear and overcast days, but more importantly the partly cloudy days. In this section, four particular days are chosen for a complete examination of the diurnal variation in radiation budget components. July 21 was characterized by its clear sky condition (Figure 3.5a) and July 10 by its overcast sky condition (Figure 3.5b). July 7 (Figure 3.5c) represents a typical summertime sky feature in most mid-latitude continental mountains, beginning with a clear sky in the morning, followed by a convective cloud buildup during the midday and afternoon. June 25 (Figure 3.5d) was an example of snow shower in early morning. The thin snow cover melted quickly afterwards. It should be noted that the curves before 10:30 on June 25 are not reliable because the glass domes of those upward facing radiometers may be covered by snow.

(1) Global solar radiation and transmissivity

Global solar radiation is the sum of direct and diffuse solar radiation. The direct solar radiation decreased dramatically with increasing cloud amount, but the diffuse solar radiation increased with the cloud amount (Figure 3.6). On a clear day (Figure 3.5a), the diurnal transmissivity varies symmetrically about the solar noon. This results in K↓ closely tracking the extraterrestrial radiation K_0, with maxima at solar noon. The diffuse component was only 8 - 11% of the total during the clear day on Plateau Mountain.

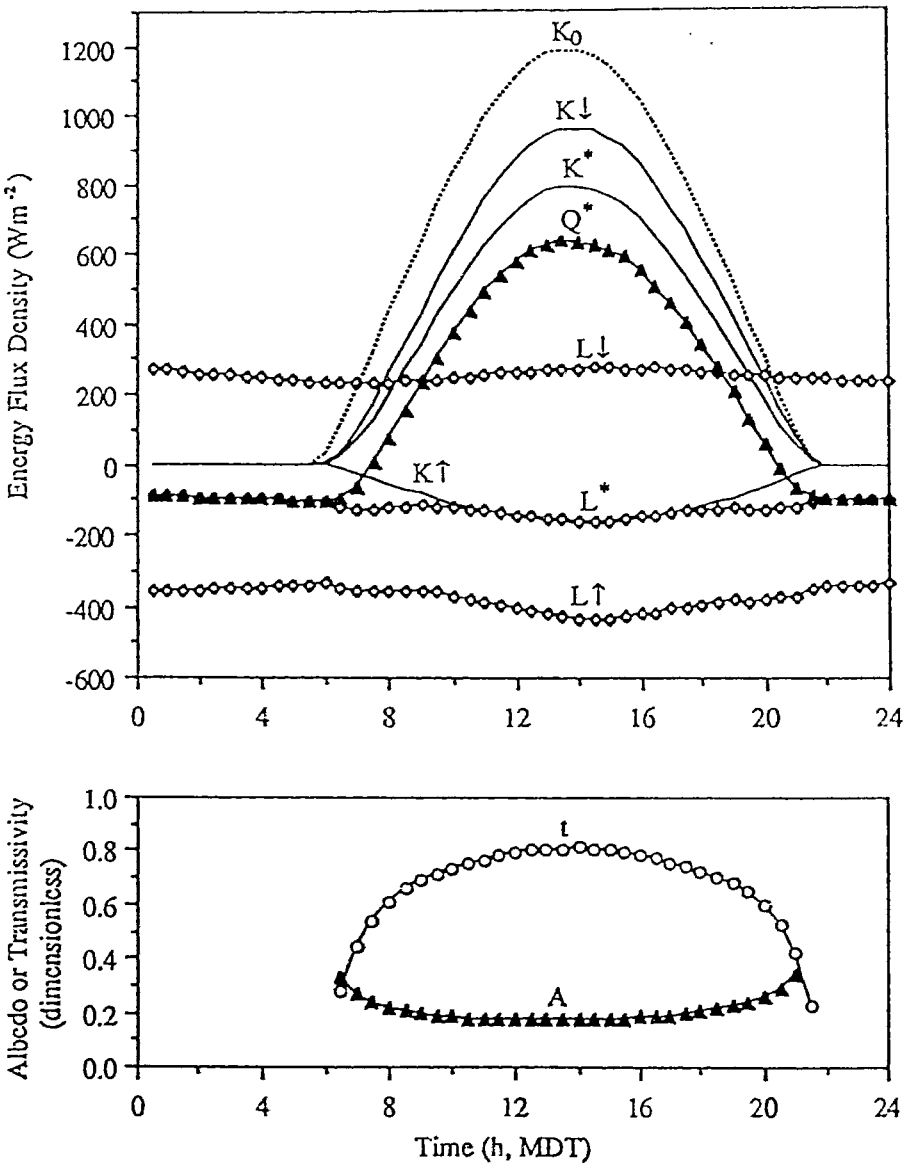

Figure 3.5a Diurnal trends of radiation flux densities, transmissivity and albedo on a clear day, July 21, 1989.

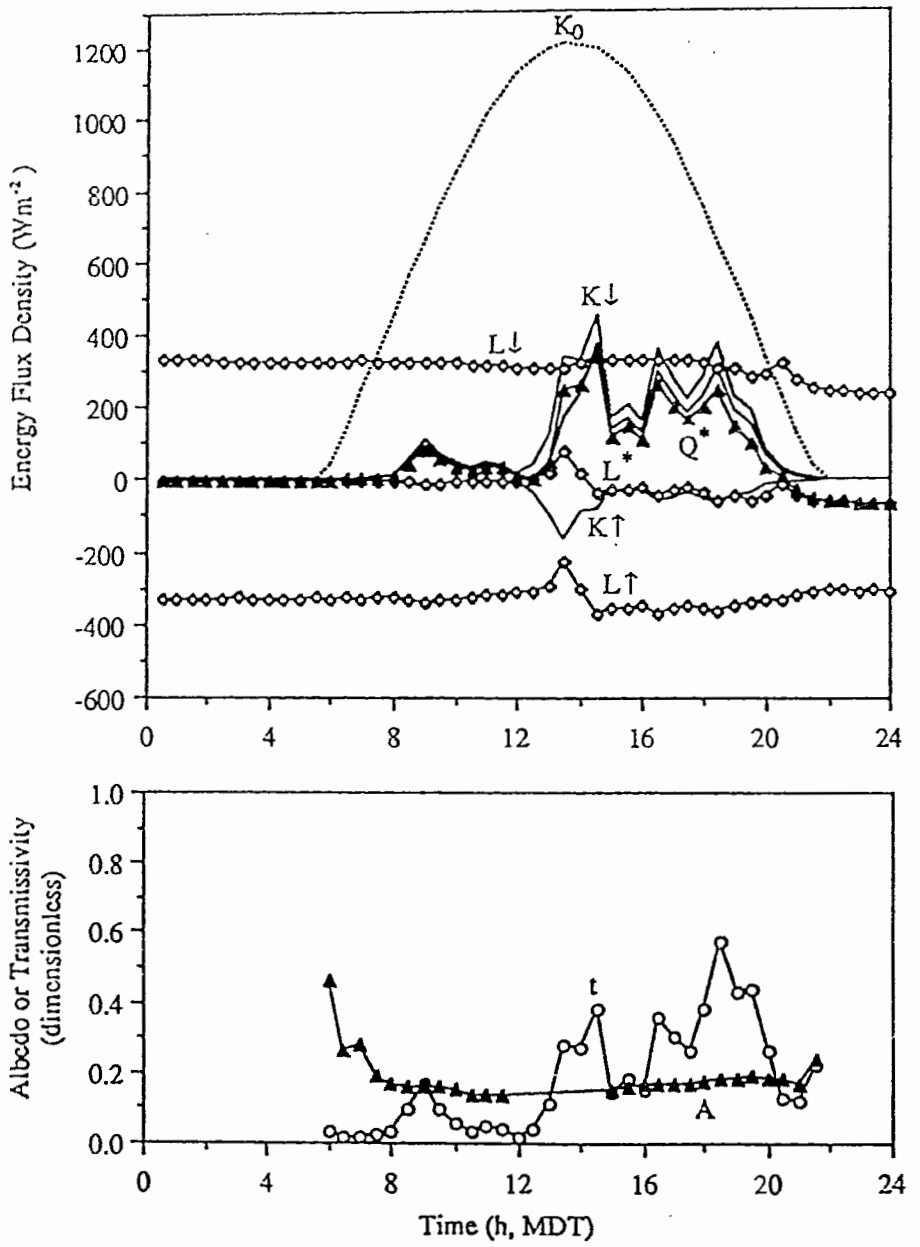

Figure 3.5b Diurnal trends of radiation flux densities, transmissivity and albedo on a cloudy day, July 10, 1989.

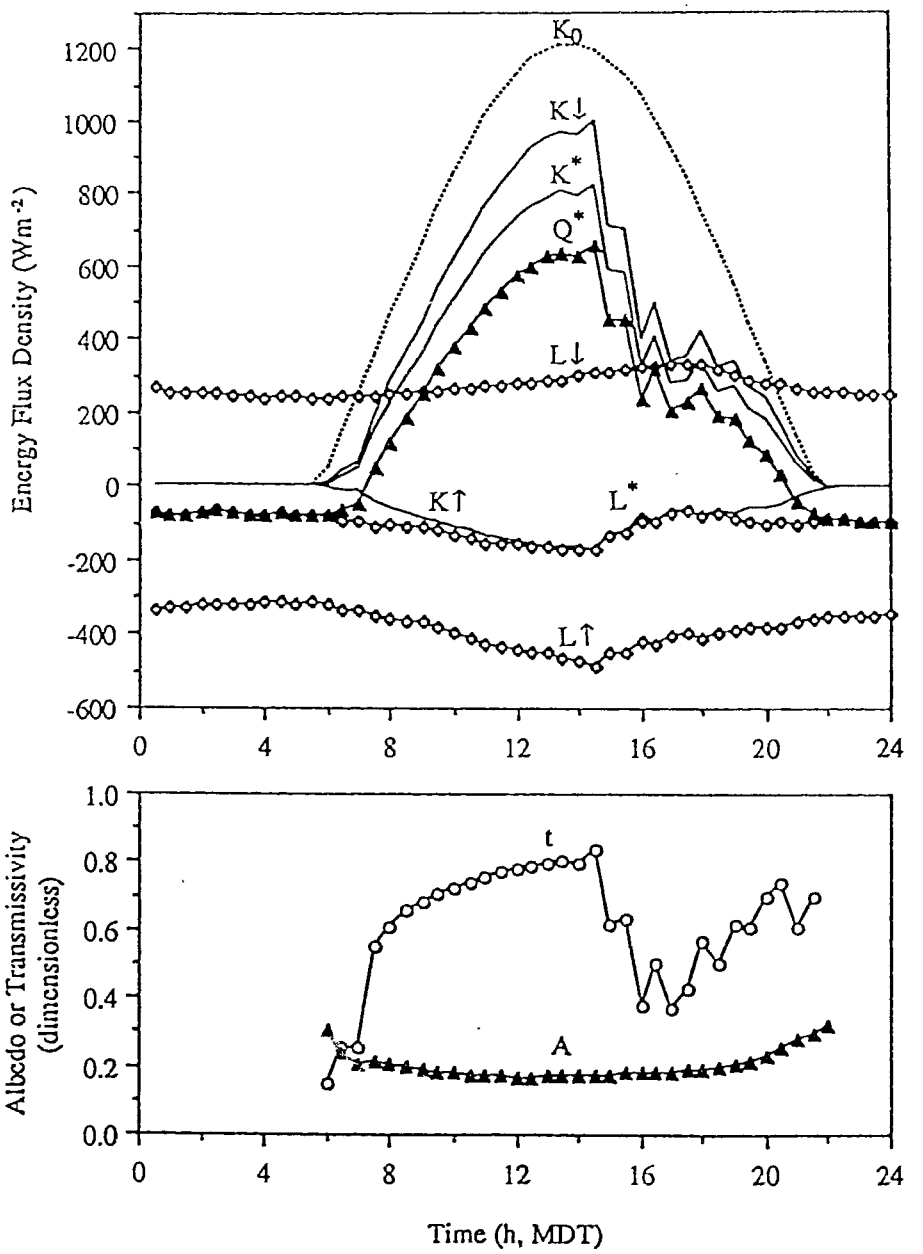

Figure 3.5c Diurnal trends of radiation flux densities, transmissivity and albedo on a day with cloudy afternoon, July 7, 1989.

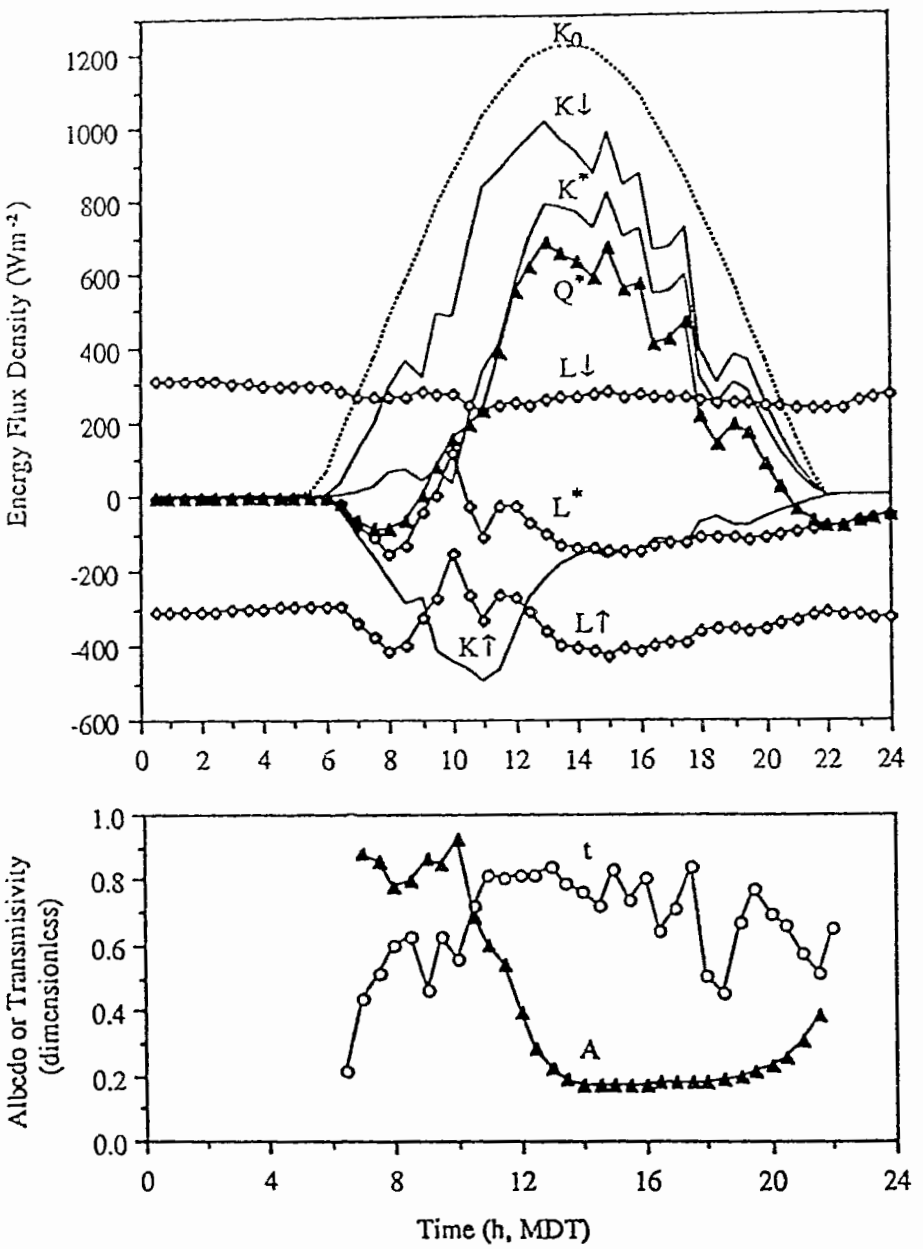

Figure 3.5d Diurnal trends of radiation flux densities, transmissivity and albedo on a day following a snow shower, June 25, 1989.

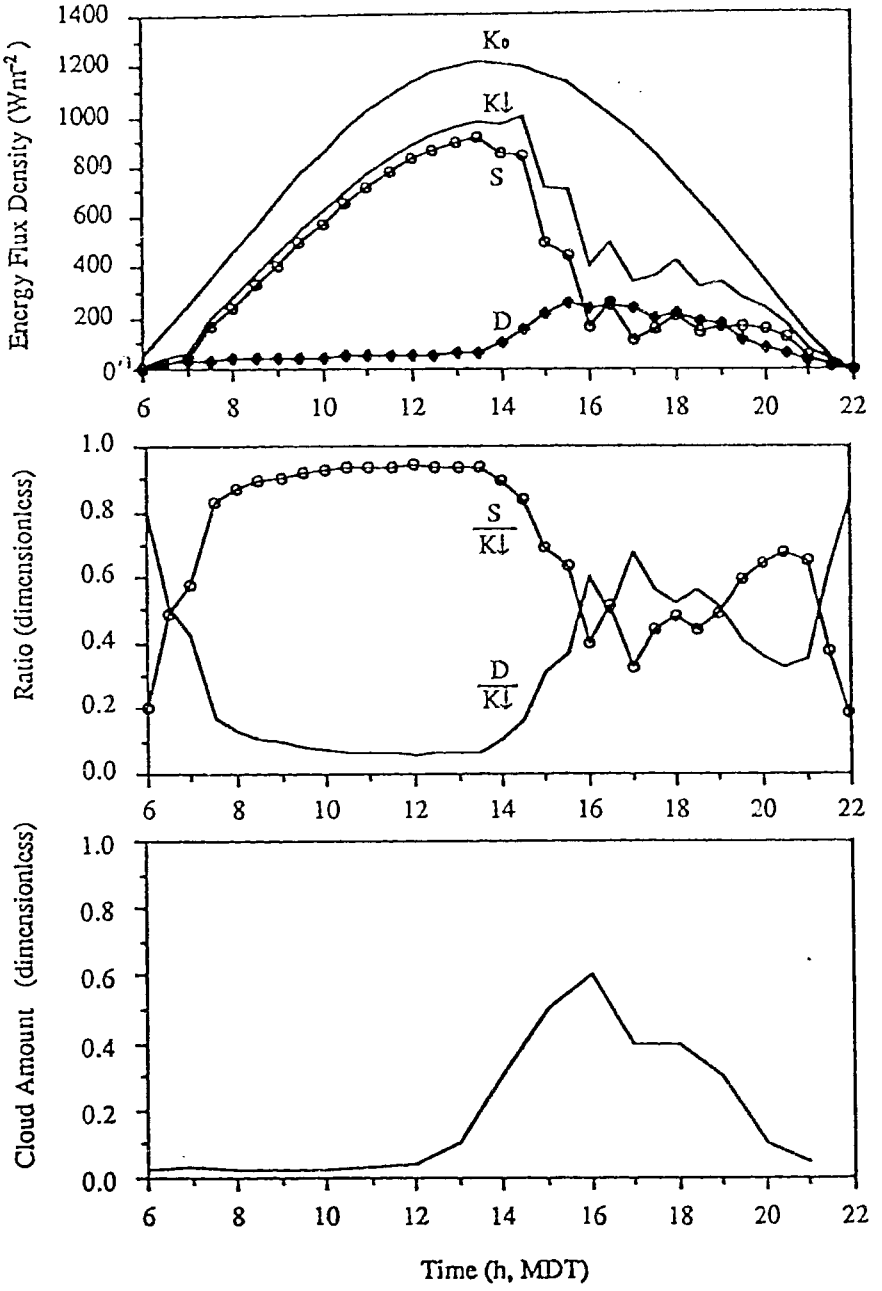

Figure 3.6 Diurnal change of direct and diffuse solar radiation with cloud amount, July 7, 1989.

This is close to the values (0.11 - 0.13) measured in Colorado's Brush Creek Valley (2467 m a.s.l.) (Whiteman et al., 1989) and less than the values at sea level (0.15 - 0.20) (Miller, 1981). The low diffuse component is attributed to the high altitude (reduced atmosphere thickness) and possibly less atmospheric pollutants.

The transmissivity in July is characteristic of days with a cloud buildup (Figure 3.5c). The transmissivity increased steadily until noon and then decreased from above 0.8 to below 0.5 for several hours. As a consequence, K↓ also decreased abruptly from above 900 Wm^{-2} to about 400 Wm^{-2}. This scenario has also been described by a number of other researchers (Lougeay and Brazel, 1982; Olyphant, 1984). Figure 3.5b shows a day with heavy overcast in the morning and some sunny breaks in the afternoon. In the overcast morning, the transmissivity never exceeded 0.20, and K↓ was only diffuse radiation. But in the afternoon, large variation of transmissivity occurred as the cloud cover changed, from 0.03 to as high as 0.60.

(2) Reflected solar radiation and albedo

The albedo of a site depends on the surface characteristics, mainly the vegetation and bare ground at that site. For an anisotropic reflector, reflection will be a function of the incident angle of the solar beam. Figures 3.5a - 3.5d show the reflected solar radiation and albedoes as a function of time. On the day following snow (Figure 3.5d), the albedo was very high (0.75) in the morning. Along with the quickly melting of the snow cover, albedo decreased suddenly and restored to normal (around 0.18). Such scenarios are common at any time in alpine environments. On the days without snow covering the surface, the diurnal variations of albedoes had a similar pattern. The albedoes were relatively invariant in mid-day, but were elevated significantly in the early morning and late afternoon. By careful examination, the albedoes were found to be asymmetric about the solar noon, being slightly higher in the afternoon than in the morning at the same beam incident angle (Figure 3.7). This phenomenon has been noted by an earlier research (Bailey et al., 1989) in the

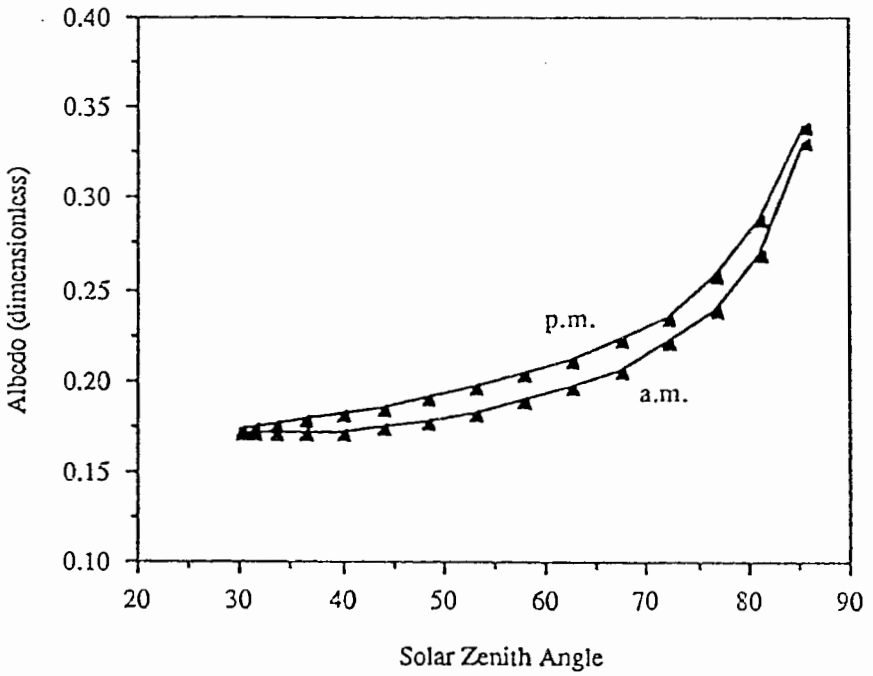

Figure 3.7 Albedo variation with solar zenith angle on a clear day, July 21, 1989.

same site and in other regions (Idso et al., 1969; Nkemdirim, 1972, 1973; Ripley and Redmann, 1976). A number of possible explanations have been suggested for the asymmetry of albedoes. It seems more reasonable to attribute the asymmetry to the prevailing wind patterns which affect the vegetation's angular response to solar irradiance. As for the elevated albedoes near the sunrise and sunset, two possible explanations may be offered. One is that the underlying surface did have some degree of specular reflection at low solar elevations. The other is the instrumental error due to the multi-reflections inside the radiometer domes or the cosine response.

(3) Net solar radiation

As the reflected solar radiation was relatively invariant and was only about 18% of the global solar radiation, K^* closely tracked the global solar radiation $K\downarrow$. When the alpine environment experiences a snow shower in the summer, the diurnal K^* trend could be affected significantly by the rapidly changing albedo. However, this short term event does not have great significance to the longer term radiation budget. But this reminds us of the winter season when the ground is usually snow-covered. During such times, albedo would become a important factor in controlling the daily and seasonal surface radiation regime.

(4) Incoming, outgoing and net longwave radiation

Unlike the solar radiation components, the incoming atmospheric radiation $L\downarrow$ is conservative during day and night, and its daily range rarely exceeds 100 Wm^{-2}. It is the largest energy supplier to the alpine environment over the 24-hour period. This component is especially important during the night and during days of heavy cloud cover when the direct solar radiation is obscured. On the heavy overcast day of July 10 (Figure 3.5b), the daily incoming longwave radiation (26.9 MJm^{-2}) was more than three times the incoming solar radiation (7.9 MJm^{-2}). By examination, $L\downarrow$ did have slight diurnal variation which was associated with the sky condition and air temperature. Under clear skies, $L\downarrow$ was

lower, with its maximum in early afternoon and minimum in early morning. Under cloudy days, however, L↓ varied with cloud amount (see Figure 3.5c).

Although the outgoing longwave radiation emitted by the tundra surface was also conservative day and night, its daily total was the largest of all the daily radiation fluxes. Under clear days, its variation closely tracked net solar radiation, with the maximum around solar noon. It provides a moderating influence to the alpine environment by dissipating the excess heat caused by K^*. On a day with heavy cloud cover, it is nearly invariant. Given the nature of L↓ and L↑, the trend of net longwave radiation is expected, with its maximum net loss around solar noon. During the heavy overcast period of July 10, net longwave loss L^* is close to 0 Wm^{-2}, but it is larger during the clear period.

3.6 Relationship between Global Solar Radiation and Net Radiation

Since both the daily and diurnal change in net longwave radiation and albedo are conservative when the ground is snow-free, a linear relationship between Q^* and K↓ is expected. From the data set obtained in the summer of 1989, the following relationship are obtained (Figures 3.8 and 3.9). For daily data

$$Q^* = 1.18 + 0.471\ K\downarrow \ (MJ\ m^{-2}\ d^{-1}) \quad (n = 28, r^2 = 0.931) \qquad (3.7)$$

and for hourly data

$$Q^* = -48.1 + 0.732\ K\downarrow \ (Wm^{-2}). \quad (n = 450, r^2 = 0.978) \qquad (3.8)$$

These relations are similar to those of Bailey et al.(1989) and Saunders (1990) which are formulated with alpine data. Table 3.3 lists these equations for a ready comparison. Comparing (3.8) with (3.7), it is obvious that the relationship based on hourly average is steeper than that based on daily data. This implies the lower dependence of equation 3.8 on L^*. Therefore it is suggested that equation 3.8 may be more reliable for the purpose of estimating short interval Q^*.

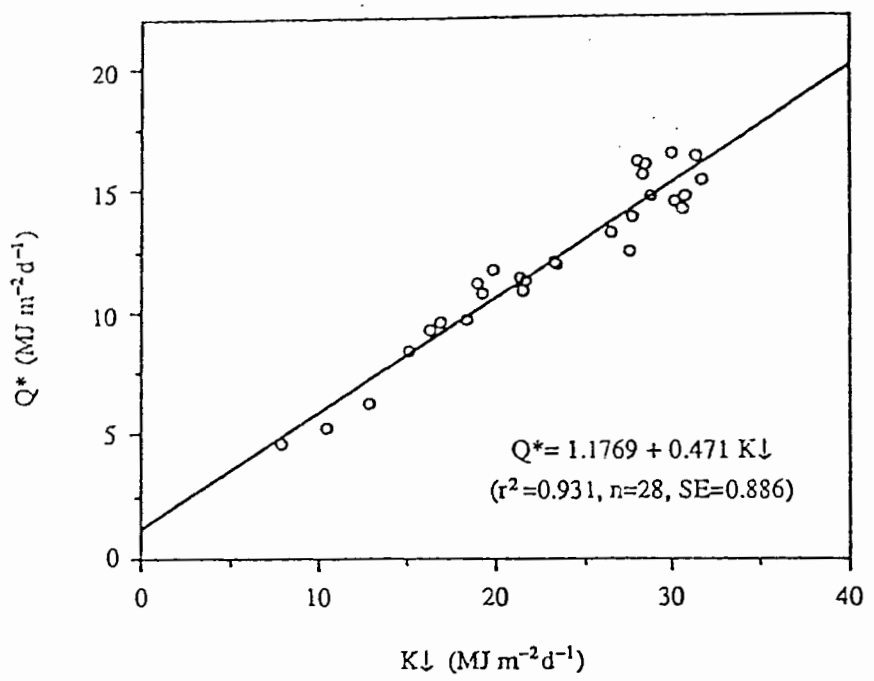

Figure 3.8 Relationship between daily net radiation and global solar radiation.

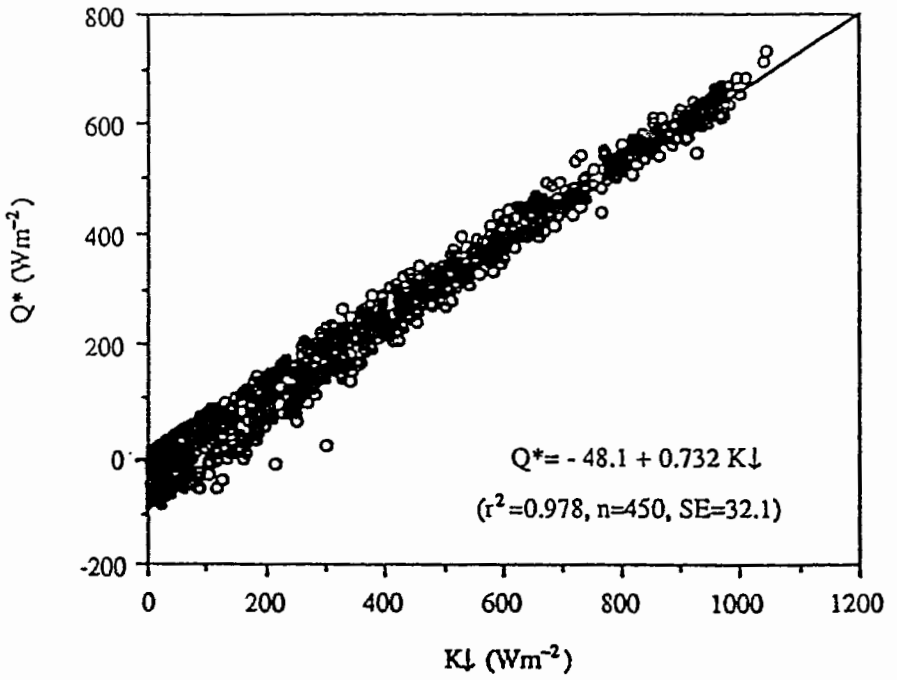

Figure 3.9 Relationship between hourly net radiation and global solar radiation.

Table 3.3 Correlation Equations between Net Radiation and Global Solar Radiation

Authors	Daily Data (MJ m^{-2} d^{-1})	Hourly Data (Wm^{-2})
Davies (1967)	$Q^* = -1.01 + 0.617\ K\downarrow$	
Saunders (1990)	$Q^* = 1.10 + 0.445\ K\downarrow$	$Q^* = -26 + 0.664\ K\downarrow$
Bailey et al. (1989)	$Q^* = 0.98 + 0.514\ K\downarrow$	$Q^* = -57 + 0.680\ K\downarrow$
Isard (1989)		$Q^* = -66 + 0.74\ K\downarrow$
This experiment	$Q^* = 1.18 + 0.471\ K\downarrow$	$Q^* = -48 + 0.732\ K\downarrow$

3.7 Photosynthetically Active Radiation (PAR) and Global Solar Radiation

The wavelength range of solar radiation is 0.3 to 4.0 μm. A portion of the range (0.4 - 0.7 μm) is necessary to determine photosynthesis and is called photosynthetically active radiation (PAR) (Weiss and Norman, 1985). Knowledge of PAR is useful in the study of forest and alpine vegetation. Some reports have presented the measured PAR/K↓ ratios in low altitudes (Szeicz, 1974; Stigter and Musabilha, 1982; Pereira et al., 1982; Weiss and Norman, 1985). But no measurements have yet been made in alpine environments.

According to theoretical and experimental findings, the photosynthetically active portion (PAR/K↓) represents 43% of direct radiation and 57% of diffuse radiation, or 50% of global solar radiation (Yefimova, 1972). The measured PAR/K↓ ratios in the literature vary: extreme values are 0.63 under cloudy conditions and 0.46 under clear sky for solar elevation greater than 20° (Pereira et al., 1982). In an analysis of the theoretical calculations and experimental measurement, Szeicz (1974) showed that the PAR fraction of global solar radiation is nearly constant at 0.50 ± 0.03 and is almost independent of atmospheric conditions and solar elevation. For direct radiation only, PAR/K↓ ratio in very clean air in the summer varies between 0.41 and 0.49 as solar elevation increases from 10° to 40°. For diffuse solar radiation from blue sky the ratio is 0.75. As indicated in the literature, some of the PAR/K↓ ratio variations could be attributed to seasonal factors (Szeicz, 1974; Weiss and Norman, 1985): solar elevation, cloud and time of the day.

The PAR/K↓ ratio measured during this experiment was 0.47 (Figure 3.10). It is approximately equal to the calculated ratio (0.47) above the atmosphere when PAR = 0.3 - 0.7 μm and K↓ = 0.3 - 3.0 μm (Szeicz, 1974). This is low compared with the other reported values. However, this low ratio may be understandable. As light penetrates the atmosphere, differential filtration takes place primarily by water vapour, ozone and carbon dioxide. Water vapour absorbs light primarily above 0.75 μm and its presence would increase the PAR/K↓ ratio. Humidity and temperature tend to decrease with high altitudes,

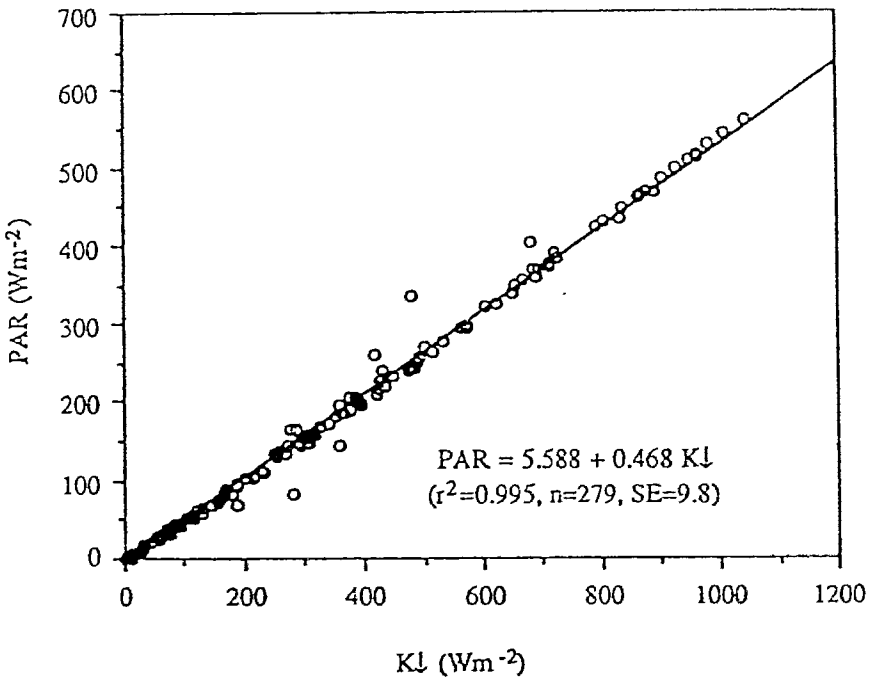

Figure 3.10 Relationship between PAR and the global solar radiation K↓.

consequently decreasing the absolute humidity. This will theoretically decrease the PAR/K↓ ratio. Ozone absorbs light less than 0.75 μm, which would decrease the PAR/K↓ ratio compared with that above the atmosphere. The concentration of ozone is less at the equator than at higher latitudes and thus, as a generality, the PAR/K↓ ratio could be expected to be lower at higher latitudes than lower latitudes.

As shown in Figure 3.10, the linear relationship between global solar radiation and PAR can be expressed as

$$PAR = 0.468\ K\downarrow + 5.6 \qquad (n = 279,\ r^2 = 0.995) \qquad (3.9)$$

Figure 3.11 shows the value of PAR/K↓ on clear day plotted against solar elevation. As Figure 3.11 shows, the scatter is large, but the class means do not change significantly above 10° of solar elevation and remain at a near constant value of 0.47. Figure 3.12 shows the variation of the half-hourly value of PAR/ K↓ with cloudiness represented by the fraction of diffuse radiation to the global solar radiation. The result is when it is partly cloudy, the still intense direct beam solar radiation maintains the PAR/K↓ ratio nearly unchanged. When most of the radiation at the ground is received after transmission through thick clouds, PAR/K↓ is slightly higher.

3.8 Conclusions

This chapter presents the results of radiation budget measurements for the 1989 summer on Plateau Mountain. The period of observation experienced variable weather conditions from overcast to extremely clear with daily transmissivity 0.19 to 0.80. Transmissivity is mainly controlled by atmospheric conditions. Diffuse radiation makes up 8-11% of the global solar radiation during clear days. Daily albedo was essentially constant during the experiment (approximately 0.18). This results in the atmospheric transmissivity controlling the global solar radiation and net solar radiation. An exception exists for theperiod following snow when albedo control becomes very important. As for the asymmetry of albedo about the solar noon, better explanation is still required.

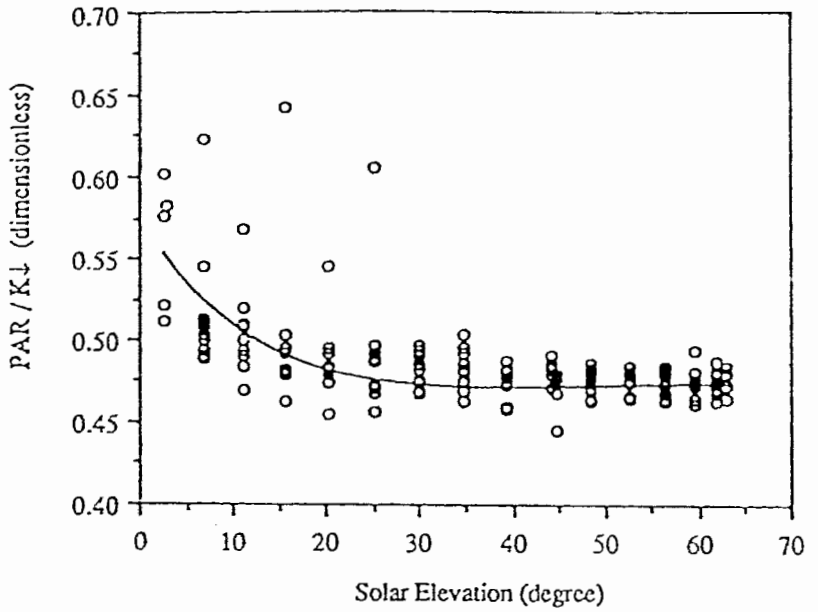

Figure 3.11 PAR / K↓ratio variation with solar elevation angle (curve fitted by hand).

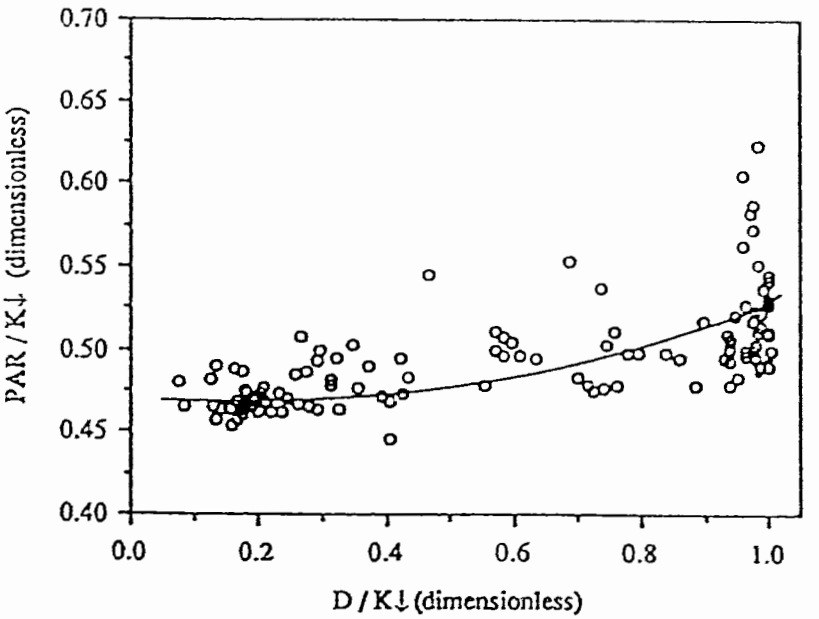

Figure 3.12 PAR / K↓ratio variation with D / K↓ ratio (curve fitted by hand).

The incoming and outgoing longwave radiation is very conservative compared with solar radiation components. Although the outgoing longwave radiation is the largest of all daily averaged radiative fluxes, it is almost counter-balanced by incoming longwave radiation. Therefore, net longwave radiation is much smaller than net solar radiation.

Given the conservative nature of net longwave radiation, the linear relationship between net radiation and global solar radiation was expected. This relationship is not appreciably different from those observed for other surface types.

A strong relationship between photosynthetically active radiation (PAR) and global solar radiation was obtained. PAR makes up 47% of the global solar radiation in this experiment. This value is somewhat low when compared with those reported in the literature. A possible explanation is the higher latitude and altitude of the observation site. Further field measurements of PAR are still needed in alpine environments.

Chapter 4

RADIATION MEASUREMENTS FROM SLOPING SURFACES ON PLATEAU MOUNTAIN, ALBERTA, CANADA

4.1 Introduction

Although a lot of radiation budget studies have been undertaken in selected mountain regions, few have measured the radiation budget on sloping surfaces. This chapter will summarize the differences in radiation budget components between a site on an unobstructed horizontal surface and four sites on sloping surfaces.

4.2 Theoretical Background

Mountainous environments consist of horizontal surfaces and sloping surfaces with different inclinations and orientations. The radiation budget of a horizontal surface was discussed in Chapter 3. The radiation budget of a sloping surface Q_s^* is the sum of net solar radiation K_s^* and net longwave radiation L_s^* received on the slope

$$Q_s^* = K_s^* + L_s^* = (K_s\downarrow - K_s\uparrow) + (L_s\downarrow - L_s\uparrow) \qquad (4.1)$$

where $K_s\downarrow$ is the global solar radiation, $K_s\uparrow$ the reflected solar radiation, $L_s\downarrow$ the incoming longwave radiation and $L_s\uparrow$ the outgoing longwave radiation. The subscript s denotes that the flux densities are on the sloping surfaces.

$K_s\downarrow$ is composed of three components

$$K_s\downarrow = S_s + D_s + K_t \qquad (4.2)$$

where S_s and D_s are the direct and diffuse solar radiation to the slope respectively, and K_t the incoming solar radiation from the reflection of surrounding terrain. $K_s\uparrow$ is dependent on $K_s\downarrow$ and the surface albedo.

$L_s\downarrow$ is composed of two components

$$L_s\downarrow = L_{as} + L_{ts} \qquad (4.3)$$

where L_{as} is the longwave radiation from the atmosphere and L_{ts} the longwave radiation from the surrounding terrain. Outgoing longwave radiation $L_s\uparrow$ is determined by surface temperature T_s and surface emissivity ε according to the Stefan-Boltzmann law (Oke, 1987)

$$L_s\uparrow = \varepsilon \sigma T_s^4 + (1 - \varepsilon) L_s\downarrow \qquad (4.4)$$

where σ is the Stefan-Boltzmann constant. For alpine tundra surfaces, the surface emissivity ranges between 0.90 and 0.99 and for grass it ranges between 0.90 and 0.95 (Oke, 1987). Snow and ice surfaces can be treated as blackbody emitters with emissivity from 0.97 to 0.99 (Muller, 1985).

4.3 Observational Procedure

The experiment site was on Plateau Mountain which is located in the Livingstone Range of the Rocky Mountains in southwestern Alberta, Canada, at about 50°13' N and 114°31' W. A horizontal site was on the unobstructed summit area and four sloping sites were on slopes facing north, east, south and west. The details of the sites were given in Chapter 1.

Due to the resource limitations, only two measurement systems were used in this experiment. One system was kept in operation at the horizontal site throughout the experiment from June 20 to July 24, 1989. The other one was operated continuously for a period of about one week on each of the four sloping sites, which ensured at least one cloudy day and one clear day in each period. The dates of operation are presented in Table 1.1.

The horizontal site system was installed with instruments as described in Chapter 3. On sloping sites, global solar radiation was measured by an Eppley PSP Precision pyranometer. Reflected solar radiation measurements were made by a downward-looking Middleton CN-7 pyranometer. Incoming longwave radiation was measured with an Eppley pyrgeometer. Net radiation was measured by a Middleton CN-1 net pyrradiometer.

With the above measurements, outgoing longwave radiation is calculated as a residual from Equation 4.1.

All radiometers were mounted on a tripod. The tripod can be adjusted according to the slope angle and slope orientation, so that all the receiving surfaces of the radiometers were parallel to the sloping surface. Surface temperature was measured by two thermocouple arrays (each has ten thermocouples connected in parallel). These thermocouple arrays had the same problem as described in Chapter 3, i.e. when they were partially exposed to direct sunshine, they overestimated the surface temperature. However, when it was overcast or during the night, they worked well. It is suggested that the thermocouples should be very fine so that the radiative heating of the thermalcouple could be neglected.

All data were recorded and processed by a Campbell Scientific 21X datalogger. The datalogger was programmed to yield half-hourly output averages. The datalogger was placed in an environmental enclosure.

Post-experiment radiation sensor intercomparison was performed in the field. The intercomparison between the two systems revealed that there were no significant differences. Error analysis for all the radiometers and thermocouple arrays is presented in Appendix II.

4.4 Solar Radiation

The whole observation period encountered variable weather. From each of the four observation periods, one clear and one cloudy day are chosen for comparison of the diurnal change of radiation components. In this way eight days were selected. Figures 4.1 through 4.5 show the diurnal trends of the radiation components on the horizontal and sloping sites. Time integrations of the diurnal curves (or the daily totals) are summarized in Table 4.1. Since the sloping sites and the horizontal site are close to each other (less than 2 km apart), it is assumed that the sky conditions over the horizontal site and sloping sites have no significant difference on an hourly or longer time basis. Therefore the differences in

incoming radiation can be attributed to mainly the effects of slope angle, slope orientation and surrounding terrain shading.

(1) Shading and local sunrise/sunset

Local sunrise (LSR) and sunset (LSS) marked the receipt of direct solar radiation. Since the sloping sites were shaded from the sun by both the surrounding terrain and slope itself, LSR and LSS were delayed or advanced from astronomical calculations in all slopes except for the 30° north slope (Figures 4.1a). As a consequence, the sunshine hours of sloping surfaces were reduced with respect to that of horizontal site. LSR and LSS of a slope depend on the geometrical relation between the slope facet and the position of the sun.

Generally speaking, LSR is delayed on west-facing slopes and LSS is ahead on east-facing slopes in the summer season. The steeper the slope is, the longer the LSR and LSS are delayed or advanced from their astronomical calculations. For this experiment, LSR on west sloping site was delayed by about 2 hours. Sunrise on east-facing sloping site was delayed half an hour due to terrain shading in front of the slope, and LSS was ahead approximately by 3 hours.

For a south-facing slope during the summer season, the sunshine hours decrease with the increase of slope angle. This means either LSR is delayed or LSS is ahead or both. In the current experiment, LSR was delayed by about 2 hours. The LSR and LSS of north-facing slope equalled those of unobstructed horizontal surfaces.

Small amounts of diffuse solar radiation were received at the east, west and south sloping sites between the local and astronomical sunrise and sunset. Only the delay in receiving much larger direct solar radiation was critical to daily radiation totals. This principle is applicable to the effect of shading on solar radiation. For east slope, surrounding terrain shading is more important in the morning when the slope orientation is more favorable to the sun. For the west slope, it is more important in the afternoon.

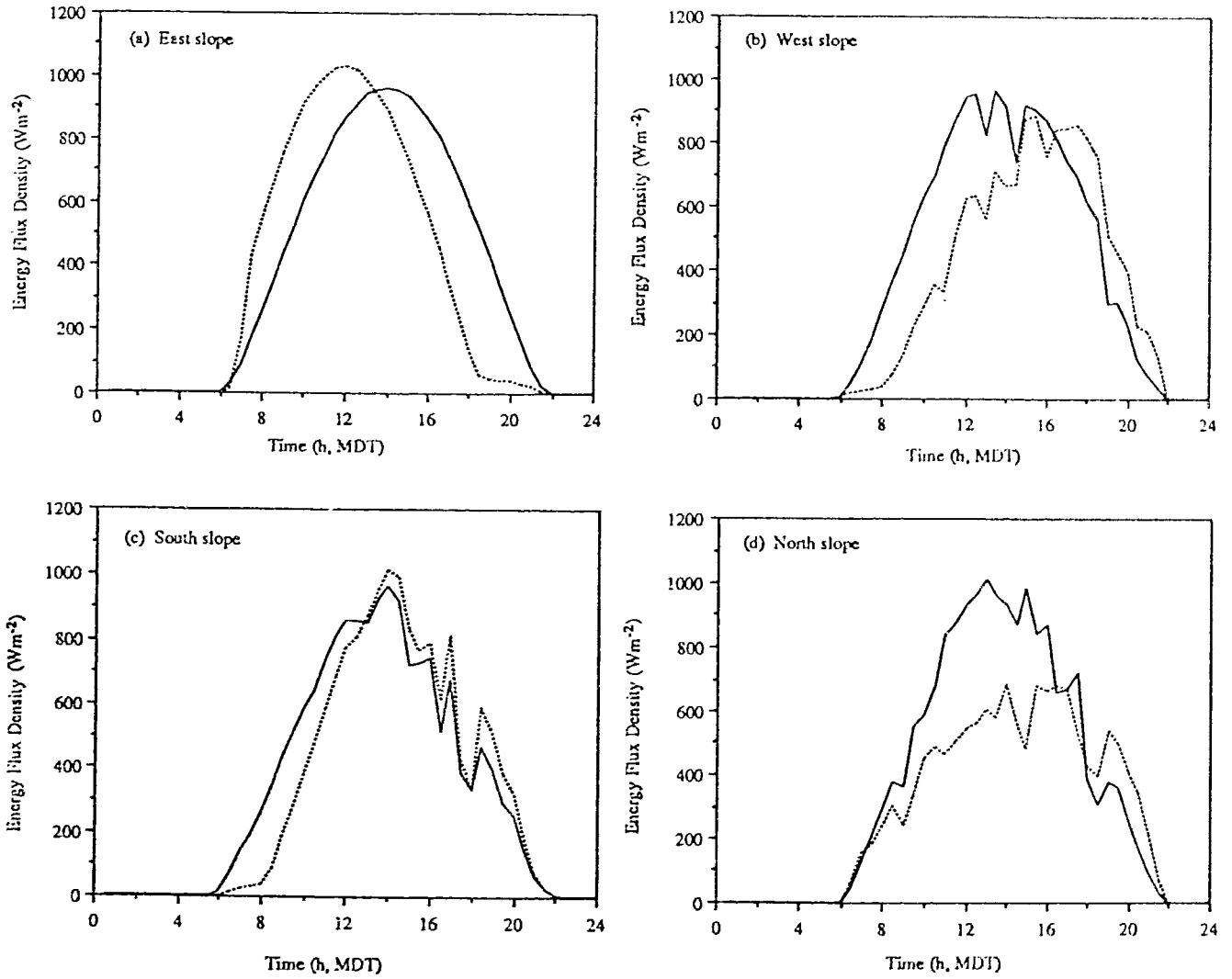

Figure 4.1a Diurnal trends of global solar radiation on selected clear days. The solid lines are for horizontal site and the dotted lines for sloping sites. (a) July 21; (b) July 8; (c) July 12 and (d) June 25.

Table 4.1 Summary of Radiation Budget Components on Selected Days (unit: $MJm^{-2}d^{-1}$)

Slope	Date	Sky	$K\downarrow$	$K_s\downarrow$	$K\uparrow$	$K_s\uparrow$	K^*	K_s^*	$L\downarrow$	$L_s\downarrow$	$L\uparrow$	$L_s\uparrow$	L^*	L_s^*	Q^*	Q_s^*
north	June 24	overcast	10.5	11.8	1.8	2.2	8.7	9.7	25.3	25.4	28.7	28.5	-3.4	-3.1	5.3	6.5
north	June 25	clear	30.6	23.2	10.7	10.8	19.9	12.3	23.1	23.0	28.8	25.8	-5.7	-2.8	14.2	9.5
south	July 10	overcast	7.9	8.3	1.8	1.8	6.1	6.4	26.9	27.0	28.4	28.2	-1.5	-1.2	4.6	5.2
south	July 12	clear	28.5	26.6	5.1	5.3	23.4	21.4	25.8	26.2	33.1	32.0	-7.4	-5.8	16.0	15.4
west	July 1	cloudy	21.3	16.7	3.9	3.0	17.5	13.7	23.1	23.4	29.1	28.7	-6.0	-5.3	11.4	8.4
west	July 8	clear	31.4	26.0	5.8	4.6	25.6	21.3	21.7	22.3	30.9	30.3	-9.3	-8.0	16.3	13.2
east	July 17	cloudy	16.2	9.9	2.9	1.8	13.2	8.1	25.8	27.0	29.9	30.3	-4.0	-3.3	9.2	4.7
east	July 21	clear	31.6	29.4	5.9	5.0	25.6	24.4	21.9	24.1	32.3	33.3	-10.4	-9.1	15.3	15.1

(2) Global solar radiation

Global solar radiation of unobstructed horizontal surfaces is the sum of direct and diffuse solar radiation from the sky hemisphere. But for the sloping surfaces, it should include the reflection of solar radiation from surrounding terrain within the view of sloping surface. However, for most surfaces when the slope is smaller than 20°, the reflection is very small and can be neglected (Fu, 1983).

Direct solar radiation can be treated as a vector quantity, and it plays a key role in forming the topoclimates. Strong climatic contrasts are generated on sloping surfaces of different inclinations and orientations relative to the sun. On a clear day, the direct component makes up to 80 - 85% of the incoming solar radiation (see Chapter 3) on Plateau Mountain. As cloudiness increased, the direct component decreased and this decrease was partly compensated by the increase of diffuse radiation. Thus, the total amount of solar radiation decreased.

Figures 4.1a - 4.1b show the diurnal trends of global solar radiation on the selected days. All the four sloping sites were shaded only slightly by surrounding terrain. Therefore, most of the differences on the diurnal trends were attributed to the effect of slope themselves. The LSS was 3 hours ahead on the east sloping site and the LSR was delayed by 2 hours on the west and south sloping sites on clear days (Figures 4.1a and 4.1b). Although the sunshine hours of the east sloping site were reduced significantly, the total solar radiation rivaled the corresponding horizontal site value (Table 4.1) because of its favorable orientation relative to the sun. Since the south sloping site was only 22° and had a southwest orientation, its daily total was close to that of the horizontal site as well. This is consistent with the theoretical analyses made by Fu (1983). The north slope site experienced the same sunshine hours as the horizontal site, but received less solar radiation due to the slope effect on the strong direct radiation.

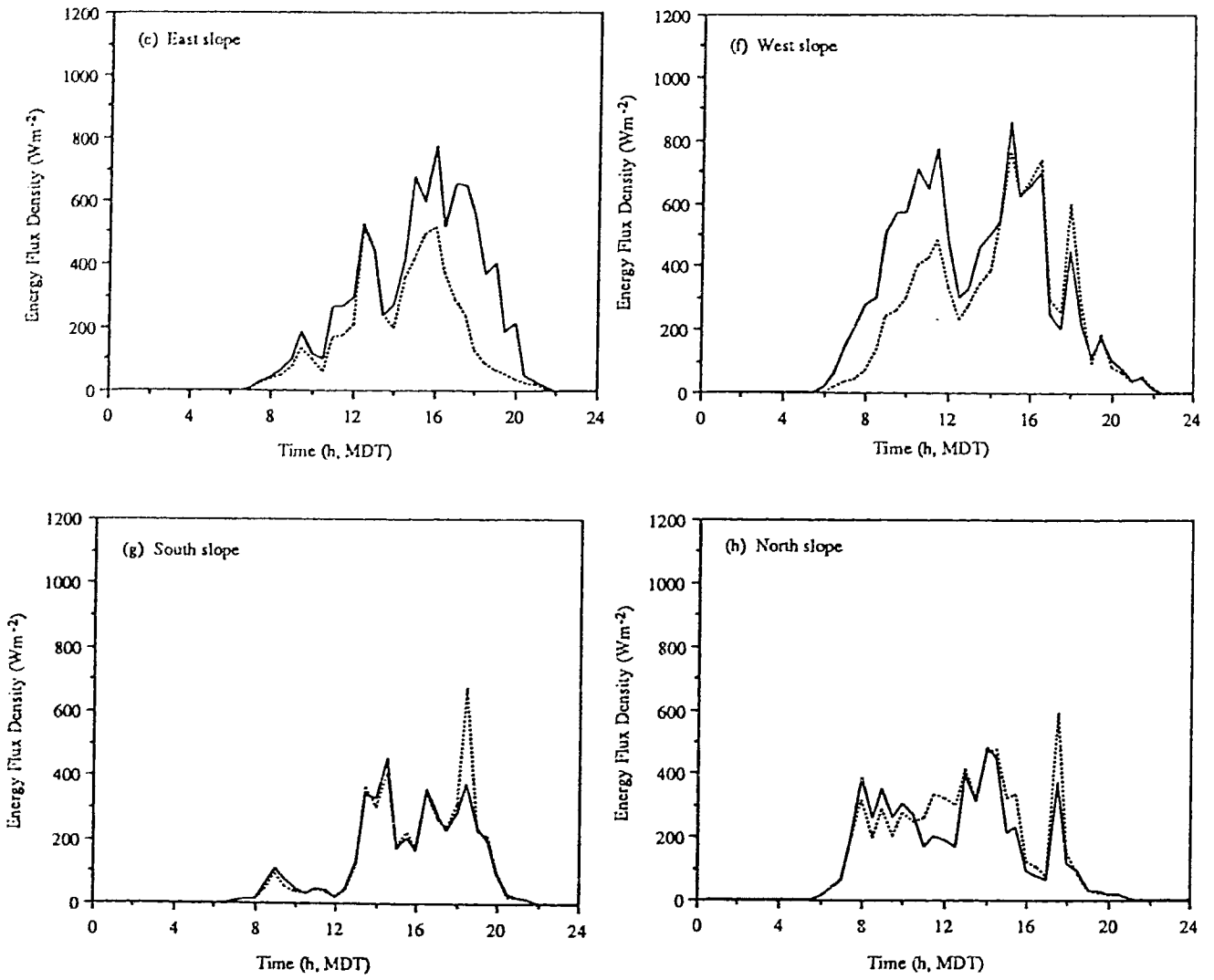

Figure 4.1b Diurnal trends of global solar radiation on selected clear days. The solid lines are for horizontal site and the dotted lines for sloping sites. (a) July 17; (b) July 1; (c) July 10 and (d) June 24.

When the days were overcast, such as that of June 4 and July 10 (Figures 4.1b), the difference of global solar radiation between horizontal site and sloping sites becomes small. This is obviously attributed to the decrease of direct solar radiation and the increase of more isotropic diffuse solar radiation.

(3) Reflected and net solar radiation

Reflected solar radiation is a function of global solar radiation and surface albedo. Figures 4.2 (a) through 4.2 (d) show the diurnal trends of albedo on sloping sites and the horizontal site. Since the albedo was relatively invariant during the day when the surface was snow-free, the diurnal trend of reflected solar radiation was similar to that of global solar radiation. This does not hold true when the surface albedo experienced large changes, such as on June 25 following a snow shower.

The horizontal site albedo was characterized by its invariance during the midday with increasing values near the sunrise and sunset. This has been discussed by previous studies (Whiteman et al., 1989; Bailey et al., 1989) and the elevated albedo near local sunrise and sunset was attributed to the specular reflection. This interpretation is also suitable for the sloping site albedoes. The period of steady albedo was shown on both the horizontal site and the sloping sites, which may be caused by nearly isotropic reflection when the solar beam incident angle to the surface is small.

Figure 4.2 (d) shows the albedo change on the north sloping site after a snow shower. When the snow cover existed, the surface exhibited strong spectral reflection and the albedo of north sloping site was far higher than the horizontal site albedo. With the rapid melting of snow, both albedoes reduced to normal.

Figure 4.3 presents the relationships between albedo and solar elevation angle with respect to slope (h_s). The albedo of east, west and south slope are symmetrical about the maximum h_s, which means the albedoes are approximately the same in the morning and afternoon at the same solar beam incident angle. Figure 4.3 also reflected the fact that south

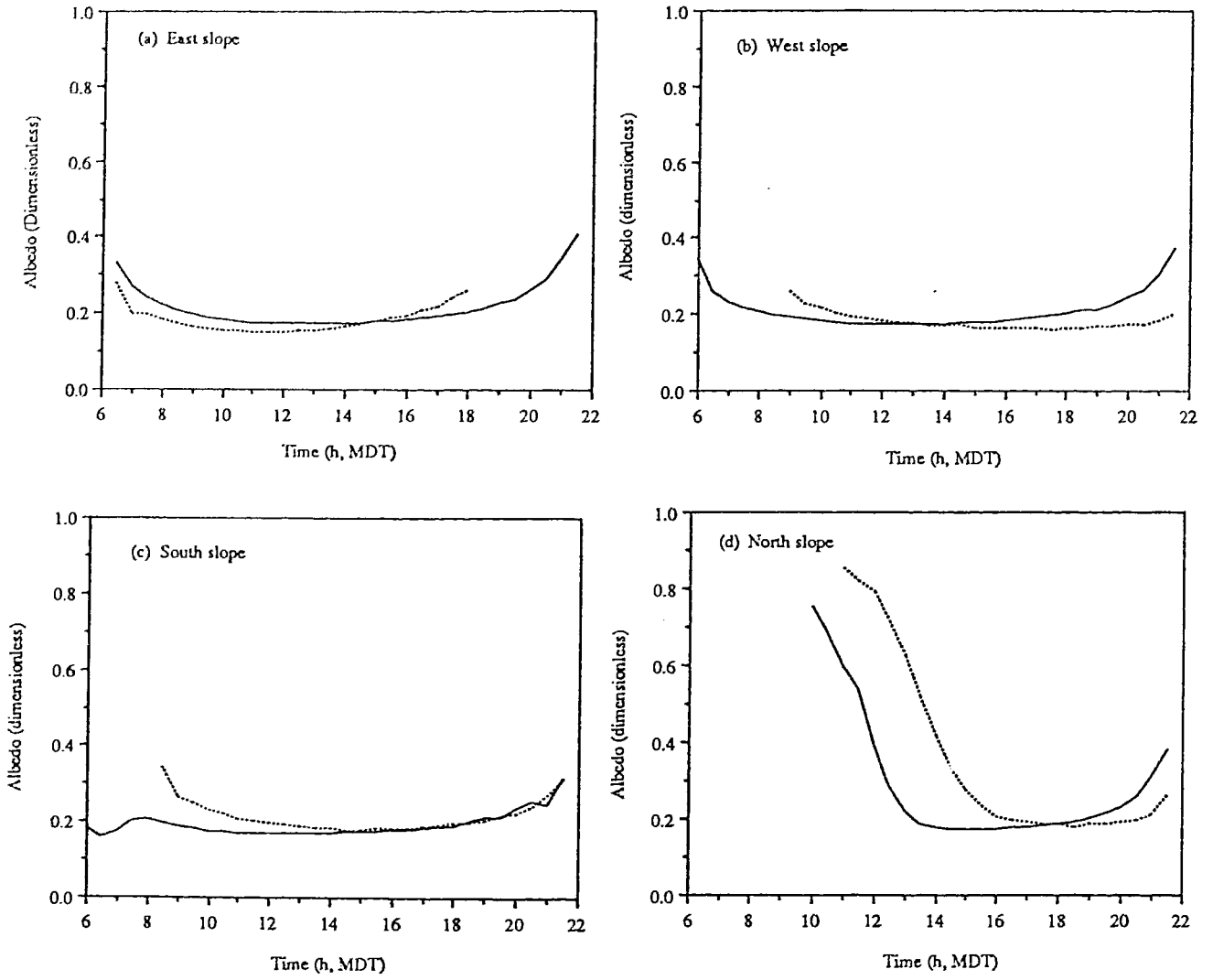

Figure 4.2 Diurnal trends of albedo on selected clear days. The solid lines are for horizontal site and the dotted lines for sloping sites. (a) July 21; (b) July 8; (c) July 12 and (d) June 25.

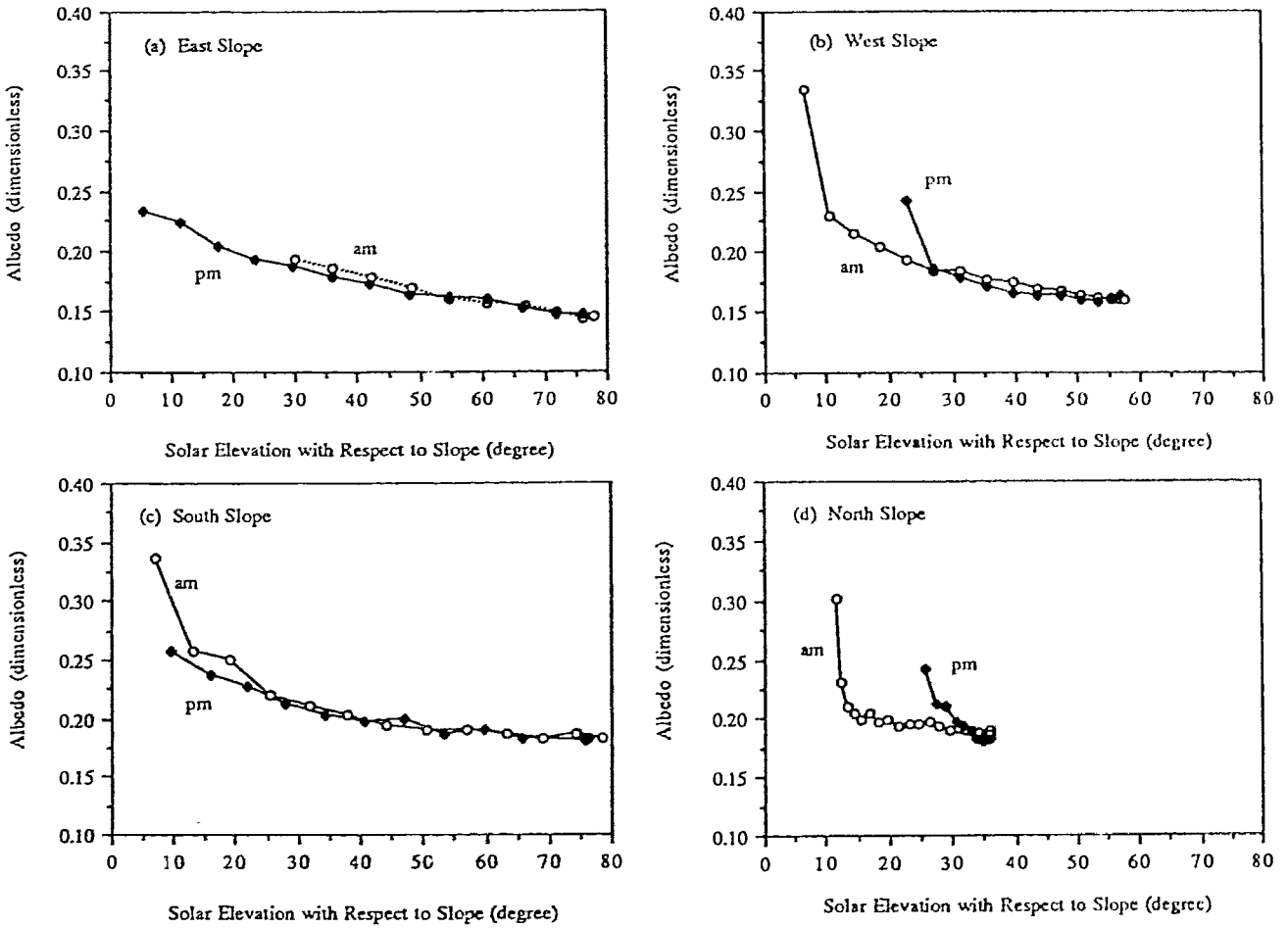

Figure 4.3 The relationship between albedo and solar elevation angle with respect to (a) east slope; (b) west slope; (c) south slope and (d) north slope.

and east facing slopes in this experiment have more favorable orientations relative to the sun. Solar elevation angle with respect to slope h_s ranges from 0 to 79° for the south slope and 0 to 78° for the east slope, while it ranges 0 to 63° on horizontal surface. The resulting daily global solar radiation totals of the sloping sites and the horizontal site are very close.

Since reflected solar radiation was only about 18% of the global solar radiation when the surface was snow-free, net solar radiation was dominated by global solar radiation. Therefore the differences between the sloping sites and the horizontal site reflected on the incoming solar radiation hold true for net solar radiation.

4.5 Longwave Radiation

(1) Incoming longwave radiation

Incoming longwave radiation is the largest energy supplier for mountain environments through a 24-hour period (Bailey et al., 1989; Whiteman et al., 1989). Compared with the solar components, it is relatively conservative throughout the day and night. On the unobstructed horizontal site, the incoming longwave radiation comes from the sky hemisphere. Under clear skies, the diurnal trend of incoming longwave radiation tracked the atmospheric temperature with the maximum around early afternoon (when the air temperature reached maximum) and minimum in early morning (Figures 4.4 (a)-4.4 (d)). Under cloudy skies, this trend became irregular because of the effect of clouds. On the sloping sites, however, the longwave radiation comes from both the atmosphere and the surrounding terrain. The fraction from the two sources depends on the relative fractions of the sky and ground seen in the viewing hemisphere of the sloping surface. The sky view factors of the five sites, which is defined as the ratio of sky and viewing hemisphere, are listed in Table 1.1. The longwave radiation received on a sloping surface depends on both atmospheric temperature and emissivity and surrounding terrain temperature and emissivity. The relative degree of dependence on atmosphere or surrounding terrain emissivity and temperature is related to the sky view factor, f. When f is large, sky view is

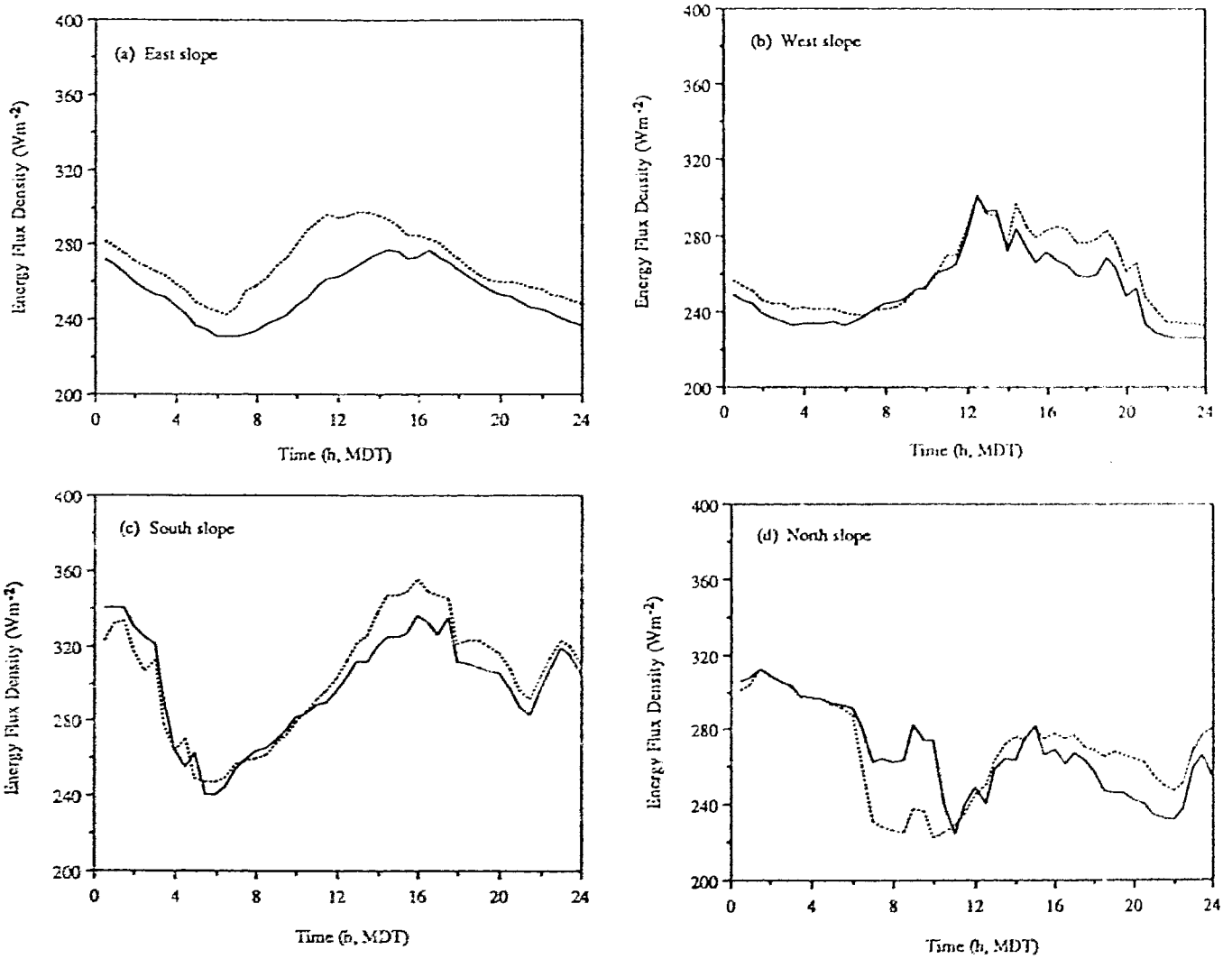

Figure 4.4 Diurnal trends of incoming longwave radiation on selected clear days. The solid lines are for horizontal site and the dotted lines for sloping sites. (a) July 21; (b) July 8; (c) July 12 and (d) June 25.

more open, and $L_s\downarrow$ depends on mainly atmospheric temperature and emissivity. When f is small, i.e., steep slopes or heavily shaded area, surrounding terrain temperature and emissivity become more important. Since all of the four sloping sites have large sky view factors, the longwave radiation on those sloping sites has no significant difference from the unobstructed horizontal site (Figures 4.4 (a) - 4.4 (d)).

Outgoing longwave radiation acts as a moderating factor for the environment in that it dissipates the large positive net solar energy gain during the daylight hours. The surface outgoing longwave radiation depends on surface temperature and surface emissivity. As indicated before, surface emissivity ranges from 0.90 to 0.99 for alpine tundra surfaces. Therefore the diurnal trends of outgoing longwave radiation depended mainly on surface temperature and has the same characteristics of surface temperature (Figure 4.5). The longwave radiation was at a minimum at all sites just after the astronomical sunrise, and then rose and approached their maximums at different times which is determined by the maximum net solar radiation values. Despite the diurnal trend differences, the daily totals of outgoing longwave radiation show no significant difference between sloping and horizontal surfaces.

Given the nature of incoming and outgoing longwave radiation, net longwave radiation is as expected. Since outgoing longwave radiation was partly counterbalanced by the incoming longwave radiation, net longwave radiation was generally negative and much smaller than net solar radiation (Figure 4.6). Figure 4.6 (d) showed that at the north sloping site on June 25, the net longwave radiation was positive during the period of 12:00 to 14:00 MDT. This rare scenario can be understood when considering the very low surface temperature following the snowmelt.

4.6 Net Radiation

During the daytime, net radiation was dominated by net solar radiation, and consequently by global solar radiation. It was equivalent to net longwave radiation at night.

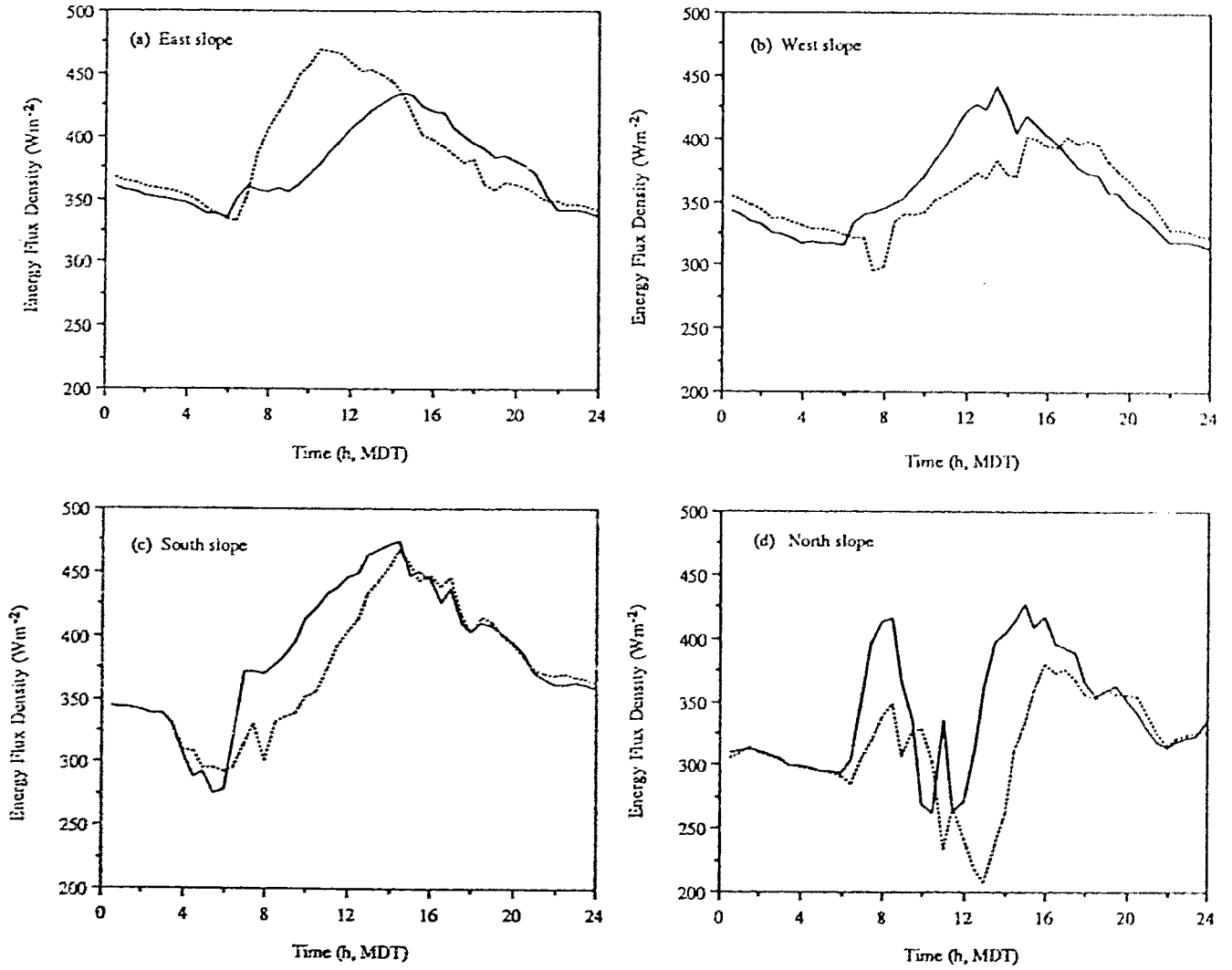

Figure 4.5 Diurnal trends of outgoing longwave radiation on selected clear days. The solid lines are for horizontal site and the dotted lines for sloping sites. (a) July 21; (b) July 8; (c) July 12 and (d) June 25.

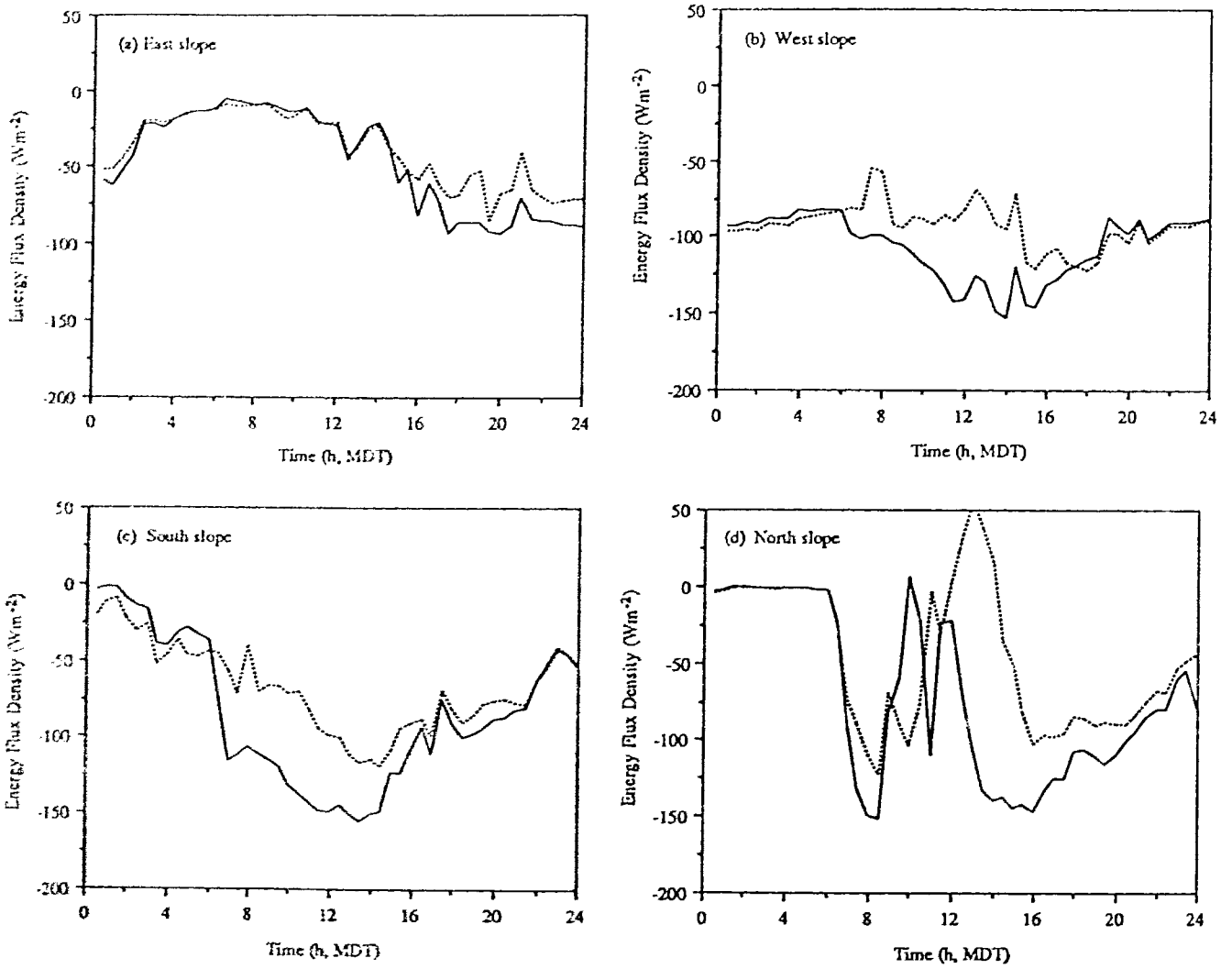

Figure 4.6 Diurnal trends of net longwave radiation on selected clear days. The solid lines are for horizontal site and the dotted lines for sloping sites. (a) July 21; (b) July 8; (c) July 12 and (d) June 25.

Therefore, net radiation on both horizontal and sloping sites was a large positive value during the day and a small negative value at night. The differences in net radiation between sloping sites and the horizontal site are primarily related to the receipt of direct beam solar radiation and thus depend strongly on slope inclination and slope orientation as well as the shading from surrounding terrain. On clear days, the differences were clearly shown on the diurnal trends. On cloudy days, the contrasts became less because of the obscured direct solar radiation (Figure 4.7).

Using the hourly average data set obtained on the four sloping sites, the relationships between net radiation and global solar radiation are obtained for the sloping surfaces (Table 4.2). Comparing these relationships with that obtained in Chapter 3, it is apparent that the linear relationship between net radiation and global solar radiation exists for both the horizontal surface and sloping surfaces. A statistical analysis of the slope and intercepts of the equations showed that the differences between the equation for horizontal site and that for sloping site were not significant. This means that the equation developed with data on horizontal surface could be used for sloping surfaces.

4.7 Conclusions

Radiation measurements were made on the horizontal surfaces of Plateau Mountain during a period following the summer solstice. The radiation regime on a horizontal site during the period is presented in Chapter 3. This current chapter summarizes the differences of radiation components between sites on a horizontal surface and sloping surfaces. Since the radiation measurement system was operated for only 6-8 days on each of the sloping surfaces, the analysis of day-to-day radiation regimes on the sloping surfaces is difficult. Nevertheless, the half-hourly average data show differences of radiation budget between horizontal and sloping sites. The differences between the horizontal surface and sloping surfaces are mainly caused by the receipt of solar radiation, instead of the relatively conservative longwave radiation. Consequently, radiation budget and its components differ

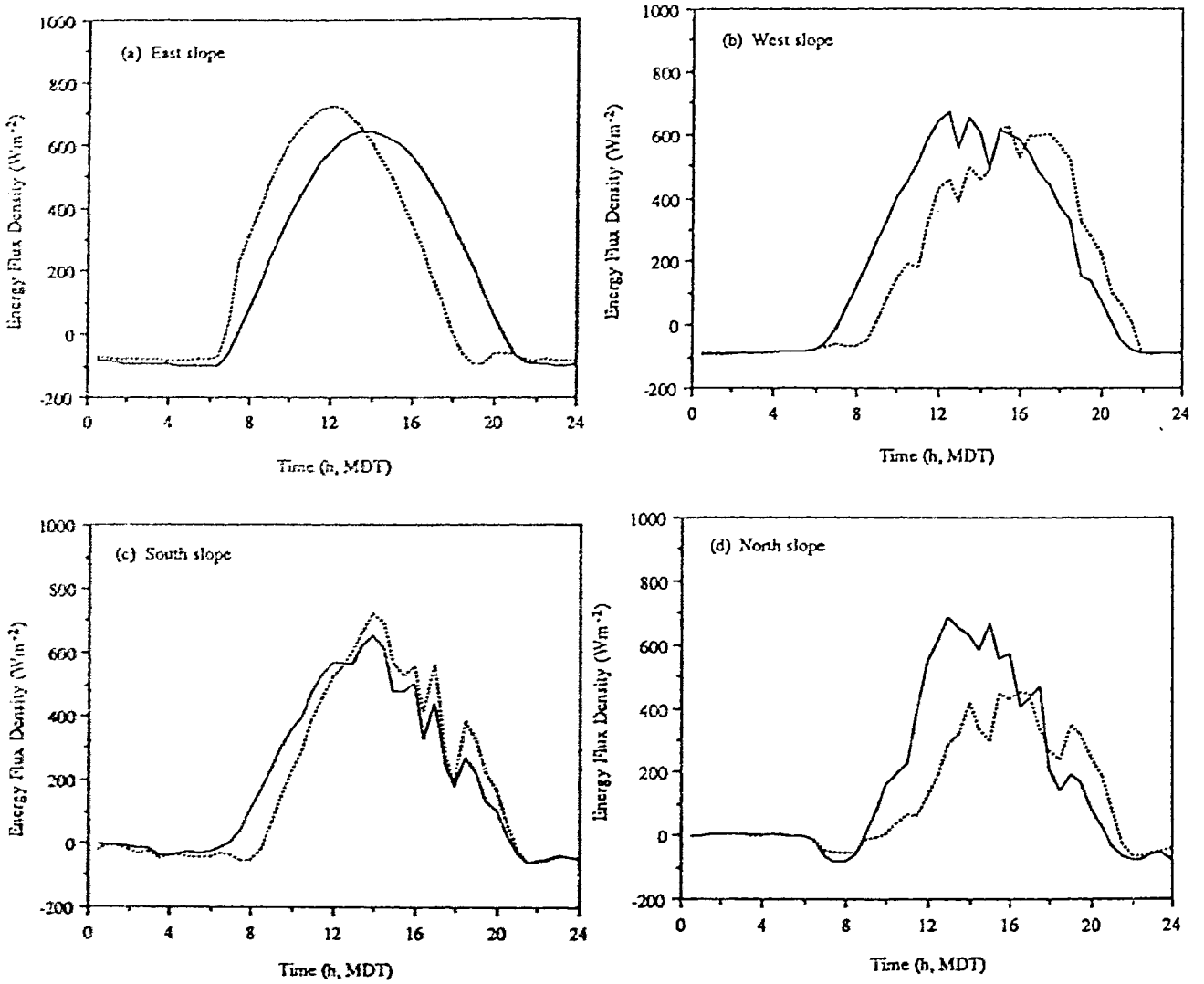

Figure 4.7a Diurnal trends of net radiation on selected clear days. The solid lines are for horizontal site and the dotted lines for sloping sites. (a) July 21; (b) July 8; (c) July 12 and (d) June 25.

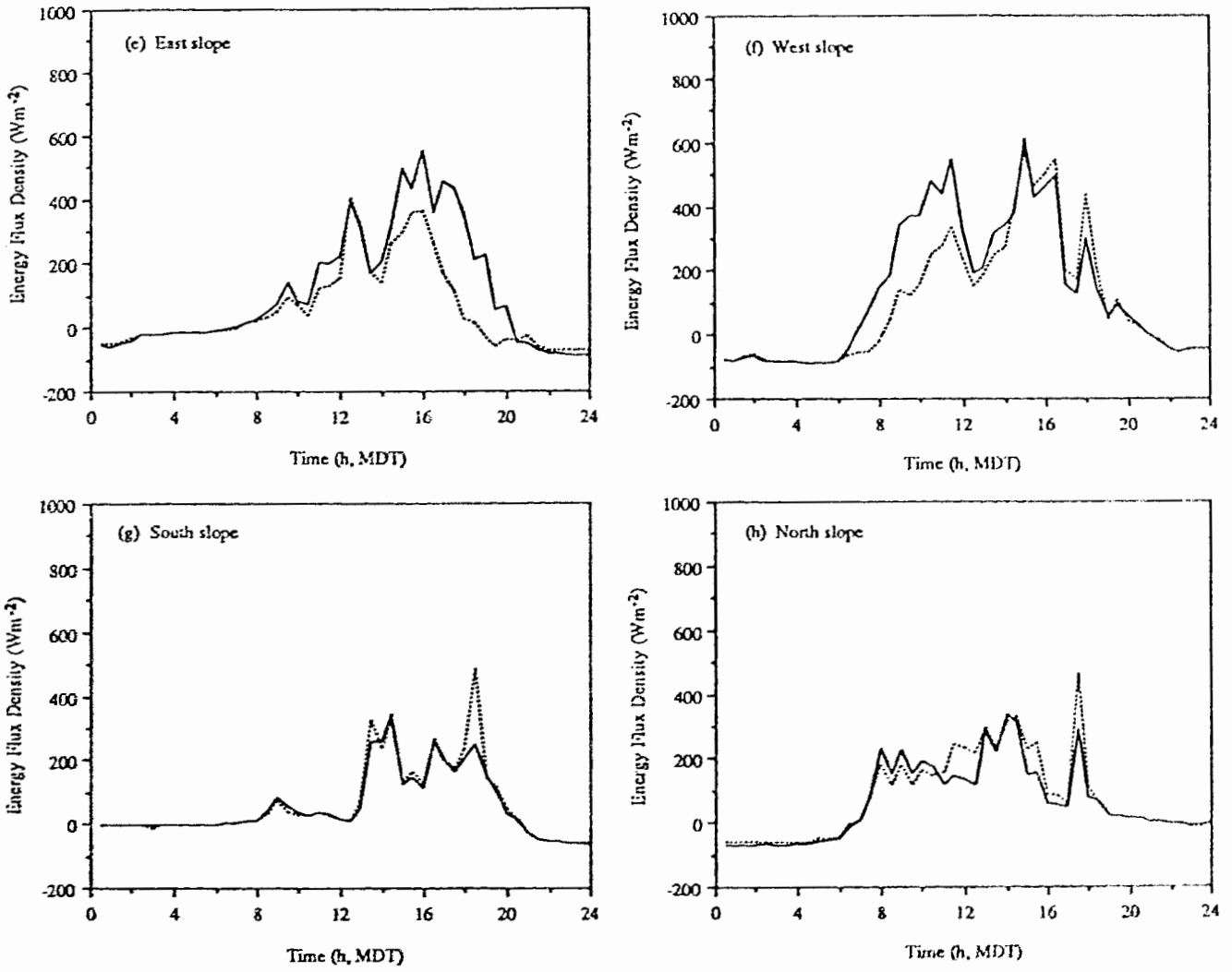

Figure 4.7b Diurnal trends of net radiation on selected cloudy days. The solid lines are for horizontal site and the dotted lines for sloping sites. (e) July 17; (f) July 1; (g) July 10 and (h) June 24.

Table 4.2 The Relationships between Hourly Net Radiation and Hourly Global Solar Radiation

Site	Equation (W m^{-2})	n	r^2	SE (W m^{-2})
East slope	$Q^* = 0.757\ Ks\downarrow - 56.4$	100	0.988	29.8
West slope	$Q^* = 0.797\ Ks\downarrow - 74.8$	136	0.989	23.6
South slope	$Q^* = 0.741\ Ks\downarrow - 25.5$	104	0.981	25.1
North slope	$Q^* = 0.710\ Ks\downarrow - 36.3$	155	0.973	23.3
All slope	$Q^* = 0.706\ Ks\downarrow - 56.3$	578	0.985	29.0
Horizontal	$Q^* = 0.732\ K\downarrow - 48.1$	450	0.978	24.3

significantly on clear days, and this difference diminished on cloudy days or cloudy periods.

Surrounding terrain shading and slope self-shading delayed the sunrise and advanced the sunset. This obviously influences the amount of direct beam solar radiation receiving by the horizontal surface and the sloping surfaces. The influence of surrounding terrain shading is stronger when the solar beam incident angle is small, such as an east sloping surface in the morning. Slope self-shading exhibits the effect of the slope itself on the radiation budget. It influences not only the diurnal course of solar radiation budget components, but also the daily totals on sloping surfaces.

The diurnal trend of albedo is a function of the incident angle of the direct solar radiation and it is symmetrical about the maximum solar beam incident angle. The data reveal the specular reflection characteristics. The snow-covered ground exhibits stronger specular reflection than the snow free surface.

The diurnal trend of incoming longwave radiation is conservative. The incoming longwave radiation on sloping surfaces and the horizontal surface shows no significant differences because the sky view factors are large. The outgoing longwave radiation depends on the surface temperature and surface emissivity. Consequently the outgoing longwave radiation tracked global solar radiation which determines the surface temperature.

Net radiation is dominated by global solar radiation. A strong linear relationship between net radiation and global solar radiation exists for both the horizontal surface and the sloping surfaces.

Chapter 5

ESTIMATING DIRECT AND DIFFUSE SOLAR RADIATION FROM GLOBAL SOLAR RADIATION

5.1 Introduction

In the absence of solar radiation measurements on slopes, solar radiation may be estimated by one of the several methods which usually require values of direct and diffuse components of global solar radiation on a horizontal surface. Whereas global solar radiation on a horizontal surface is measured at some recording stations, measurements of direct radiation or diffuse radiation are rare.

Models have been developed for computing the diffuse or direct radiation components of global solar radiation. When detailed meteorological observations are available, the models developed by Rao et al. (1984), Sherry and Justus (1984), Davies and McKay (1982) and Carroll (1985) make it possible to estimate the diffuse and direct components. Meteorological parameters frequently used as predictors include the type, amount and distribution of clouds or other observations, such as fractional sunshine, atmospheric turbidity and moisture content. Such models usually require complex calculation methods.

Another simpler approach is to correlate the diffuse or direct solar radiation with information based on global solar radiation. The diffuse fraction of global solar radiation is usually expressed as a function of atmospheric transmissivity (t)

$$D_h / K\downarrow = f(t) \qquad (5.1)$$

where D_h is hourly average or daily total diffuse solar radiation on horizontal surface, $K\downarrow$ is global solar radiation and the hourly or daily period atmospheric transmissivity t is defined as

$$t = K\downarrow / K_0 \qquad (5.2)$$

where K_0 denotes the corresponding hourly or daily extraterrestrial solar radiation. Correlation equations for estimating the diffuse and direct components of hourly global

solar radiation have been developed by numerous authors. The correlations developed by Erbs et al. (1982), Skartveit and Olseth (1987), Maxwell (1987), Orgill and Hollands (1977), Iqbal (1980) and Jeter and Balaras (1990) all relate the hourly diffuse fraction (D/K↓) to hourly atmospheric transmissivity (t). The correlation between daily diffuse fraction and transmissivity are presented by Liu and Jordan (1960), Orgill and Hollands (1977), Erbs et al. (1982), Rao et al.(1984) and Kierkus and Colborne (1989). It should be noted that all the data sets used in developing the above correlations are measured at low altitudes except Erbs et al.'s data set which contains a site at 1620 m a.s.l. This chapter will aim at testing some selected hourly and daily models with the data set obtained at an alpine site. Models for this alpine environment will be suggested.

5.2 Models

(1) Hourly Model

For the hourly diffuse fraction, three widely used models are selected for evaluation. The selection of the models is based on a literature review. They were formulated by Erbs, Klein and Duffie (1982), Orgill and Hollands (1977) and Maxwell (1987), which will be referred to as the E-K-D, O-H and M Models from here on. The E-K-D model was selected because it had been found to be the most accurate of such models by the International Energy Agency (IEA) after a comprehensive evaluation against data sets from North America, Europe and Australia (Davies et al., 1988). This model is usually called the standard correlation which is similar in essence to the O-H model. The M model is termed as a quasi-physical model since it combines a physical clear sky model with empirical fits for other conditions. The M model is originally developed to calculate the hourly direct beam component and the E-K-D and O-H models are for diffuse components. Inputs to all models consist of global solar radiation K↓ and solar zenith angle Z. Zenith angle is not an active variable in the E-K-D and O-H models, but it is used to the calculation of

atmospheric transmissivity t . In the M model, Z is used to calculate the air mass (m) since m can be approximated from (Kasten, 1966)

$$m = 1 / [\cos Z + 0.15 (93.885 - Z)^{-1.253}]. \quad (5.3)$$

The three hourly models are summarized as following:

E-K-D model

if $t \leq 0.22$ $\quad D_h / K\downarrow = 1 - 0.09\ t$ (5.4a)

if $0.22 < t \leq 0.80$ $\quad D_h / K\downarrow = 0.9511 - 0.1604\ t + 4.388\ t^2 - 16.638\ t^3 + 12.336\ t^4$ (5.4b)

if $t > 0.80$ $\quad D_h / K\downarrow = 0.165$ (5.4c)

O-H model

if $t < 0.35$ $\quad D_h / K\downarrow = 1 - 0.249\ t$ (5.5a)

if $0.35 \leq t \leq 0.75$ $\quad D_h / K\downarrow = 1.557 - 1.84\ t$ (5.5b)

if $t > 0.75$ $\quad D_h / K\downarrow = 0.177$ (5.5c)

M model

$$D_h / K\downarrow = 1 - \{K_{nc} - [B_1 + B_2 \exp (B_3\, m)]\}\ I_0 / K\downarrow \quad (5.6)$$

where I_0 is the solar constant taken as 1370 Wm^{-2} (IEA,1978)

and $$K_{nc} = 0.866 - 0.122\ m + 0.0121\ m^2 - 0.000653\ m^3 + 0.000014\ m^4 \quad (5.6a)$$

and B_1, B_2 and B_3 are functions of the transmissivity given by:

if $t \leq 0.6$

$$B_1 = 0.512 - 1.560\ t + 2.286\ t^2 - 2.222\ t^3$$
$$B_2 = 0.370 + 0.962\ t \quad (5.6b)$$
$$B_3 = -0.280 + 0.932\ t - 2.048\ t^2$$

if $t > 0.6$

$$B_1 = -5.743 + 21.77\ t - 27.49\ t^2 + 11.56\ t^3$$
$$B_2 = 41.40 - 118.5\ t + 66.05\ t^2 + 31.90\ t^3 \quad (5.6c)$$
$$B_3 = -47.01 + 184.2\ t - 222.0\ t^2 + 73.81\ t^3$$

(2) Daily Model

Three daily models were selected for evaluation. They were developed by Erbs et al. (1982) (E-K-D1 model), Kierkus and Colborne (1989) (K-C model) and Bristow et al. (1985) (B-C-S model). K-C model is essentially similar to E-K-D1 model, but the data base used to develop it consists of eight Canadian sites. B-C-S model is a continuous equation for daily diffuse radiation transmissivity values (defined as D_h / K_0) which incorporates a single physically based coefficient. These models are summarized as follows:

E-K-D1 model

if $t < 0.722$ $\quad D_h / K\downarrow = 1.0 + 0.2832\ t - 2.5557\ t^2 + 0.8448\ t^3$ (5.7a)

if $t \geq 0.722$ $\quad D_h / K\downarrow = 0.175$ (5.7b)

K-C model

if $t \leq 0.11$ $\quad D_h / K\downarrow = 0.98$ (5.8a)

if $0.11 < t < 0.84$ $\quad D_h / K\downarrow = 0.944 + 0.672\ t - 3.22\ t^2 - 0.618\ t^3 + 2.568\ t^4$ (5.8b)

if $t \geq 0.84$ $\quad D_h / K\downarrow = 0.15$ (5.8c)

B-C-S model

An equation of the form

$$D_h / K_0 = t\ [1 - \exp (X - XY / t)] \quad (5.9)$$

is used to describe the relationship between daily diffuse radiation transmissivity D_h/K_0 and atmospheric transmissivity t. Where X and Y are empirical coefficients and they are related. From the original model

$$X = 0.6 / (Y - 0.4) \quad (5.9a)$$

where Y is the maximum clear-sky transmissivity determined from the available data (in this experiment, it is 0.786).

5.3 Observational Procedure

The data set was obtained during a summer experiment in 1989 on Plateau Mountain (2475 m a.s.l.), southwestern Alberta, Canada. The experiment was described in detail in Chapter 3. This data set includes 28 days of half-hourly global and diffuse solar radiation. These data are combined to give the hourly averages and daily totals. The data set is considered to be of high quality.

Following the suggestions of Willmott (1982), two statistical quantities, mean bias error (MBE) and root mean square error (RMSE) between the predicted and measured diffuse radiation are used to evaluate the model performance. MBE and RMSE values are calculated using the following equations

$$MBE = (1/n)\sum_{i=1}^{n}(P_i - O_i) \tag{5.10}$$

$$RMSE = \{(1/n)\sum_{i=1}^{n}(P_i - O_i)^2\}^{0.5} \tag{5.11}$$

where P_i is the predicted or calculated value and O_i is the observed or measured value. MBEs and RMSEs are usually given both in Wm^{-2} and as percentages of the mean diffuse solar radiation. To determine MBE and RMSE as percentage values, the quantities computed using (5.10) and (5.11) are divided by the average observed values.

5.4 Results and Discussion

(1) Hourly Model

Each model's overall MBEs and RMSEs, sorted by transmissivity, are presented in Table 5.1. Table 5.1 also reports the mean diffuse radiation in each transmissivity range. The large MBEs suggest that none of these models can be used in alpine environments without modification. The next analysis, however, is based on the relative performances

Table 5.1 Overall Performance of Selected Hourly Models as a Function of Atmospheric Conditions

t Range		0 - 0.3	0.3 - 0.7	over 0.7	all range
Mean D_h		128	170	101	132
E-K-D model	MBE	2	41	27	27
	RMSE	8	75	67	63
O-H model	MBE	-2	41	34	28
	RMSE	8	75	73	64
M model	MBE	7	36	30	29
	RMSE	14	72	70	63

Note: Units of MBE and RMSE are Wm^{-2}.

between the models. Overall, the E-K-D model performs as well as Maxwell model based on RMSE. O-H model produces a slightly larger RMSE than the other two.

Close analysis of the MBEs and RMSEs in Table 5.1 reveals the different behavior for each model. In the 0.0 - 0.3 transmissivity range, the E-K-D model performs as well as the O-H model in RMSE, but the E-K-D model tends to overestimate and the O-H model tends to underestimate by 2 Wm^{-2}. The M model obviously overestimates the diffuse fraction. It seems that the M model can not handle cloudy conditions properly (see Figure 5.1 and Table 5.1).

For intermediate sky conditions ($0.30 < t < 0.70$), all three models have pronounced tendencies to overestimate, although the M model's tendency is smaller (36 Wm^{-2}). The M model performs relatively better in RMSE (36 Wm^{-2}). The other two behave virtually the same. Within this t range, the result revealed from the present analysis for the M model is generally the same as that concluded by Perez et al. (1990). But the result for the E-K-D model is contrary to Perez et al.'s conclusion. Instead of underestimating, the E-K-D model tends to systematically overestimate by an average of 41 Wm^{-2} or 24% of the diffuse radiation.

For clear sky conditions ($t \geq 0.7$), all the three models again systematically overestimate the diffuse radiation. The E-K-D model produced the smallest MBE and RMSE, followed by the M model and then the O-H model. In their recent work about the evaluation of models that predict hourly direct solar radiation from hourly global solar radiation, Perez et al. (1990) concluded that the M model has an advantage for clear sky conditions. This current analysis, however, does not support their conclusion.

From the above analysis, it is clear that except for one case, all three models overestimate the diffuse radiation, especially for intermediate and clear sky conditions. This is understandable when considering the high elevation and extremely transparent clear sky conditions. A similar phenomenon has also been noted by Olyphant (1984) and Isard

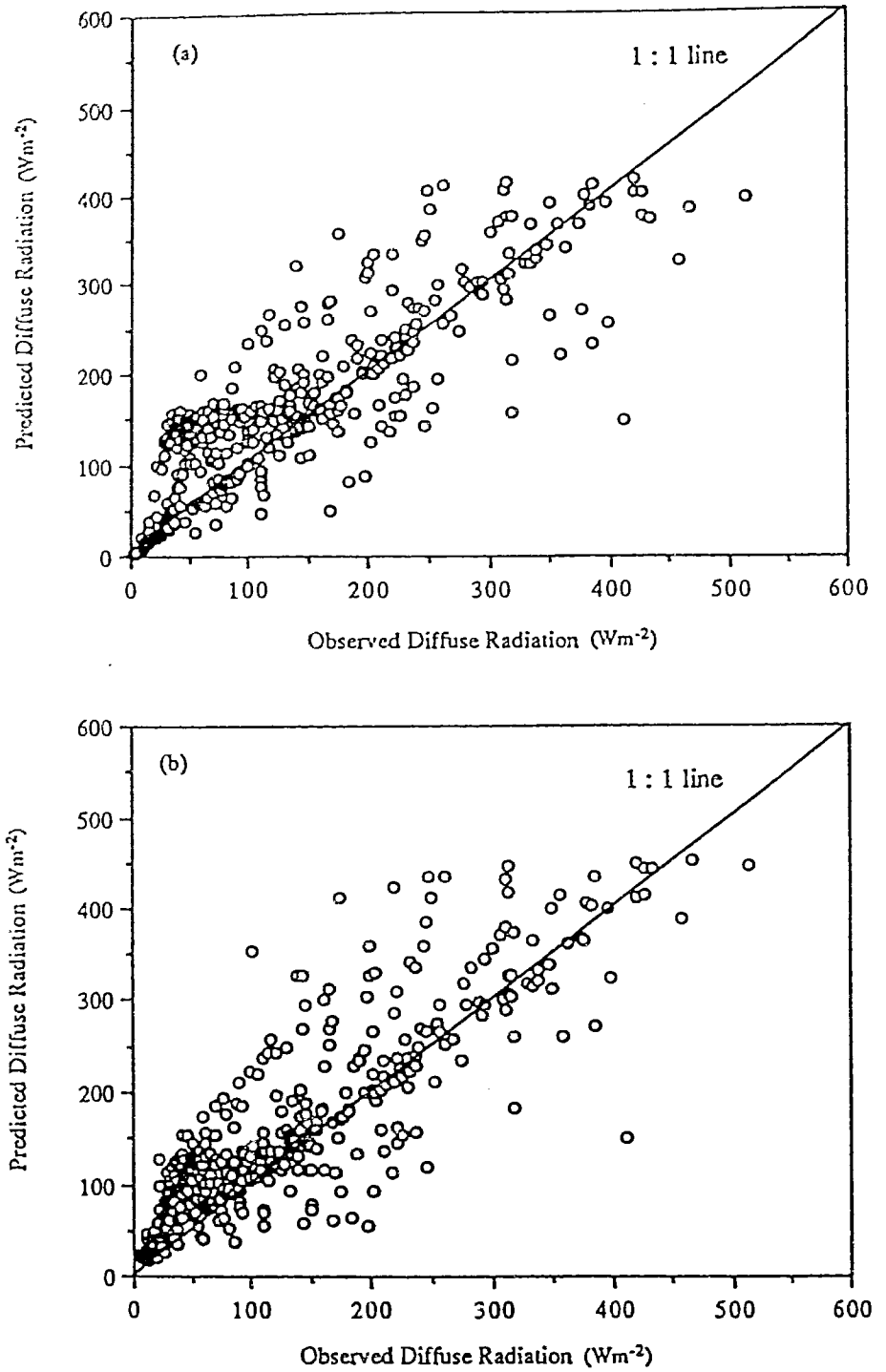

Figure 5.1 Observed hourly average diffuse radiation versus the predicted values with (a) the E-K-D model and (b) the Maxwell model.

(1986). In Olyphant and Isard's work, they used $D_h / K\downarrow = 0.12$ at $t > 0.8$, whereas Erbs et al. data gave $D_h / K\downarrow = 0.165$. Based on the Plateau Mountain data set, a revised E-K-D model is proposed

$$\text{if } t \leq 0.22 \qquad D_h / K\downarrow = 1.015 - 0.208\, t \tag{5.12a}$$

$$\text{if } 0.22 < t \leq 0.80 \qquad D_h / K\downarrow = 0.166 + 9.570\, t - 36.71 t^2 + 48.50\, t^3 - 22.03\, t^4 \tag{5.12b}$$

$$\text{if } t > 0.80 \qquad D_h / K\downarrow = 0.12. \tag{5.12c}$$

This model has a MBE of 1 Wm^{-2} and a RMSE of 60 Wm^{-2}. Although this model has not included site altitude as a parameter, its influence is actually included in the calculation of the atmospheric transmissivity. Therefore, it is suggested that this model has application to other similar alpine environments.

(2) Daily Model

The MBEs and RMSEs in different atmospheric transmissivity ranges are presented in Table 5.2 for the three selected models which predict the daily diffuse radiation. Although the data set is not large enough to provide a more reliable evaluation, the results in Table 5.2 at least give a preliminary test of the daily model with alpine radiation data. The overall performances in MBE and RMSE are very close for the three models, the RMSEs are 2.2, 2.3 and 2.4 $MJm^{-2}\ d^{-1}$ for the K-C, the B-C-S and the E-K-D1 models, respectively. Examining the MBEs, one notes that the E-K-D1 and the K-C model have tendencies to overestimate the diffuse components, especially for intermediate and high clearness indices. The reason for the overestimation may be also explained by the high altitude and extremely transparent atmosphere.

It seems that the E-K-D1 model can handle low and high t, but it failed in the intermediate t range, with RMSE as high as 3.1MJ $m^{-2} d^{-1}$ or 35% of the mean value. The performance of the K-C model has a similar trend to that of the E-K-D1 model and the handling of the intermediate t is better. The B-C-S model overestimates diffuse fraction at

Table 5.2 Overall Performance of Selected Daily Models as a Function of Atmospheric Conditions

t Range		0 - 0.3	0.3 - 0.7	over 0.7	all range
Mean D_h		8.3	8.7	4.1	7.5
E-K-D1 Model	MBE	0.7	2.6	0.2	1.8
	RMSE	1.1	3.1	0.7	2.4
K-C Model	MBE	0.6	1.9	1.9	1.7
	RMSE	0.9	2.4	2.0	2.2
B-C-S Model	MBE	1.0	2.0	-1.6	0.9
	RMSE	1.4	2.6	1.7	2.3

Note: Units of MBE and RMSE are $MJm^{-1}d^{-1}$.

$t < 0.70$, and underestimate at $t > 0.70$. This suggests that equation (5.9a) is not proper here. From the alpine data set, this relation should be adjusted to:

$$X = 0.42 / (Y - 0.4). \tag{5.13}$$

Then, the B-C-S model will be

$$D_h / K_0 = t \{ 1 - \exp[0.42 (1 - Y / t) / (Y - 0.4)] \} \tag{5.14}$$

which has a MBE of 0.5 $MJm^{-2} d^{-1}$ and a RMSE of 2.0 $MJm^{-2} d^{-1}$.

5.5 Conclusions

In order to calculate the solar radiation incident on slopes from its measurements on a horizontal surface, separating the direct and diffuse components of global solar radiation is required. In this chapter, three hourly models (E-K-D, O-H and the M models) and three daily models (E-K-D1, K-C and B-C-S models) are selected for evaluation using the measurements in alpine area.

The results of this evaluation of six models are consistent with the findings of Olyphant (1984) and Isard (1986). However, the results do not support all the conclusions of Perez et al. (1990). Nearly all the models systematically overestimate diffuse fraction. None can be used in alpine environments without modification. The reasons suggested are the high altitude of the site and the more transparent atmosphere.

For hourly models, the overall performances of the E-K-D and the M models are close in RMSE, but the M model produces a larger MBE. Close analysis shows both the E-K-D and the O-H models can work properly under cloudy conditions. The Maxwell model handles the intermediate sky conditions better. A modified E-K-D model is presented as equation 5.12. For daily models, all three produce similar RMSE. Close examination shows that the E-K-D1 model can handle low and high clearness indices more properly. The B-C-S model could be better with the adjusted relation (equation 5.14).

All of the above analyses are preliminary and longer term measurements in alpine environments are still needed to further confirm these findings.

Chapter 6

EVALUATION OF MODELS FOR PREDICTING SOLAR RADIATION FOR ALPINE TUNDRA SLOPING SURFACES

6.1 Introduction

The estimation of solar radiation for a sloping surface requires a geometrically based transformation of direct solar radiation and an integration of the diffuse radiance (both sky and surface-reflected) over the field of view of the sloping surface. Over the past three decades, a number of models have been developed. Some are for climatological and hydrological studies and most are directed to engineering purposes (Rowe and Willmott, 1984). No matter what the original purposes of the models are, their underlying theory is the same and can be used for a host of purposes. Hay and McKay (1985) provided an extensive review of the sloping surface solar radiation models developed by Kondratyev (1977), Bugler (1977), Loudon (1967), Hay (1979), Klucher (1979), Puri et al. (1980), Perez et al. (1983). In the International Energy Agency's Task IX of the Solar Heating and Cooling Programme, Hay and McKay (1987) tested 21 solar radiation models by comparing a data base from 27 different sites around the world.

The object of this chapter is to estimate the magnitude of errors resulting from the use of one isotropic and the three most successful anisotropic solar radiation models. This will be accomplished by comparing radiation estimates based on measurements on an unobstructed horizontal site with solar radiation measurements on natural sloping surfaces on Plateau Mountain, southwestern Alberta, Canada. Further, the effects of using the equations in Chapter 5 instead of directly measured diffuse radiation will also be assessed.

6.2 Theoretical Background

The calculation of solar radiation from a horizontal surface to a sloping surface involves separate treatment of the three components of incident solar radiation: direct solar radiation

(S_s), diffuse radiation from the sky (D_s) and the reflected solar radiation from surrounding terrain within the field of view of the slope (K_t). The global solar radiation received on an unobstructed slope $K_s\downarrow$ can be written as

$$K_s\downarrow = S_s + D_s + K_t . \tag{6.1}$$

When the slope is shaded by surrounding terrain, Equation 6.1 should be rewritten as

$$K_s\downarrow = \beta S_s + \gamma_1 D_s + \gamma_2 K_t \tag{6.2}$$

where β is a binary coefficient (when the sun is shaded by surrounding terrain, $\beta = 0$, otherwise $\beta = 1$), and γ_1 and γ_2 are respectively local terrain shading index and local terrain enhancement index, which can be determined by the local horizon. The derivations of γ_1 and γ_2 are summarized in Appendix III.

(1) Direct Solar Radiation

For short time intervals (an hour or less), the task of determining direct solar radiation for a sloping surface is simply one of geometry and the literature contains essentially one fundamental approach. According to Kondratyev (1977) and Hay and Davies (1980), the direct beam radiation for an arbitrarily oriented sloping surface S_s can be expressed by the direct solar radiation flux to a surface normal to the solar rays S_m by using

$$S_s = S_m \cos i \tag{6.3}$$

where i is the incident angle of solar rays on a given surface. Here S_m can be expressed by direct solar radiation on horizontal surface S_h by

$$S_m = S_h / \sin h_o \tag{6.4}$$

where h_o is solar elevation angle. Substituting equation 6.4 into equation 6.3 yields

$$S_s = S_h \cos i / \sin h_o . \tag{6.5}$$

The cosine of the incident angle of solar rays is determined by

$$\cos i = \cos \alpha \sin h_o + \sin \alpha \cos h_o \cos (\psi_o - \psi_\alpha) \tag{6.6}$$

where α is the inclination angle of a sloping surface, ψ_o and ψ_α the solar azimuth and slope orientation (counted from the plane of the meridian and considered positive when counted

clockwise). The solar elevation angle and azimuth can be calculated by the following astronomical formulas

$$\sin h_o = \sin \phi \sin \delta + \cos \phi \cos \delta \cos \omega \tag{6.7}$$

$$\cos \psi_o = \frac{\sin \phi \sin h_o - \sin \delta}{\cos \phi \cos h_o} \tag{6.8}$$

$$\sin \psi_o = \frac{\cos \delta \sin \omega}{\cos h_o} \tag{6.9}$$

where ϕ is the latitude, δ the sun's declination and ω the hour angle of the sun at a given moment counted from the moment of apparent noon (ω is considered positive when counted clockwise).

(2) Diffuse Radiation from Sky

Determination of the diffuse solar radiation for a sloping surface necessitates that assumptions be made regarding the distribution of diffuse solar radiance both over the sky hemisphere and over the ground surface within the field of view of the slope (Hay and Davies, 1980). For the sky diffuse radiation, isotropic and anisotropic models have been proposed based on the different assumptions of sky radiance distribution over the sky hemisphere (Kondratyev, 1977; Hay and Davies, 1980; Klucher, 1979; and Perez et al., 1987). The main difference between the models in Section 6.3 will lie in the treatment of this component. These isotropic or anisotropic models will be presented here.

Isotropic model

The simplest distribution is that of a uniform irradiance over the sky hemisphere, the assumption of isotropy, and yielding the isotropic model. Kondratyev (1969, 1977) and

several others have provided the mathematical derivation of the isotropic model for calculating the diffuse radiation of a sloping surface.

In deriving the model, it is assumed that the diffuse radiation in the sky hemisphere is isotropic, and the surface of the slope and the horizontal surface in front of it are absolutely black. Then, it is possible to neglect the radiation reflected from the horizontal surface to the slope and the effects of multiple reflection. The diffuse radiation to an unobstructed sloping surface can then be derived as

$$D_s = 0.5\,\pi\,I\,(1 + \cos\alpha) \qquad (6.10a)$$

$$= 0.5\,D_h\,(1 + \cos\alpha) \qquad (6.10b)$$

where I is the intensity of diffuse radiation and $D_h = \pi\,I$ is the diffuse radiation on an unobstructed horizontal surface. Equation 6.10 is the isotropic model for diffuse solar radiation on an unobstructed sloping surface. When there exists horizon obstruction, the portion of D_s from the sky will be reduced. The reduction can be handled successfully by multiplying a surrounding terrain shading index. The derivation of terrain shading index is presented in Appendix II. Table 6.3 lists the shading index for the four sloping surfaces.

Klucher's anisotropic model

Klucher's anisotropic model (Klucher, 1979) is based on the model proposed by Temps and Coulson (1977). He extended the Temps-Coulson cloudless sky model to all-sky conditions. In the Temps-Coulson model, two correction factors are combined with the isotropic model to account for each of the two regions of anisotropy in the diffuse radiation field. They determined that a factor, $1+\sin^3(\alpha/2)$, accounts for the increase in sky light near the horizon during cloudless days. Similarly, the sky brightening observed near the sun could be approximated by the factor $1+\cos^2 i\,\sin^3 Z$, where i and Z are the incident angle of the sun's ray to sloping surface and solar zenith angle respectively. Then the Temps-Coulson anisotropic clear sky model has the form of

$$D_s = 0.5\,D_h\,(1 + \cos\alpha)\,(1 + \sin^3(\alpha/2))\,(1 + \cos^2 i\,\sin^3 Z). \qquad (6.11)$$

Klucher's model introduced an anisotropic function

$$F = 1 - (D_h / K\downarrow) \qquad (6.12)$$

into Temps-Coulson anisotropic cloudless sky model to account for all-sky conditions (i.e. cloudless, partly cloudy and overcast). Then Klucher's all-sky anisotropic model takes the form

$$D_s = 0.5\, D_h (1 + \cos \alpha) [1 + F \sin^3 (\alpha / 2)] [1 + F \cos^2 i \sin^3 Z]. \qquad (6.13)$$

Equation 6.13 shows that under cloudless conditions, the ratio of diffuse to total solar radiation is very small, i.e. $F \approx 1$, then equation 6.13 approximates Temps-Coulson cloudless sky model (equation 6.11).

Hay's anisotropic model

Hay (1979) and Hay and Davies (1980) have presented another anisotropic slope diffuse radiation model which is similar to Klucher's anisotropic model. The derivation was based on the following premises: *a*) when no direct beam solar radiation is observed in an hour (direct transmission is zero), the sky is essentially overcast and the isotropic model is approximate for the hour; *b*) in the absence of an atmosphere, all the radiation is direct beam (i.e. the direct transmission is 1.0) and in this limiting case all the radiation can be treated according to equation 6.5; *c*) for the case when the direct transmission is between these two extremes, the assumption is made that hourly integrated direct radiation will define the portion of diffuse radiation to be treated as isotropic and the portion to be treated as circumsolar. Therefore, the direct transmission is used to define an anisotropic index k as

$$k = S_h / K_0 \qquad (6.14)$$

where K_0 is extraterrestrial radiation on horizontal surface.

With equation 6.14, the diffuse radiation treated as isotropic (D_s') is

$$D_s' = 0.5\, D_h (1 + \cos \alpha) (1 - k) \qquad (6.15)$$

and the portion treated as circumsolar (D_s'') is evaluated as

$$D_s'' = D_h (k \cos i / \cos Z). \qquad (6.16)$$

The form of equation 6.16 is similar to that of equation 6.5 except that equation 6.16 is for circumsolar radiation. Then the diffuse radiation intercepted by the sloping surface is the sum of isotropic portion (6.15) and circumsolar portion (6.16)

$$D_s = D_h [0.5 (1 + \cos a) (1 - k) + k \cos i / \cos Z] . \qquad (6.17)$$

Equation 6.17 is Hay's all-sky condition anisotropic model. It will be noted that when the sky is overcast and no direct solar radiation observed, Hay's anisotropic model will treat all the diffuse radiation as isotropic. This is similar to Klucher's model. Both Klucher's and Hay's anisotropic model are basically the same. The only difference between these models is the assumed distributions for clear sky radiance and the nature of the anisotropic factors ($F=D_h/K\downarrow$ for Klucher and $k=S_h/K_0$ for Hay).

Perez anisotropic model (Perez et al., 1987)

This model describes the diffuse radiation from the sky as the superposition of an isotropic distribution, a circumsolar zone and a luminous horizon band. This is actually an attempt to replicate circumsolar and horizon brightening. The anisotropy may vary depending on meteorological conditions and is related to the following parameters which are used as model inputs, the amount of diffuse radiation on a horizontal plane and the ratio

$$\rho = (S_m + D_h) / D_h . \qquad (6.18)$$

The basic Perez model is expressed as

$$D_s\downarrow = D_h \{ 0.5 (1 + \cos \alpha) (1 - F_1) + F_1 (a/c) + F_2 \sin \alpha \} \qquad (6.19)$$

where a is solid angle corresponding to the circumsolar zone as seen from the slope, c denotes the solid angle corresponding to the circumsolar zone as seen from the horizontal surface. F_1 and F_2 are luminosity coefficients for the circumsolar zone and horizon band, respectively. The determination of a, c, F_1 and F_2 is given by Perez et al. (1987).

(3) Diffuse Radiation from Ground Reflection

The diffuse irradiance distribution over the ground surface has been studied by several authors (Liu and Jordan, 1960; Kondratyev, 1977; Temps and Coulson, 1977; Davies and Hay, 1980). Both isotropic and anisotropic models have been proposed. Hay and McKay (1985) reviewed and tested the various models. They concluded that when the ground is snow-free (summer season), the isotropic model performs better; when the ground is snow-covered, an anisotropic model (Temps and Coulson, 1977) showed a small but persistent advantage. Ineichan et al. (1990) tested several different models and obtained similar conclusions. Since the present data set was obtained in summer season when the natural surface was snow-free, this component in the following models will take an isotropic assumption. Under this assumption, the radiation reflected by the ground and seen by the unobstructed slope is given by

$$K_t = A\, K\downarrow\ 0.5\,(1 - \cos\alpha) \qquad (6.20)$$

where A (0.18) is the average tundra surface albedo during the experiment and α is slope angle.

6.3 Global Solar Radiation Models for a Slope

The solar radiation to an unobstructed sloping surface is the sum of the three components (S_s, D_s and K_t). On the basis discussed in last section, one isotropic and three anisotropic models are proposed for calculating the solar radiation on sloping surfaces. The isotropic or anisotropic global radiation models are named after the treatment of sky diffuse component D_s. In all four models, S_s and K_t are treated by equation 6.5 and equation 6.20 respectively.

(1) Isotropic Model (Model A, Kondratyev, 1977)

Based on the isotropic assumption, this model gives the total solar radiation ($K_s\downarrow$) to an unobstructed sloping surface of relative azimuth (ψ) and slope angle (α) by

$$K_s\downarrow = S_h\,(\cos i / \cos Z) + 0.5\,D_h\,(1 + \cos\alpha) + 0.5\,K\downarrow\,A\,(1 - \cos\alpha) \qquad (6.21)$$

where albedo A = 0.18, the average albedo of the tundra surface on Plateau Mountain during the experiment period.

(2) Hay and Davies's Anisotropic Model (Model B, Hay and Davies, 1980)

For the diffuse solar radiation, Hay and Davies's model combines the increase in diffuse solar radiation from the circumsolar sky with the isotropic approximation for diffuse sky radiation. This model is given by

$$K_s\downarrow = S_h (\cos i / \cos Z) + D_h \{\kappa \cos i / \cos Z + 0.5 (1 - \kappa) (1 + \cos \alpha)\} + 0.5\, K\downarrow A (1 - \cos \alpha) \quad (6.22)$$

with

$$\kappa = S_h / I_0 \cos Z \quad (6.23)$$

where I_0 (=1370 Wm^{-2}) is solar constant (International Energy Agency, 1978).

(3) Klucher's Anisotropic Model (Model C, Klucher, 1979)

Klucher's model is written by

$$K_s\downarrow = S_h (\cos i / \cos Z) + D_h \{ 0.5 (1 + \cos \alpha) (1 + F \sin^3(\alpha/2)) \times (1 + F \cos^2 i \sin^3 Z)\} + 0.5\, K\downarrow A (1 - \cos \alpha). \quad (6.24)$$

with a modulating function

$$F = 1 - (D_h / K\downarrow)^2 \quad (6.25)$$

(4) Perez et al.'s Anisotropic Model (Model D, Perez et al., 1987)

The basic Perez et al.'s model is expressed as

$$K_s\downarrow = S_h (\cos i / \cos Z) + D_h \{ 0.5 (1 + \cos \alpha) (1 - F_1) + F_1 (a/c) + F_2 \sin \alpha\} + 0.5\, K\downarrow A (1 - \cos \alpha) \quad (6.26)$$

where the ratio

$$\rho = (S_n + D_h) / D_h. \quad (6.27)$$

The determination of a, c, F_1 and F_2 are given by Perez et al. (1987). In this study, F_1 and F_2 coefficients evaluated for a circumsolar disk of radius 25° and based on the original data measured at Trappes (USA) and Carpentras (France).

As discussed in Chapter 5, when the direct measurements of diffuse radiation on horizontal surface are unavailable, it is necessary to separate the global solar radiation into its direct and diffuse components. To explore the effects of using a diffuse fraction correlation on the resulting radiation predicted by each of the above model, the correlation developed for Plateau Mountain (see Chapter 5) has been used to predict the diffuse radiation on a horizontal surface (given measured global radiation on horizontal surface).

The correlation is

$$\text{if } t \leq 0.22 \qquad D_h/K\downarrow = 1.015 - 0.208\, t \tag{6.28a}$$

$$\text{if } 0.22 < t \leq 0.80 \qquad D_h/K\downarrow = 0.166 + 9.570\, t - 36.71 t^2 + 48.50\, t^3 - 22.03\, t^4 \tag{6.28b}$$

$$\text{if } t > 0.80 \qquad D_h/K\downarrow = 0.12 \tag{6.28c}$$

where t is atmospheric transmissivity. It is defined as

$$t = K\downarrow / K_0 \tag{6.29}$$

where K_0 is the extraterrestrial radiation. Using diffuse sky radiation calculated from equation 6.28 instead of the direct measurements, the above models were tested against the global solar radiation measurements.

6.4 Observational Procedure

The radiation measurements were obtained between June 20 and July 24, 1989 on the Plateau Mountain (50°15' N, 114°31' W, 2300 - 2475 m a.s.l.), southwestern Alberta, Canada. Details on the sites are presented in Chapter 1. An Eppley PSP pyranometer was used to measure the global solar radiation on the unobstructed horizontal summit area. Another Eppley PSP pyranometer mounted with a shadow band was used to measure the diffuse radiation on the horizontal surface. A third Eppley PSP pyranometer mounted on a

tripod was used to measure global solar radiation on the four slopes oriented the four major directions. Simultaneous measurements were taken at 10 second intervals and the data loggers provided half-hourly averages. These half-hourly averages were combined to give hourly average radiation values.

At the horizontal site, both global radiation and diffuse radiation are available. The direct radiation on horizontal surface can be calculated. Then it is transposed to slope site as "observed" direct radiation on slope. Therefore, the "observed" diffuse radiation on slopes is obtained by subtracting the "observed" direct radiation from the measured global solar radiation on the sloping site.

It should be noted that the hourly data when global radiation was below 5 Wm^{-2} are rejected. All computations involving the solar zenith angle are performed every 2 minutes (or 0.5 degree hour angle) and then averaged over the whole hour. Such computations apply to hourly input data when evaluating the slope direct and diffuse radiation from global and diffuse radiation on the horizontal surface.

Mean bias error (MBE) and root mean square error (RMSE) as described by Willmott (1982) are used for performance assessment. For this experiment, MBE indicates the average hourly difference between the measured and calculated radiation values. It gives information on the long term bias that is the systematic error between model predictions and measurements. RMSE is a general indicator including biases and fluctuations and is usually considered as a way to evaluate errors.

6.5 Results And Discussion

Figure 6.1 shows the plots of hourly measured versus calculated values of total solar radiation upon the Plateau Mountain slopes by using the four models (Model A: isotropic model; Model B: Hay and Davies' anisotropic model; Model C: Klucher's anisotropic model; and Model D: Perez et al's anisotropic model). Each dot on the figure corresponds to one hour. The MBE and RMSE indicate the systematic and non-systematic variation of

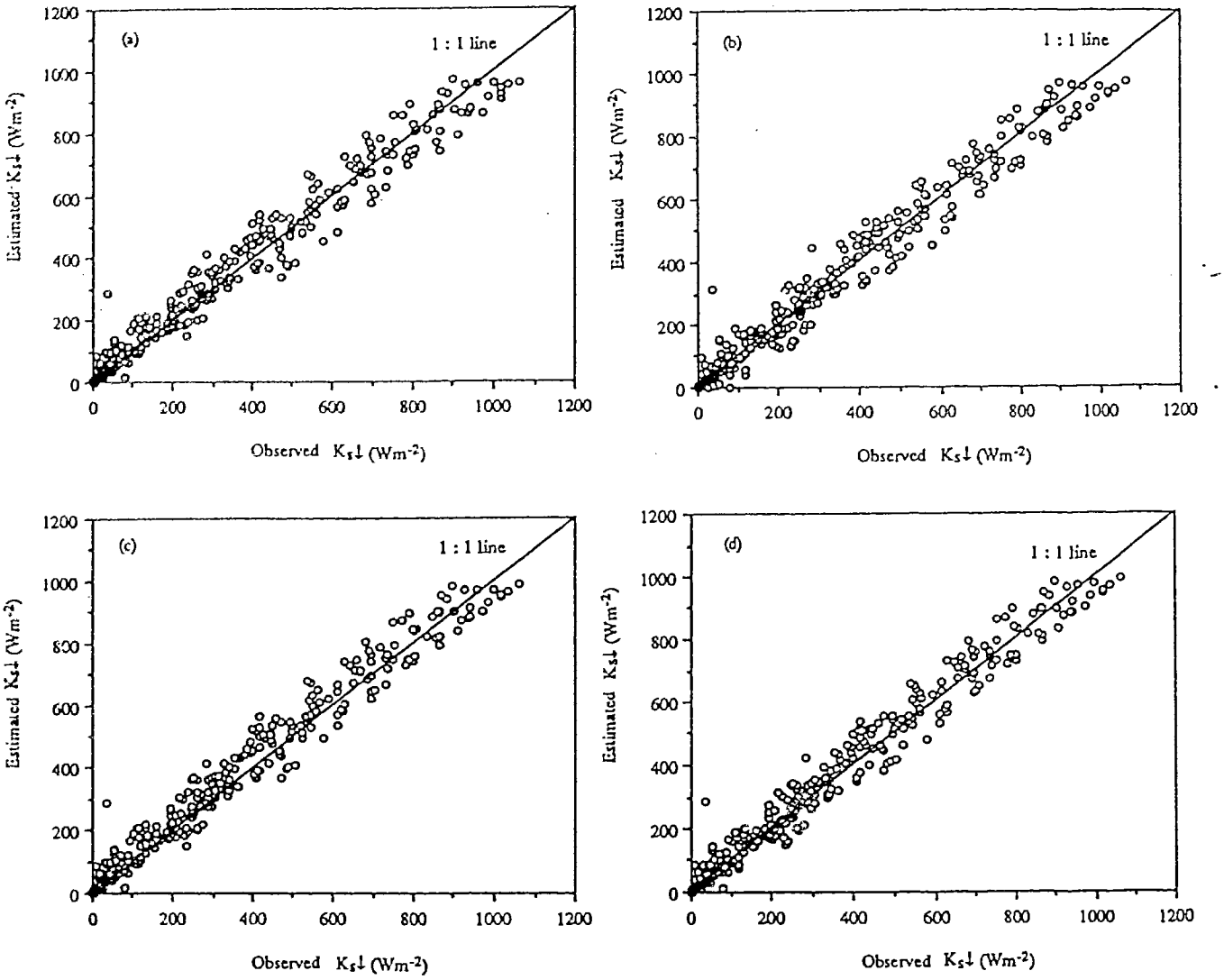

Figure 6.1 Observed hourly solar radiation versus the predicted values with (a) isotropic model, (b) Hay and Davies' anisotropic model, (c) Klucher's anisotropic model and (d) Perez's anisotropic model.

predictions from measurements. For example, the average estimate of total solar radiation for slope using Perez et al.'s model systematically exceeds the measured global flux by 2% (6 Wm^{-2}) with an error of 15% (45 Wm^{-2}) for individual observations. Using the correlation of the hourly diffuse fraction and atmospheric transmissivity increases the non-systematic error (the average increase of RMSE for Model A, Model B, Model C and Model D are 11, 2, 8, 9 Wm^{-2}, respectively). The differences of the isotropic (A) and anisotropic models (B, C and D) in MBE and RMSE are also very small (RMSE for Model A, B, C, D are 40, 47, 42 and 38 Wm^{-2}, respectively).

Table 6.1 gives the performance statistics for models A, B, C, D and Table 6.2 lists the results of the model test using equation 6.28. Since the "observed" slope diffuse is derived as a difference (see Section 6.4), the absolute values of MBE and RMSE in the estimates of the diffuse and global slope radiation are identical. However, the relative errors are substantially reduced when expressed relative to the global as opposed to the diffuse solar radiation. Although the overall performances (indicated by MBE and RMSE) are close for all models, Perez et al.'s model (Model D) shows persistent better performance (RMSE) over the others on all slopes. All models underestimate slope radiation for clear skies. Under clear days, the differences between predicted and measured solar global radiation on slopes are within 10.5% for all four models, although the relative errors to diffuse radiation are high. This may be attributed to the method used to derive the "observed" slope diffuse radiation. Close examination of Table 6.1 and Table 6.2 shows that all models give small MBEs on south and north facing slopes and significant underestimation on east facing slope and overestimation on west facing slope.

In order to investigate the possible influence of local horizon on these results, the terrain shading indexes γ_1 and the terrain enhancement index γ_2 for the four slopes are calculated (Table 6.3). The adjusted slope radiation estimates according to Equation 6.2 are compared with the measurements. Table 6.4 presented the performance statistics. The results show insignificant improvement on MBEs and RMSEs. This is obviously because

Table 6.1 Performance Statistics of Models for Calculating Global Solar Radiation on Sloping Surfaces

		Model A			Model B			Model C			Model D			measured	measured
		absolute	relative (%) of		absolute	relative (%) of		absolute	relative (%) of		absolute	relative (%) of		diffuse	global
		(Wm^{-2})	diffuse	global	(Wm^{-2})	diffuse	global	(Wm^{-2})	diffuse	global	(Wm^{-2})	diffuse	global	(Wm^{-2})	(Wm^{-2})
south	MBE	-0.2	-0.2	-0.1	-6	-4.9	-2.5	7	5.8	2.5	3	2.5	1.2	121	244
	RMSE	30	24.8	12.3	29	24.0	11.9	33	27.3	13.5	27	22.3	11.1		
north	MBE	-1	-0.9	-0.5	-0.3	-0.3	-0.1	5	4.5	2.4	-0.2	-0.2	-0.1	110	208
	RMSE	36	32.7	17.3	34	30.9	16.3	38	34.5	18.3	36	32.7	15.4		
east	MBE	-21	-18.6	-5.5	5	4.4	1.3	-15	-13.3	-3.9	-22	-19.5	-5.7	113	384
	RMSE	43	38.1	11.2	52	46.0	13.5	39	34.5	10.2	38	33.6	9.9		
west	MBE	23	26.1	6.1	21	23.9	5.6	36	40.9	9.6	30	34.1	8.0	88	376
	RMSE	47	53.4	12.5	44	50.0	11.7	53	60.2	14.1	46	52.3	12.2		
all	MBE	3	2.8	1.0	3	2.8	1.0	11	10.4	3.5	6	5.7	1.9	106	314
slopes	RMSE	40	37.7	12.7	47	44.3	15.0	42	39.6	13.4	38	35.8	12.1		
clear	MBE	-8	-13.3	-1.5	-5	-8.3	-0.9	-2	-3.3	-0.4	-3	-5.0	-0.6	100	537
sky	RMSE	56	93.3	10.4	54	90	10.1	54	90.0	10.1	52	86.7	9.7		

Table 6.2 Performance Statistics of Models for Calculating Global Solar Radiation on Sloping Surfaces Using Equation 6.28

		Model A			Model B			Model C			Model D			measured	measured
		absolute	relative (%) of		absolute	relative (%) of		absolute	relative (%) of		absolute	relative (%) of		diffuse	global
		(Wm^{-2})	diffuse	global	(Wm^{-2})	diffuse	global	(Wm^{-2})	diffuse	global	(Wm^{-2})	diffuse	global	(Wm^{-2})	(Wm^{-2})
south	MBE	7	6.25	2.9	1	0.9	0.4	15	13.4	0.1	10	8.9	4.1	112	244
	RMSE	34	30.4	13.9	31	27.7	12.7	37	33.0	15.2	32	28.6	13.1		
north	MBE	2	2.0	1.0	1	-1.0	0.5	7	7.0	3.4	2	2.0	1.0	100	208
	RMSE	37	37.0	18.0	38	38.0	18.3	38	38.0	18.3	38	38.0	18.3		
east	MBE	-31	-23.3	-8.1	-40	-30.1	-10.4	-19	-14.3	-4.9	-25	-18.8	-0.5	133	384
	RMSE	59	44.4	15.4	61	45.9	15.9	45	33.8	11.7	46	34.6	12.0		
west	MBE	34	43.6	9.0	31	39.7	8.2	47	60.3	12.5	40	51.3	10.6	78	376
	RMSE	60	76.9	16.0	56	71.8	14.9	66	84.6	17.6	59	75.6	15.7		
all slopes	MBE	7	6.8	2.2	2	1.9	0.6	17	16.5	5.4	11	10.7	3.5	103	314
	RMSE	51	49.5	16.2	49	47.6	15.6	50	48.5	15.9	47	45.6	15.0		

Table 6.3 Calculated Terrain Shading Indexes and Terrain Enhancement Indexes

slope orientation	γ_1	γ_2
South	0.9911	1.0553
North	0.9886	1.2081
East	0.9837	1.2136
West	0.9292	1.6017

Table 6.4 Performance Statistics of Models for Calculating Global Solar Radiation on Sloping Surfaces (Adjusted for terrain shading and terrain enhancement)

		Model A			Model B			Model C			Model D			measured	measured
		absolute	relative (%) of		absolute	relative (%) of		absolute	relative (%) of		absolute	relative (%) of		diffuse	global
		(Wm^{-2})	diffuse	global	(Wm^{-2})	diffuse	global	(Wm^{-2})	diffuse	global	(Wm^{-2})	diffuse	global	(Wm^{-2})	(Wm^{-2})
south	MBE	-2	-1.7	-0.8	-4	-3.3	-1.6	5	4.1	2.0	1	0.8	0.4	121	244
	RMSE	3 0	24.8	12.3	29	24.0	11.9	31	25.6	12.7	27	22.3	11.1		
north	MBE	-2	-1.8	-1.0	-2	-1.8	-1.0	4	3.6	1.9	-1	-0.9	-0.5	110	208
	RMSE	35	31.8	16.8	34	30.9	16.3	37	33.6	17.8	36	332.7	15.4		
east	MBE	-24	-21.2	-6.3	-40	-35.4	-10.4	-19	-16.8	4.9	-25	-22.1	-6.5	113	384
	RMSE	42	37.2	11.2	55	48.7	14.3	37	32.7	9.6	37	32.7	9.6		
west	MBE	22	25.0	5.9	23	26.1	6.1	35	39.8	9.3	30	34.1	8.0	88	376
	RMSE	47	53.4	12.5	44	50.0	11.7	52	59.0	13.8	46	52.3	12.2		
all	MBE	1	0.9	0.3	-3	-2.8	-1.0	10	1.0	3.2	5	4.7	1.2	106	314
slopes	RMSE	40	37.7	12.7	42	39.6	13.4	41	38.7	13.1	38	35.8	12.1		

of the low shading effect and low albedo of the surrounding terrain. However, when the surrounding terrain has higher albedo (snow cover, for instance) and heavy shading effect or the slope is steeper, it is recommended that slope solar radiation be adjusted according to equation 6.2.

All the above models showed similar performance in both MBE and RMSE statistics in the Plateau Mountain area. The disappearance of the advantages of the anisotropic models is obviously attributed to the more transparent atmosphere in high altitudes and the variable mountain clouds. The choice of the "best" model is then influenced by the limitations and relative complexity of the individual model. The isotropic models (Hay and Davies, Klucher) are simpler to use when compared to the Perez et al.'s model. The Perez et al.'s model also has the potential for being location dependent due to the empirical nature of the reduced brightness coefficients. However, recent research has noted that location dependence of this model was negligible (Perez et al., 1990).

6.5 Conclusions

Four existing models for estimating solar radiation on sloping surfaces were presented and evaluated with the data set obtained on Plateau Mountain . The results of evaluation are consistent with the findings of Hay (1986), Hay and McKay (1985), Isard (1986) and Reindl et al. (1990). Models based on the correlation between atmospheric transmissivity and the diffuse fraction perform as well as models using measurements of diffuse solar radiation on horizontal surface. Overall, Perez et al.'s model showed small but consistently better performance, which has a RMSE of typically 15% and a MBE 2% for global solar radiation. However, Hay and Davies, Klucher and the isotropic models have the advantage of simplicity and show comparable figures for the MBE and RMSE. All model can produce slope irradiation estimation to an accuracy within 10.5% for clear sky conditions. The slope radiation adjustment according to equation 6.2 shows insignificant advantages. However, it is suggested that this effect be taken into consideration when the surrounding terrain has heavy shading effects and/or high albedo.

Chapter 7

ESTIMATION OF LONGWAVE RADIATION FOR ALPINE ENVIRONMENTS

7.1 Introduction

For an accurate assessment of the surface radiation exchange in mountainous areas, each component of the energy budget must be evaluated. While a great deal of effort has been directed toward computing the solar radiation components (see Chapter 5 and 6) in mountainous areas, the longwave components of the radiation budget have received much less attention. This is particularly the case for sloping surfaces which make up a major part of alpine areas. The longwave radiation on a sloping surface comes from two sources: the atmosphere and surrounding terrain.

Several different procedures (empirical and analytical) have been developed for calculating cloudless sky longwave radiation by use of screen level measurements. Some of them have been tested by alpine radiation measurements (LeDrew, 1975; Lougeay and Brazel, 1982). However, few firm conclusions have been reached (Saunders, 1990). For the longwave radiation from surrounding terrain, very few studies have been done because of the difficulties in acquiring surrounding terrain temperature and emissivity. No operational model has yet emerged in this regard.

The objective of this chapter is to review and test several currently accepted longwave radiation models both for horizontal surface and sloping surfaces, to assess their relative applicability in alpine environments and to see if some simple yet robust ways to evaluate the longwave radiation for the sloping surfaces can be derived.

7.2 Theoretical Background

The net longwave radiation at an unobstructed horizontal surface (L^*) is

$$L^* = L\downarrow - L\uparrow \tag{7.1}$$

where $L\downarrow$ is incoming longwave radiation and $L\uparrow$ is outgoing longwave radiation. If the surface temperature (T_s) is known, $L\uparrow$ can be determined from the Stefan-Boltzmann law

$$L\uparrow = \varepsilon \sigma T_s^4 + (1 - \varepsilon) L\downarrow \quad (7.2)$$

where ε is the surface emissivity. Emissivity ranges from 0.90 to 0.99 for tundra surfaces (Oke, 1987) and 0.97 to 0.99 for snow and ice (Muller, 1985). Saunders (1990) suggested a value of 0.95 for snow-free alpine tundra surfaces.

Net longwave radiation on a sloping surface (L_s^*) is

$$L_s^* = L_s\downarrow - L_s\uparrow \quad (7.3)$$

where $L_s\uparrow$ is outgoing longwave radiation which can be determined by (7.2). Incoming longwave radiation at a sloping surface includes two components

$$L_s\downarrow = L_{as} + L_{ts} \quad (7.4)$$

where L_{as} is the longwave radiation from atmosphere and L_{ts} the longwave radiation from surrounding terrain within the viewing hemisphere of the slope.

7.3 Models for Incoming Longwave Radiation on Horizontal Surfaces

As described by equation 7.2, outgoing longwave radiation can be estimated accurately if reliable measurements of surface temperature are available. Incoming longwave radiation, however, is more problematic to model since the atmospheric emissivity is a function of both air temperature and the quantity of emitting sources, mainly water vapour. The most common approach for estimating incoming longwave radiation is to approximate the atmospheric emissivity, based on either surface and screen-level measurements (Brunt, 1932; Swinbank, 1963; Idso and Jackson, 1969; Berdahl and Martin, 1984) or upon temperature and vapour pressure profiles (LeDrew, 1975). In a remote alpine area, atmospheric soundings are generally unavailable, so the emissivity approximation must be based on surface or screen level measurements.

Eight models will be tested in this chapter by using the data obtained at an unobstructed horizontal site on Plateau Mountain in 1989. These models are listed in Table 7.1.

Table 7.1 Selected Longwave Radiation Models

Model	Equation Form	Equation
Brunt (1932)	$L\downarrow = \sigma T_a^4 \, (0.604 + 0.048 \sqrt{e})$	(7.5)
LeDrew (1975)	$L\downarrow = \sigma T_a^4 \, (0.491 + 0.067 \sqrt{e})$	(7.6)
Swinbank (1963)	$L\downarrow = \sigma T_a^4 \, (0.92 \times 10^{-5} T_a^2)$	(7.7)
Idso-Jackson (1969)	$L\downarrow = \sigma T_a^4 \, \{ 1 - 0.261 \, [-7.704 \times 10^{-4} (273 - T_a)^2] \}$	(7.8)
Berdahl-Martin (1984)	$L\downarrow = \sigma T_a^4 \, [0.711 + 0.56 (T_{dp}/100) + 0.73 (T_{dp}/100)^2]$	(7.9)
Brutsaert (1975)	$L\downarrow = \sigma T_a^4 \, [1.24 (e / T_a)^{1/7}]$	(7.10)
Idso (1981)	$L\downarrow = \sigma T_a^4 \, [0.179 \, e^{1/7} \exp(350/T_a)]$	(7.11)
Marks-Dozier (1981)	$L\downarrow = \sigma T_a^4 \, [1.24 (e' / T_a')^{1/7}] \, [P_0/1013]$	(7.12)

Note: T_a = air temperature (K), T_{dp} = dewpoint temperature (C), e = vapour pressure (10^{-1} kPa), e'=RH $e_s(T')$, T'= T_a + (0.0065 z), P_0 = station air pressure (10^{-1} kPa), RH = relative humidity at station (%), e_s = saturation vapour pressure (10^{-1}kPa), z = elevation of station (m).

They are of two basic types: those purely empirical (equations 7.5-7.9), based on correlations with actual measurements of the longwave radiation, and those which are more analytical (equation 7.10-7.12), derived on apparently physical grounds. The empirical methods suffer from the necessity to calibrate the appropriate regression coefficients at each location and the analytical models also have assumptions to be satisfied. It should be noted that in all cases the longwave radiation is more sensitive to air temperature. Vapour pressure, however, is a much less sensitive variable than temperature in the longwave radiation models. This suggests that even if the vapour pressure is roughly approximated, the models still can give useful results as long as the temperature data are accurate. In alpine areas, accurate temperature measurements are easy to acquire, but the vapour pressure is difficult to measure, particularly at temperatures below freezing point.

The Brunt model was chosen because it is the first longwave radiation model and its present form is supposed to be applicable to the Northern Hemisphere. The LeDrew model is a modified form of Brunt model by using alpine measurements and high altitude radiosonde data. These two empirical models use both air temperature and vapour pressure as inputs. The Swinbank model and the Idso-Jackson model require only air temperature as input, the assumption being that temperature correlates well with the surface vapour pressure. These temperature-only models have the advantage of requiring simple inputs which are easy to acquire with high accuracy. The Brunt model, the Swinbank model and the Idso-Jackson model have been previously tested by LeDrew (1975) at high elevation on Niwot Ridge, Colorado. The fifth model was developed by Berdahl and Martin (1982). It is an empirical model using both air and dewpoint temperatures as inputs. Since the dewpoint temperature is a function of vapour pressure, it is not surprising that the Brunt model can fit Berdahl and Martin's data equally well (Berdahl and Martin, 1984).

The Brutsaert model is an integration result of Schwarzschild's atmospheric transfer equation under a standard atmosphere. His simple model is more physically based and does not need empirical parameters from radiation measurements. The Marks-Dozier model,

following the Brutsaert model, also requires temperature and vapour pressure as inputs, but incorporates an extrapolation of air temperature to sea level equivalent value, and also pressure-corrects the calculation of emissivity. This model has been tested at high elevations in the Sierra Nevada Mountains.

It should be noted that all the models listed in Table 7.1 are cloudless sky models, although they will be tested here for all sky condition data. The cloudless sky assumption is obviously not true for mountain environments. To accommodate the sky cloudiness, corrections to the cloudless sky model can be used, such as those developed by Bolz (1949)

$$L_c\downarrow = L\downarrow (1+ a_1 n^2) \tag{7.13}$$

and Unsworth and Monteith (1975)

$$\varepsilon_c = \varepsilon_a + 0.84\, n\, (1 - \varepsilon_a) \tag{7.14}$$

where $L_c\downarrow$ is cloudy sky longwave radiation, $L\downarrow$ is cloudless sky longwave radiation, n is the fraction of sky covered by clouds ($0 < n < 1.0$), and a_1 is a variable contingent on cloud type. Oke (1987) has listed its values for different clouds. Since only cloud amount was observed in the experiment, an average of a_1 for all cloud types (0.21) is used in this study. ε_c and ε_a are respectively the atmospheric emissivity for cloudy sky and cloudless sky.

7.4 Models for Longwave Radiation on Sloping Surfaces

As mentioned in previous chapters, the mountainous area is an assemblage of both horizontal and sloping surfaces. Sloping surfaces make up the largest portion of mountain areas. Therefore, in longwave radiation budget research, the longwave radiation on sloping surfaces seems more important than that on horizontal surfaces. Longwave radiation from the atmosphere and from the surrounding terrain both contribute to the longwave irradiance of a sloping surface. Radiation received from the sky portion can be determined in the similar way as discussed in Section 7.3. That received from surrounding terrain depends upon the combined influences of terrain emission and reflection as well as the transmission

and emission by the "air wedge" between the source and the receptor. The latter effects are usually ignored in radiation budget studies and the radiation is assumed to be mainly proportional to the fourth power of the terrain surface temperature.

If we assume that both longwave radiances from the sky and from the ground are isotropic, the longwave irradiance of an unobstructed sloping surface $L_s\downarrow$ would be

$$L_s\downarrow = 0.5\, L\downarrow\, (1 + \cos\alpha) + 0.5\, (\varepsilon\, \sigma\, T_s^4 + L\downarrow - \varepsilon\, L\downarrow)\, (1 - \cos\alpha) \qquad (7.15)$$

where $L\downarrow$ is incoming longwave radiation on horizontal surface (which can be calculated by any one of the models in Table 7.1), α is slope angle, ε ground emissivity and T_s surface temperature.

However, the longwave radiation from the sky hemisphere is anisotropic (Robinson, 1947, 1950; Unsworth and Monteith, 1975; Kondratyev, 1977). This will influence the longwave irradiance to different sloping surfaces. Unsworth (1975) proposed the angular distribution of the atmospheric emissivity

$$\varepsilon(h) = \varepsilon_a - b\, (0.5 - \ln(\mathrm{cosec}\, h)) \qquad (7.16)$$

Using spherical co-ordinate geometry, the atmospheric emissivity facing the sloping surface can be expressed as

$$\varepsilon_{as} = 2 \int_0^{\pi} \int_{h_1}^{\pi/2} \frac{\varepsilon(h)}{\pi}\, f\, dh\, d\psi. \qquad (7.17)$$

where $f = (\sin\alpha \cos h \cos\psi + \cos\alpha \sin h) \cos h$ and the integration limit h_1 is

$$h_1 = \begin{cases} \arccos\left[\dfrac{\cos\alpha}{\sqrt{1 - \sin^2\alpha\, \sin^2\psi}}\right] & \dfrac{\pi}{2} \le \psi \le \pi \\ 0 & 0 \le \psi \le \dfrac{\pi}{2} \end{cases} \qquad (7.18)$$

Using equations 7.16 and 7.18, equation 7.17 may be written as

$$\varepsilon_{as} = \frac{1}{2}\varepsilon_a (1+\cos\alpha) - \frac{1}{4} b (1+\cos\alpha) + \frac{2b}{\pi}\int_0^{\pi}\int_{h_1}^{\pi/2} f \ln(\text{cosec } h)\, dh\, d\psi$$

$$= \quad I_1 \quad + \quad bI_2 \qquad (7.19)$$

The first term (I_1) on the right hand side of (7.19) corresponds to an isotropic distribution of atmospheric emittance and the remaining terms (bI_2) represents the anisotropic component which can be evaluated numerically without any inputs (b=0.088). I_1 and I_2 for the four sloping surfaces on Plateau Mountain are calculated and listed in Table 7.2. Therefore, longwave radiation to a sloping surface can be estimated

$$L_s\downarrow = \varepsilon_{as}\,\sigma\,T_a^4 + 0.5\,(\varepsilon\,\sigma\,T_s^4 + L\downarrow - \varepsilon\,L\downarrow)\,(1 - \cos\alpha). \qquad (7.20)$$

As mentioned before, the slopes receive longwave radiation from both the atmosphere and the ground within the field of view of the slopes. The latter component is theoretically anisotropic as well and can be calculated by numerical integration (Olyphant, 1986a). However, its input requirement prevents its operational use. Fortunately this component is not important except for those very steep slopes or heavily shaded slopes. For example, for an unshaded 30° slope, if the surrounding terrain longwave radiation changes from 250 to 350 Wm^{-2}, its contribution to the slope changes only from 16.7 to 23.4 Wm^{-2}. Therefore, the surrounding terrain longwave radiation is assumed 292 Wm^{-2} for daytime and 266 Wm^{-2} for nighttime, which correspond to the average values of a day during the observation period. In this way, the longwave radiation to a sloping surface can be calculated by equation 7.15 or equation 7.20.

7.5 Outgoing Longwave Radiation and Net Longwave Radiation

Outgoing longwave radiation can be calculated with equation 7.2 if given proper surface emissivity and surface temperature measurements. For this experiment, $\varepsilon = 0.95$ was taken for this alpine tundra. This value is a mean value for tundra specified by Oke (1987) and it is used by Saunders (1990) for a similar alpine area.

Table 7.2 I_1 and I_2 Values for for the Slopes on Plateau Mountain

Orientation	Slope (°)	I_1	I_2
South slope	20	0.9698	0.2110
North slope	31	0.9286	0.2457
East slope	30	0.9330	0.2434
West slope	21	0.9668	0.2153

Another method is to use screen level air temperature (T_a) in the Stefan-Boltzmann equation. This method has the advantage of avoiding the use of surface temperature, since a representative surface temperature is more difficult to obtain than screen level temperature. Saunders (1990) proposed an empirical equation to calculate outgoing longwave radiation

$$L\uparrow = \sigma T_a^4 + 0.1\ K\downarrow \qquad (7.21)$$

based on his data set measured on a snow free alpine tundra (2350 m a.s.l.), Scout Mountain, British Columbia, which is at the same latitude as the present experiment. The second term in the right side of equation 7.21 reflects the radiative surface heating during the daytime. When this equation is used for sloping surfaces, the inputs should be their corresponding values on sloping surfaces (predicted or measured values).

When incoming and outgoing longwave radiation is known, net longwave radiation can be calculated using a flux-by-flux method (i.e. equation 7.1 for horizontal surfaces and equation 7.3 for sloping surfaces).

7.6 Observational Procedure

The field data were collected between June 20 to July 24, 1989 on the Plateau Mountain, southwestern Alberta, Canada. Details of the sites are presented in Chapter 1. On both the horizontal site and the four sloping sites, all data were collected at 10s intervals and stored using Campbell Scientific 21X dataloggers on half-hourly basis.

Incoming longwave radiation was directly measured on both horizontal and sloping sites by two Eppley pyrgeometers. Field intercomparison indicated the good agreement between the two pyrgeometers. Ground surface temperatures were measured with two thermocouple arrays, each with ten thermocouples connected in parallel. Dry- and wet-bulb temperatures at 1m above the ground were obtained by the two psychrometric systems. The vapour pressure was calculated using the dry- and wet-bulb temperatures and the psychrometric equation. Dewpoint temperature was determined by Murray's (1967) equation of saturation vapour pressure. Cloud observations were made on selected days.

The observed cloud amount will be used to discuss the model performance. Outgoing longwave radiation is calculated as a residual from equation 3.1 and net longwave radiation is calculated by equation 7.1 and 7.3.

Mean bias error (MBE) and root mean square error (RMSE) as described by Willmott (1982) are used for model performance assessment. The MBE and RMSE are expressed in both absolute value and percentage.

7.7 Results and Discussion

Incoming Longwave Radiation on a Horizontal Surface

(1) Using cloudless sky models in all sky conditions

The range of the measured values of longwave radiation (657 hourly averages) during the 1989 experiment was from 210 to 363 Wm^{-2}, which corresponds to black body temperature range of –27 to 10°C. Table 7.3 lists each model's MBEs and RMSEs over the whole data, daytime data and nighttime data.

Of the eight models tested under all sky conditions, the Idso model, by incorporating both vapour pressure and air temperature, exhibits the best performance in both MBE and RMSE, followed by Idso-Jackson model and Brutsaert model. The LeDrew model, which was tested at the Front Range of Corolado (Lougeay and Brazel, 1982), and Marks-Dozier model, which was a modified Brutsaert model for use in alpine areas, have the worst performance in this alpine area. The remaining models have virtually the same performance as that of Brutsaert and Idso-Jackson models over all data, daytime data and nighttime data, with MBEs less than 11% (30 Wm^{-2}) and RMSEs less than 16% (47 Wm^{-2}) of the measured values.

One of the significant features in Table 7.3 is that all these models (except the Idso model) underestimate the observed longwave radiation. This could be explained by the influence of clouds. As mentioned before, all these models are actually cloudless sky

Table 7.3 Comparison of the Observed Incoming Longwave Radiation and the Predicted Values on Horizontal Surfaces by Selected Cloudless Longwave Radiation Models

Model	All Data Mean: 284 Wm^{-2}		Daytime Data Mean: 292 Wm^{-2}		Nighttime Data Mean: 266 Wm^{-2}	
	MBE Wm^{-2}	RMSE Wm^{-2}	MBE Wm^{-2}	RMSE Wm^{-2}	MBE Wm^{-2}	RMSE Wm^{-2}
Brunt	-24.7	44.5	-29.0	42.5	-14.2	35.3
	-8.7 %	14.3 %	-9.9 %	14.6 %	-5.4 %	13.3 %
LeDrew	-47.0	56.2	-51.4	59.3	-36.0	47.6
	-16.5 %	19.8 %	-17.6 %	20.3 %	-13.5 %	17.9 %
Swinbank	-25.5	45.0	-28.4	46.8	-18.3	40.2
	-9.0 %	15.8 %	-9.7 %	16.0 %	-6.9 %	15.1 %
Idso-Jackson	-15.8	39.6	-19.1	40.8	-7.6	36.4
	-5.5 %	13.9 %	-6.5 %	14.0 %	-2.8 %	13.7 %
Berdahl-Martin	-28.0	42.1	-32.3	44.3	-17.6	36.1
	-9.9 %	14.8 %	-11.1 %	15.2 %	-6.6 %	13.6 %
Brutsaert	-25.0	39.4	-29.3	41.4	-14.6	33.9
	-8.8 %	13.9 %	-10.0 %	14.2 %	-5.5 %	12.7 %
Idso	6.3	30.1	1.5	28.0	18.0	34.9
	2.2 %	10.6 %	0.5 %	9.6 %	6.8 %	13.1 %
Marks-Dozier	-68.5	75.0	-73.5	79.0	-56.3	64.3
	-24.1 %	26.4 %	-25.2 %	27.1 %	-21.2 %	24.2 %

longwave radiation models. When they are used to predict the cloudy sky longwave radiation, they will underestimate the observed value because increasing cloud cover will cause an increase in incoming longwave radiation. Nevertheless, even without any cloudiness correction, the use of these cloudless sky models (except Marks-Dozier model and LeDrew model) under all sky conditions will result in MBEs less than 11% and RMSEs of no more than 16% of the mean observed values.

A examination of the results in Table 7.3 reveals that Marks-Dozier model and LeDrew model always tend to underestimate the incoming longwave radiation. The underestimation has been noted by Marks and Dozier (1979) and Lougeay and Brazel (1982). It may not be due to the inefficiencies of the model construct, but to the advective or inversion effects on air temperature and relative humidity in the local areas. This method assumes constant relative humidity and dry adiabatic air temperature lapse rate extrapolated to sea level corresponding values to produce the necessary effective emissivity. However, these assumptions are rarely satisfied in alpine areas during the summer when convective clouds are dominant.

Although LeDrew's empirical model (modified Brunt's relationship) was developed and tested in alpine area (LeDrew, 1975; Lougeay and Brazel, 1982), it does not perform well in this alpine environment under all sky conditions. This again exposes the deficiency of the empirical models. It is difficult to suggest universally useful coefficients for Brunt's relationship. Many sets of empirical coefficients, which can fit to different local conditions, are needed to make this model universally valid. This principle is also applicable to those other empirical models which are easily subject to the variation of local conditions.

The Idso-Jackson model, using only the air temperature as input, performs as well as the Brutsaert model and Brunt model. This result could be very important since the other model's need for measured vapour pressure in alpine areas is not easily satisfied under sub-zero air temperatures. Although the Swinbank model also uses only air temperature as the input, it was not developed with sub-zero temperature nor was it verified with alpine data

sets. The validation shows that it will result in a MBE of −26 Wm^{-2} and a RMSE of 45 Wm^{-2} when used in alpine area. However, when it is used under clear sky condition only, the results are greatly improved, with a MBE of 1.6 Wm^{-2} and a RMSE of 18.4 Wm^{-2} (see Table 7.4). These results are consistent with Saunders' (1990) conclusion: the temperature-only models can work as well as those using both temperature and vapour pressure as inputs. The Idso model is the only one which overestimates the incoming longwave radiation. Its MBE is 7%, yet it has a relatively small RMSE of 14%. Based on the Plateau Mountain data, a revised version of Brunt model is proposed for comparison purposes

$$L\downarrow = \sigma T_a^4 \ (0.539 + 0.081 \sqrt{e}). \qquad (7.22)$$

(2) Using cloudless sky models with cloud-correction

In order to investigate the models' performances under different cloud conditions, the daytime data are subdivided into clear, partly cloudy and cloudy periods based on the clearness indices. The period when atmospheric transmissivity $t \geq 0.7$ is classified as clear, $0.3 < t \leq 0.7$ as partly cloudy sky and $0 < t \leq 0.3$ as cloudy sky condition. The calculated results are also tabulated in Table 7.4.

An examination of the results (Table 7.4) reveals that all models (except Marks-Dozier model and LeDrew model) work equally well under clear sky conditions. Both the MBEs and RMSEs between the predicted and the measured values are reasonably small, less than 5% and 8% respectively. This suggests that these models would provide a good approximation for the prediction of longwave radiation under clear skies over this alpine area. Figure 7.1 shows the results of the Brutsaert model and Idso-Jackson model. The Marks-Dozier model and LeDrew model significantly underestimate the incoming longwave radiation and the Idso model overestimates it under clear conditions. With the increasing cloud cover from clear to cloudy sky, the underestimation becomes more significant, for example, MBE of the Idso-Jackson model changes from 3.2% to -15.9% and that of

Table 7.4 Comparison of the Observed Incoming Longwave Radiation and the Predicted Values on Horizontal Surfaces under Different Sky Conditions by Selected Cloudless Longwave Radiation Models

Model	Clear Mean: 282 Wm^{-2}		Partly Cloud Mean: 289 Wm^{-2}		Cloudy Mean: 305 Wm^{-2}	
	MBE Wm^{-2}	RMSE Wm^{-2}	MBE Wm^{-2}	RMSE Wm^{-2}	MBE Wm^{-2}	RMSE Wm^{-2}
Brunt	-8.1	16.1	-27.8	39.1	-52.5	62.1
	-2.9 %	5.7 %	-9.6 %	13.5 %	-17.2 %	20.3 %
LeDrew	-32.5	35.0	-50.0	56.8	-73.1	79.9
	-11.5 %	12.4 %	-17.3 %	19.6 %	-24.0 %	26.2 %
Swinbank	1.6	18.4	-28.2	41.4	-59.6	69.8
	0.6 %	6.5 %	-9.7 %	14.3 %	-19.5 %	22.9 %
Idso-Jackson	9.1	20.1	-18.9	35.4	-48.5	60.4
	3.2 %	7.1 %	-6.5 %	12.3 %	-15.9 %	19.8 %
Berdahl-Martin	-12.2	17.9	-31.0	41.1	-55.1	64.0
	-4.3 %	6.3 %	-10.7%	14.2 %	-18.0 %	20.9 %
Brutsaert	-10.4	16.2	-27.9	38.4	-51.1	60.1
	-3.7 %	5.7 %	-9.6 %	13.3 %	-16.7 %	19.7 %
Idso	17.3	21.4	3.2	26.4	-17.7	35.6
	6.1 %	7.6 %	1.1 %	9.1 %	-5.8 %	11.7
Marks-Dozier	-57.2	58.7	-71.8	76.7	-93.2	98.5
	-20.2 %	20.8 %	-24.8 %	26.5 %	-30.5 %	32.2 %

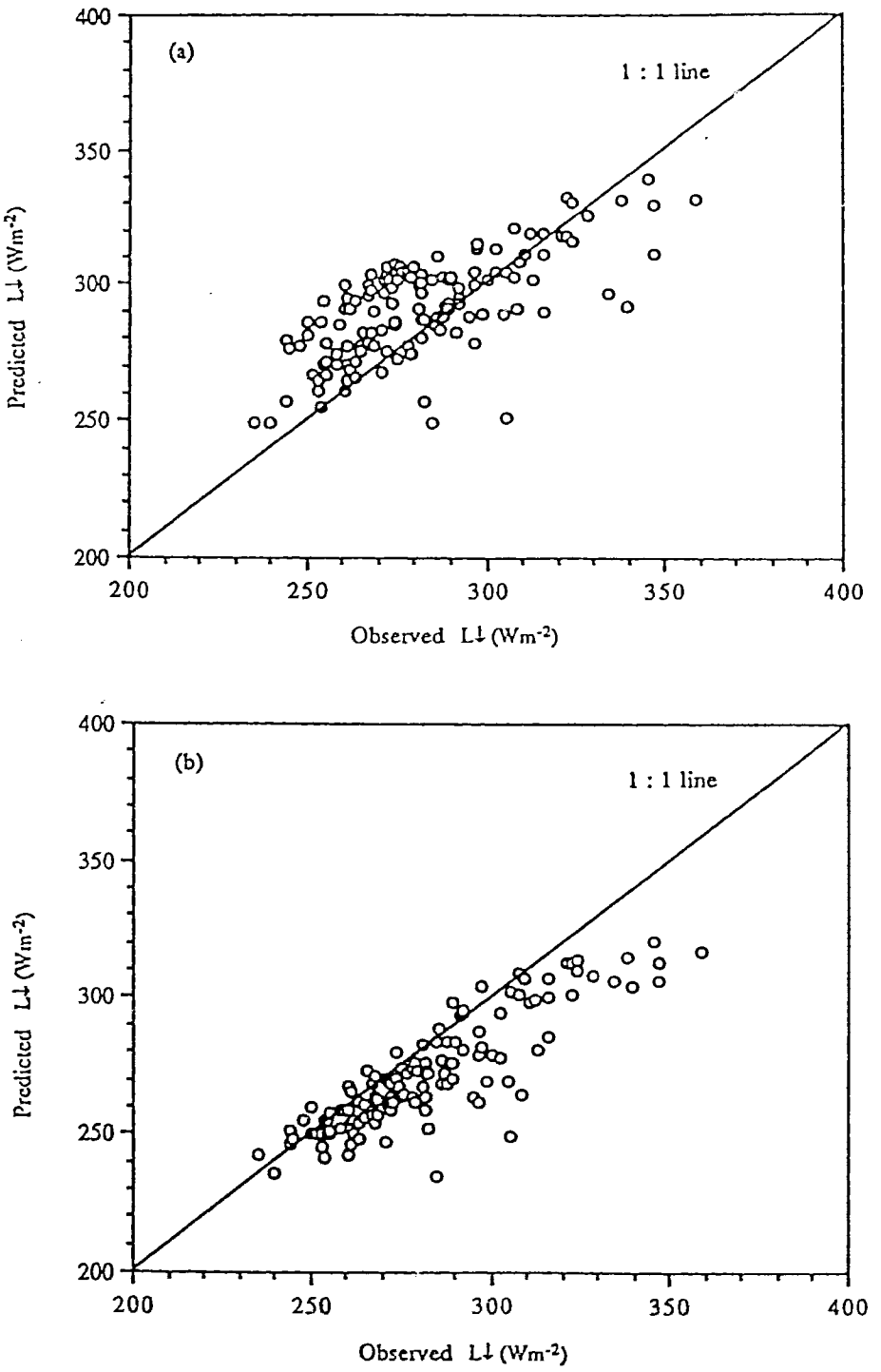

Figure 7.1 Observed hourly incoming longwave radiation versus the predicted values with (a) Idso-Jackson model and (b) Brutsaert model on clear days.

Marks-Dozier model from -20.2% to -30.5%. This clearly shows the enhancement effect of the clouds on incoming longwave radiation.

As discussed in the previous chapters, most alpine weather is partly cloudy or cloudy. Therefore, the use of cloudless sky models in alpine area is not appropriate, and the enhancement effect of clouds should be taken into consideration. The cloud-correction methods proposed by Bolz (1949) and Unsworth and Monteith (1975) (see Section 7.3) are used here. The MBEs and RMSEs before correction and after correction with Bolz method and Unsworth-Monteith method are listed in Table 7.5. Examination of Table 7.5 shows clearly that the MBEs and RMSEs for all models are reduced significantly after cloud correction, and the reduction of errors by Unsworth-Monteith method is more significant than that by Bolz method. These results suggest that in this alpine area under all sky conditions, all models (excluding Marks and Dozier model) can produce incoming longwave radiation prediction with MBEs less than 7% and RMSEs no more than 10% of the measured values if they are used with the Unsworth-Monteith cloudiness correction method. Figure 7.2 shows again the results of the Brutsaert model and the Idso-Jackson model under all sky conditions but with the Unsworth-Monteith cloudiness correction.

Longwave Radiation on Sloping Surfaces

Longwave radiation on sloping surfaces comes from two sources: the atmosphere and the surrounding terrain seen by the sloping surface. The isotropic model (equation 7.15) and the anisotropic model described by equation 7.20 were tested over all data, under different sky conditions and on different slopes. In the test, the Idso model was used to calculate incoming longwave radiation on horizontal surface. The test results are tabulated in Table 7.6, 7.7 and 7.8. Generally speaking, the simpler isotropic model works a little better than the more complex anisotropic model. However, their difference is not appreciably significant. The results suggest that for slopes up to 30° using the isotropic

Table 7.5 Comparison of the Observed Incoming Longwave Radiation and the Predicted Values on Horizontal Surfaces by Selected Cloudless Longwave Radiation Models with Cloudiness Correction

Model	No Correction Mean: 284 Wm^{-2}		Bolz Correction Mean: 284 Wm^{-2}		Unsworth-Monteith Mean: 284 Wm^{-2}	
	MBE Wm^{-2}	RMSE Wm^{-2}	MBE Wm^{-2}	RMSE Wm^{-2}	MBE Wm^{-2}	RMSE Wm^{-2}
Brunt	-27.5	42.1	-18.1	29.7	-1.7	19.1
	-9.7 %	14.8 %	-6.4 %	10.5 %	-0.6 %	9.1 %
LeDrew	-51.1	59.4	-42.5	48.2	-19.3	26.0
	-18.0 %	20.9 %	-15.0 %	17.0 %	-6.8 %	9.1%
Swinbank	-24.7	46.6	-15.5	35.0	1.7	23.7
	-8.7 %	14.2 %	-5.5 %	12.3 %	0.6 %	8.3 %
Idso-Jackson	-14.9	40.4	-5.3	29.4	8.4	24.9
	-5.3 %	15.0 %	-1.9 %	10.3 %	3.0 %	8.8 %
Berdahl-Martin	-31.7	44.5	-22.5	32.1	-5.0	19.0
	-11.2 %	15.7 %	-7.9 %	11.3 %	-1.8 %	6.7 %
Brutsaert	-29.8	42.3	-20.4	29.8	-3.8	18.4
	-10.5 %	14.9 %	-7.2 %	10.5 %	-1.3 %	6.5 %
Idso	1.0	28.2	11.6	22.7	18.1	27.2
	0.3 %	9.9 %	4.1%	8.0 %	6.4 %	9.6 %
Marks-Dozier	-72.4	77.9	-64.6	68.2	-35.1	39.5
	-25.5 %	27.5 %	-22.7 %	24.0 %	-12.4 %	13.9 %

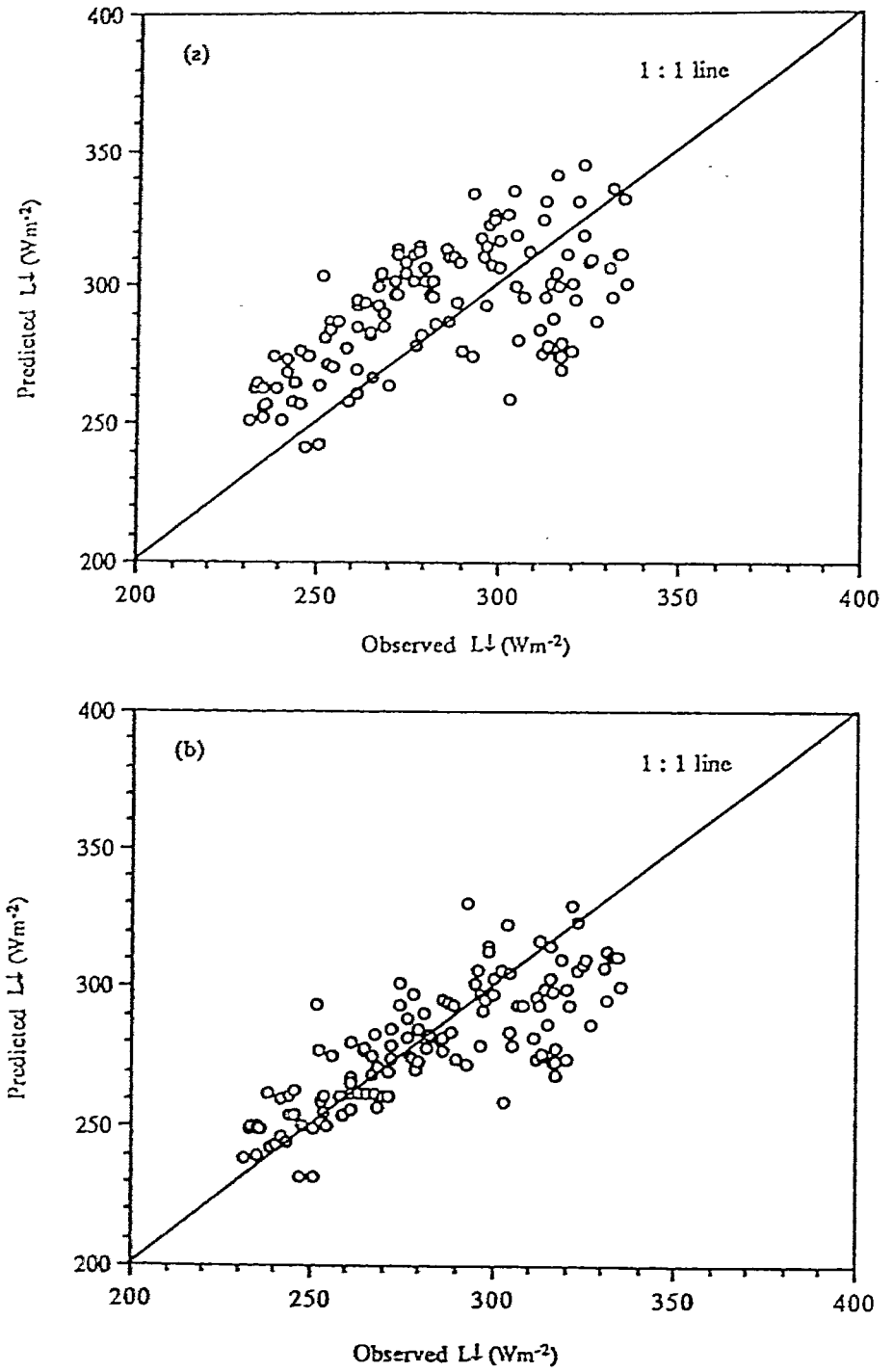

Figure 7.2 Observed hourly incoming longwave radiation versus the predicted values by (a) Idso-Jackson model and (b) Brutsaert model with Unsworth-Monteith cloudiness correction.

Table 7.6 Comparison of the Observed Hourly Average Longwave Radiation on Sloping Surfaces and Predicted Values Using the Isotropic and Anisotropic Models

Model	All Data Mean: 275 Wm^{-2}		Daytime Data Mean: 283 Wm^{-2}		Nighttime Data Mean: 260 Wm^{-2}	
	MBE Wm^{-2}	RMSE Wm^{-2}	MBE Wm^{-2}	RMSE Wm^{-2}	MBE Wm^{-2}	RMSE Wm^{-2}
Isotropic	12.8	29.2	8.4	26.1	22.0	34.6
	4.7 %	10.6 %	3.5 %	9.2 %	8.4 %	13.3 %
Anisotropic	19.9	32.9	15.6	29.2	28.8	39.4
	7.2 %	11.9 %	5.5 %	12.3 %	11.1 %	15.0 %

Table 7.7 Comparison of the Observed Hourly Average Longwave Radiation on Sloping Surfaces and Predicted Values Using the Isotropic and Anisotropic Models under Different Sky Conditions

Model	Clear Mean: 289 Wm^{-2}		Partly Cloudy Mean: 282 Wm^{-2}		Cloudy Mean: 278 Wm^{-2}	
	MBE Wm^{-2}	RMSE Wm^{-2}	MBE Wm^{-2}	RMSE Wm^{-2}	MBE Wm^{-2}	RMSE Wm^{-2}
Isotropic	-5.2	29.5	9.1	25.5	18.8	23.9
	-1.8 %	10.2 %	3.2 %	9.0 %	6.8 %	8.6 %
Anisotropic	1.6	28.9	16.3	28.8	26.6	30.3
	0.5 %	10.0 %	5.8 %	10.2 %	9.6 %	18.9 %

Table 7.8 Comparison of the Observed Hourly Average Longwave Radiation on Sloping Surfaces and Predicted Values for Different Slopes by Using the Isotropic and the Anisotropic Models

Model	South Slope Mean: 300 Wm^{-2}		North Slope Mean: 272 Wm^{-2}		East Slope Mean: 285 Wm^{-2}		West Slope Mean: 252 Wm^{-2}	
	MBE Wm^{-2}	RMSE Wm^{-2}	MBE Wm^{-2}	RMSE Wm^{-2}	MBE Wm^{-2}	RMSE Wm^{-2}	MBE Wm^{-2}	RMSE Wm^{-2}
Isotropic	-1.2	24.2	3.4	24.7	14.3	28.3	28.2	35.2
	-0.4 %	8.1 %	1.2 %	9.1 %	5.0 %	9.9 %	11.2 %	14.0 %
Anisotropic	5.3	34.8	10.7	26.8	22.2	33.0	32.0	37.7
	1.8 %	8.3 %	3.9 %	9.3 %	7.8 %	11.6 %	12.7 %	15.0 %

model (7.15) can predict longwave radiation to an accuracy of within 11% of the observed value (RMSE = 30 Wm^{-2}) (Table 7.6). The results in Table 7.7 show that cloudiness would not significantly affect the model performance since the Idso model (used to calculate L↓) can work well under all sky conditions. Table 7.8 shows the test results of both models for the four different sloping surfaces. The differences in MBEs and RMSEs between the slopes are mainly the effect of local surrounding conditions rather than the models themselves. Nevertheless, use of these models will result in a RMSE less than 15% of the observed values.

Outgoing Longwave Radiation on Sloping Surfaces

From knowledge of surface emissivity and surface temperature, outgoing longwave radiation can be successfully calculated by equation 7.2. Equation 7.21, using air temperature and incoming solar radiation as inputs, was tested with Plateau Mountain data. The results show that it overestimates outgoing longwave radiation of the horizontal site in both daytime (MBE = 22 Wm^{-2}, RMSE = 27.2 Wm^{-2}) and nighttime (MBE = 18.1 Wm^{-2}, RMSE = 20.4 Wm^{-2}). Considering this, a modified empirical equation is proposed for Plateau Mountain:

$$L\uparrow = 0.95\ \sigma\ T_a^4 + 0.075\ K\downarrow + 5.1\ . \qquad (7.24)$$

$$(n = 903,\ r = 0.73,\ S.E. = 13.6\ Wm^{-2})$$

As discussed by Saunders (1990), this model is inappropriate for snow-covered surfaces. Even when the ground is wet, it can cause significant errors. However, it has the advantage of requiring data which are routinely observed. Equation 7.24 was used to estimate the outgoing longwave radiation of sloping surfaces. The measured temperature and solar radiation on sloping surfaces are used as inputs to equation 7.24 since the purpose is to test equation 7.24 on sloping surfaces. The test results show that using equation 7.24 on sloping surfaces gave a RMSE of less than 26 Wm^{-2} although with a MBE of about 24 Wm^{-2}.

Net longwave Radiation on Sloping Surfaces

Given the incoming longwave radiation to a sloping surface (equation 7.15) and the outgoing longwave radiation of the sloping surface (equation 7.24), net longwave radiation is determined by equation 7.3, a flux-by-flux approach. The test results show that using this method results in a MBE of -8.4 Wm^{-2} and a RMSE of 25.5 Wm^{-2} (Figure 7.3).

7.8 Conclusions

The results of this study show that most traditional longwave radiation models (Brunt model, Berdahl-Martin model and Brutsaert model) which incorporate both vapour pressure and air temperature provide useful methods for estimating incoming longwave radiation. Even the temperature-only models (such as the Idso-Jackson model) can work equally well. The Marks-Dozier model, although was designed for alpine use, performed the worst under all sky conditions, always tended to overestimate the incoming longwave radiation.

All the cloudless sky models (except the Marks-Dozier model and the Idso model) work equally well under clear sky conditions and they can produce predictions with high accuracy (MBEs less than 5% and RMSEs less than 8%). Even under all sky conditions, they will result in MBEs no more than 10% and RMSEs less than 16%. Under all sky conditions but incorporating Unsworth and Monteith's cloudiness correction, their performance can be greatly improved, with MBEs less than 5% and RMSEs less than 10%.

More alpine measurements are still needed to make extensive validation of the models. The measurement and modelling of longwave radiation on sloping surfaces is especially needed.

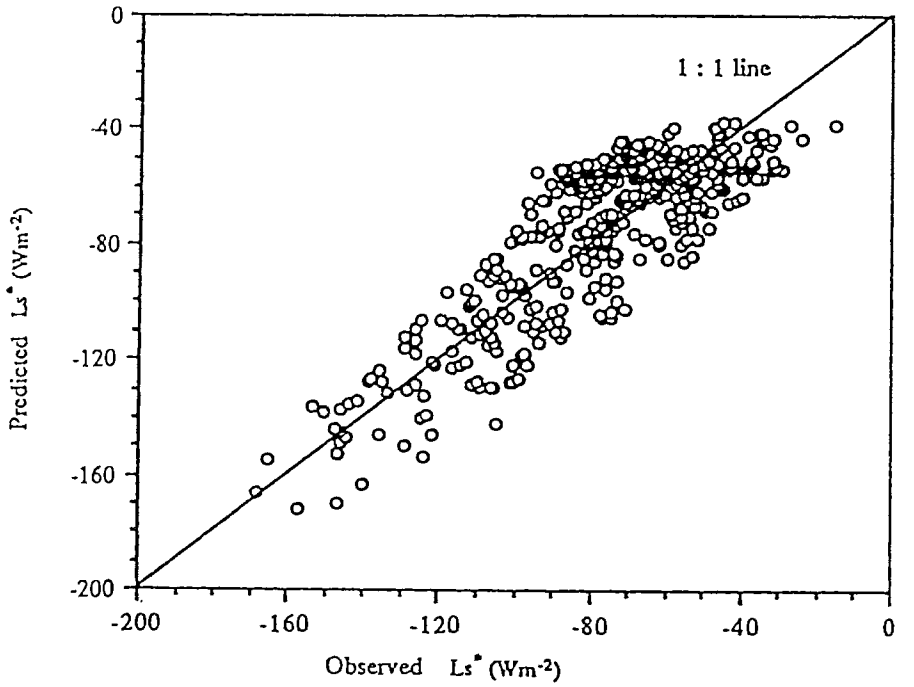

Figure 7.3 Observed hourly net longwave radiation on sloping surfaces versus the predicted values with the flux-by-flux method.

Chapter 8

ESTIMATION OF NET RADIATION FOR ALPINE ENVIRONMENTS

8.1 Introduction

As mentioned in previous chapters, alpine areas are characterized by a wide range of slopes facing different directions. For a complete alpine radiation budget study, measurements of the net radiation and its components for different slopes are required. It is obviously impractical to measure net radiation on all slopes. Therefore the other alternative is to use models. Unfortunately, very few studies have been directed at this aspect in the past. The objective of this chapter is to examine two approaches for estimating net radiation for alpine slopes. One is called the flux-by-flux method which involves modelling all the components of radiation budget and the other is an empirical method which uses the relations between net radiation and global solar radiation.

8.2 Theoretical Background

(1) Flux-by-flux method

Mountainous environments consist of horizontal surfaces and sloping surfaces with different inclinations and orientations. The radiation balance (or net radiation) of a sloping surface Q_s^* is the sum of net solar radiation K_s^* and net longwave radiation L_s^* received on the slope:

$$Q_s^* = K_s^* + L_s^* = (K_s\downarrow - K_s\uparrow) + (L_s\downarrow - L_s\uparrow) \qquad (8.1)$$

where $K_s\downarrow$ is the global solar radiation, $K_s\uparrow$ reflected solar radiation, $L_s\downarrow$ incoming longwave radiation and $L_s\uparrow$ outgoing longwave radiation. Here the subscript s denotes that the flux densities are on the sloping surfaces. The flux-by-flux method involves the modelling of the four components: $K_s\downarrow$, $K_s\uparrow$, $L_s\downarrow$ and $L_s\uparrow$. $K_s\uparrow$ can also be substituted by surface albedo as $K_s\uparrow = AK_s\downarrow$.

For the determination of $K_s\downarrow$, the isotropic model (see Chapter 6) was used:

$$K_s\downarrow = S_h (\cos i / \cos Z) + 0.5 D_h (1 + \cos \alpha) + 0.5 K\downarrow A (1 - \cos \alpha) \qquad (8.2)$$

where S_h, D_h and $K\downarrow$ are respectively direct beam, diffuse and global solar radiation on horizontal surface, Z is solar zenith angle, i the beam solar radiation incident angle to the slope and α the slope angle. The surrounding terrain albedo A is assumed as 0.18, which is the average albedo of the tundra surface on Plateau Mountain during the experiment period of 1989.

Measured $K_s\uparrow$ is used in the flux-by-flux method since the objective of this study is to test the combined result of the models for $K_s\downarrow$, $L_s\downarrow$ and $L_s\uparrow$.

For the determination of $L_s\downarrow$, the following isotropic model was used, which was tested with data from Plateau Mountain (see Chapter 7)

$$L_s\downarrow = 0.5 L\downarrow (1 + \cos \alpha) + 0.5 (\varepsilon \sigma T_s^4 + L\downarrow - \varepsilon L\downarrow) (1 - \cos \alpha). \qquad (8.3)$$

The second term represents longwave radiation from surrounding terrain which was assumed 292 Wm^{-2} for daytime and 266 Wm^{-2} for nighttime, corresponding to an average value during the observation period. $L\downarrow$ is longwave radiation on horizontal surface and can be calculated from Idso model (see Table 7.1)

$$L\downarrow = \sigma T_a^4 [0.179 e^{1/7} \exp(350 / T_a)] \qquad (8.4)$$

where e and T_a are screen level vapour pressure (10^{-1}kPa) and air temperature (K) on the horizontal site.

The outgoing longwave radiation $L_s\uparrow$ estimated by (Chapter 7)

$$L_s\uparrow = 0.95 \sigma T_{as}^4 + 0.75 K_s\downarrow + 5.1 \qquad (8.5)$$

where T_{as} is measured air temperature on sloping surfaces and $K_s\downarrow$ is estimated by equation 8.2.

(2) Empirical Method

As already discussed in Chapter 3, the relatively conservative effects of longwave radiation and surface albedo imply that net radiation is an empirical function of global solar radiation. Several models have been suggested in the literature and most of them used data

from nonalpine area (Davies, 1967; Fritschen, 1967). From alpine environments, Isard (1989) proposed an empirical model

$$Q^* = 0.74\ K\downarrow - 66 \quad (Wm^{-2}) \tag{8.6}$$

for 31 hours of data from an alpine fellfield. Saunders (1990) developed

$$Q^* = 0.664\ K\downarrow - 26 \quad (Wm^{-2}) \tag{8.7}$$

for the 1113 hours of data from Scout Mountain. Bailey et al. (1989) found that

$$Q^* = 0.680\ K\downarrow - 57 \quad (Wm^{-2}) \tag{8.8}$$

for 465 hours of data from Plateau Mountain in 1985. However, data from the same area during the same season of 1989 (the present experiment) yielded

$$Q^* = 0.732\ K\downarrow - 48 \quad (Wm^{-2}). \tag{8.9}$$

As mentioned in Chapter 3, the small difference between (8.8) and (8.9) may reflect the year-to-year climatic variation. In the summer of 1985, clear sky conditions prevailed, but it was mostly cloudy in the summer of 1989. For comparison purposes, the same relations for sloping surfaces are also evaluated (Table 4.2). Table 4.2 and equations 8.6 - 8.9 show that the present relations are all similar to those developed by other authors from other alpine environments (Saunders, 1990; Isard, 1989). Therefore, equation 8.9 will be used as an empirical method to estimate the daytime net radiation on sloping surfaces

$$Q_s^* = 0.732\ K_s\downarrow - 48 \quad (Wm^{-2}) \tag{8.10}$$

where the subscript s again represents the values on sloping surfaces.

During nighttime, $K_s\downarrow = 0$ and then $Q_s^* = L_s^* = -40\ Wm^{-2}$. This is not the case, since Q_s^* could change between 0 and -150 Wm^{-2} depending on the air temperature and sky conditions. Therefore, the flux-by-flux method would have merit during nighttime situations.

8.3 Experimental Procedure

The radiation measurements were obtained between June 20 and July 24, 1989 on Plateau Mountain (50°15' N, 114°31' W, 2300 - 2475 m a.s.l.), southwestern Alberta, Canada. Detail of the sites and measurement systems was presented in Chapters 1 and 4.

On the horizontal site, global solar and reflected solar radiation were measured with an Eppley PSP Precision pyranometer and a Middleton CN-7 pyranometer. A third Eppley PSP Precision pyranometer mounted with a shadow band was used to measure the diffuse radiation on the horizontal surface. Incoming longwave radiation was measured with an Eppley pyrgeometer, and net radiation with a Middleton CN-1 net pyrradiometer. Air temperature and vapour pressure were determined by a psychrometric system. All data were collected by a Campbell Scientific 21X datalogger, which measured sensor signals at 10-second interval and stored half-hourly means. Hourly means were derived from the half-hourly means. On the four sloping sites, all items corresponding to those of horizontal site were measured (except diffuse solar radiation).

Like previous chapters, mean bias error (MBE) and root mean square error (RMSE) as described by Willmott (1982) were used for model performance assessment.

8.4 Results and Discussion

The data used in this study are all daytime data. The whole data set is subdivided for different sky conditions according to the clearness index: clear ($t \geq 0.7$), partly cloudy($0.3 < t < 0.7$) and cloudy ($t \leq 0.3$). Figure 8.1 shows the plots of hourly measured against calculated values of net radiation on the four Plateau Mountain slopes by using empirical method and flux-by-flux method. The performance assessment of the two approaches over different sky conditions is summarized in Table 8.1.

Examining Figure 8.1 and Table 8.1 clearly shows that the simple empirical method produced persistent better performance over the flux-by-flux approach under any sky condition. The systematic error of prediction (indicated by MBE) exhibits the same trend for the empirical method and flux-by-flux method: underestimation of the Q_s^* under cloudy sky conditions (MBE = -11 and -17 Wm^{-2}, respectively) and overestimation of the Q_s^* under clear sky conditions (MBE = 22 and 27 Wm^{-2} respectively). The overestimation or underestimation of the flux-by-flux method is a combined effect of all the errors introduced by the different components.

Table 8.1 Comparison of the Observed Hourly Average Net Radiation on Sloping Surfaces and the Predicted Values Using the Empirical Method and Flux-by-Flux Method

Model	All Sky Conditions Mean: 251 Wm^{-2}		Cloudy Mean: 85 Wm^{-2}		Partly Cloudy Mean: 214 Wm^{-2}		Clear Mean: 367 Wm^{-2}	
	MBE Wm^{-2}	RMSE Wm^{-2}	MBE Wm^{-2}	RMSE Wm^{-2}	MBE Wm^{-2}	RMSE Wm^{-2}	MBE Wm^{-2}	RMSE Wm^{-2}
Empirical	4.4	53.1	-11.2	43.2	-4.7	52.4	21.9	57.7
	1.8 %	21.1 %	-13.1 %	50.5 %	-2.2 %	24.5 %	6.0 %	15.7 %
Flux-by-Flux	4.8	64.0	-16.6	43.9	-6.2	61.4	27.1	73.5
	1.9 %	25.4 %	-19.4 %	51.4 %	-2.9 %	28.7 %	7.4 %	20.0 %

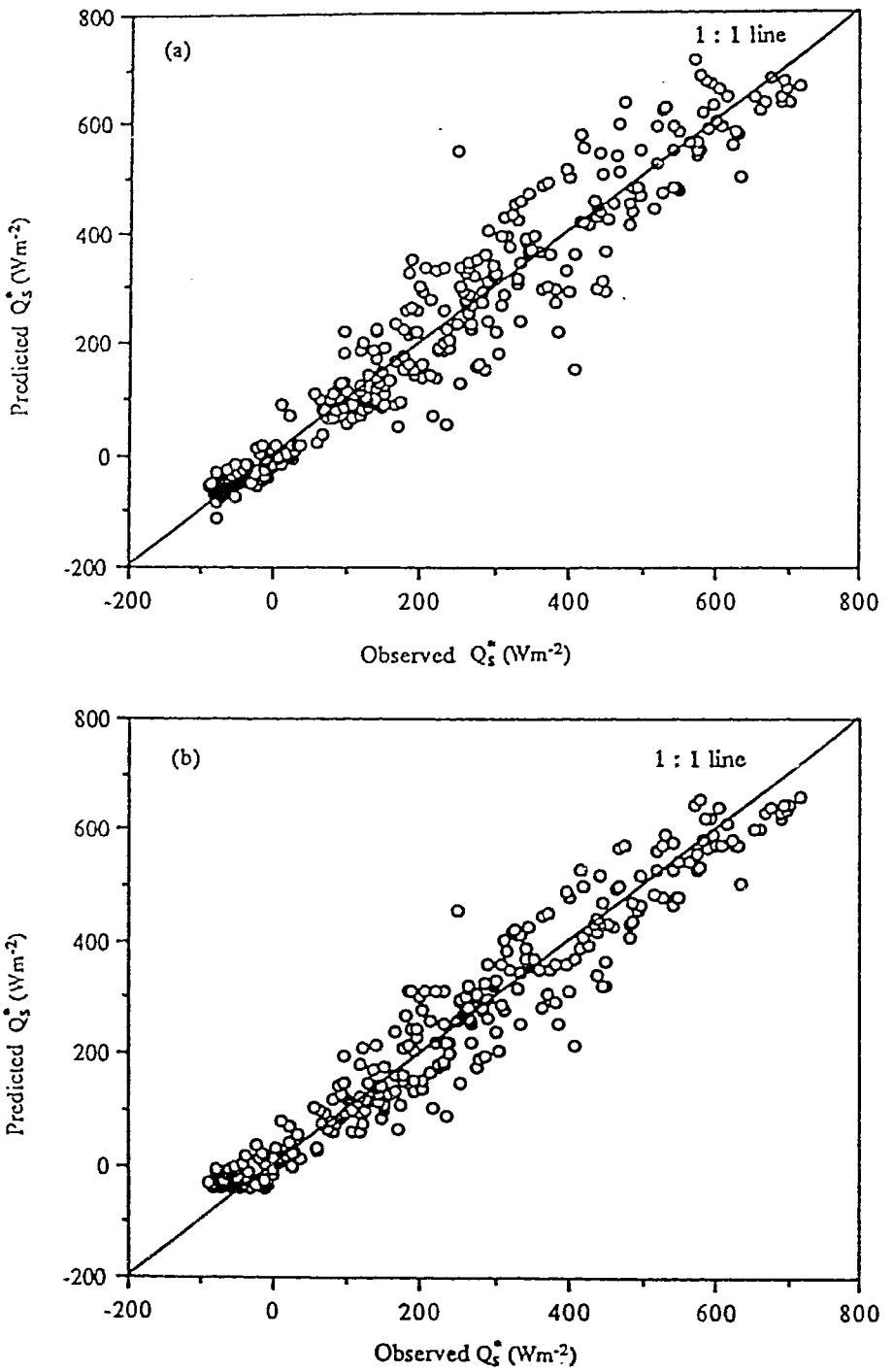

Figure 8.1- Observed versus the predicted net radiation on sloping surfaces by (a) the flux-by-flux method and (b) the empirical method.

The nonsystematic error (RMSE) of the prediction shows that under clear sky conditions the empirical method can predict the hourly Q* to within about ± 58 Wm^{-2} or to within about 16% of the measured values on sloping surfaces, with a relatively small overestimation of 6%. With the increase of cloudiness the absolute value of RMSE decreases, but the percentage value of RMSE increases since the measured Q_s^* decreases with the increasing cloudiness. This reveals that the inappropriateness of the empirical method for the period when solar radiation is low, as it is the case for night.

As mentioned above, the RMSE of the flux-by-flux method is also a combined effect of errors introduced by the different flux components, typically 56 Wm^{-2} for $K_s\downarrow$ (Chapter 6), 30 Wm^{-2} for $L_s\downarrow$ and 26 Wm^{-2} for $L_s\uparrow$ (Chapter 7). The test results in Table 8.1 show that the flux-by-flux method gave a RMSE of 73.5 Wm^{-2} or 20% of the measured Q_s^* value under clear sky conditions. This accuracy is acceptable when considering the accuracy of $K_s\downarrow$, $L_s\downarrow$ and $L_s\uparrow$.

8.5 Conclusions

Two approaches to calculate the net radiation on sloping surfaces are proposed and tested. They are the empirical method based on the relation of $Q_s^* = f(K_s\downarrow)$ and the flux-by-flux method involving the calculation of the individual components $K_s\downarrow$, $K_s\uparrow$, $L_s\downarrow$ and $L_s\uparrow$. The results show that the empirical method was capable of predicting hourly Q_s^* to within about ± 53 Wm^{-2} under all sky conditions. With clear sky conditions, it could predict Q_s^* to within ± 58 Wm^{-2} or 16% of the measured values.

The flux-by-flux method, although it did not perform as well as the empirical method, could work adequately and could give a reasonable RMSE of less than 74 Wm^{-2} (20%) and a MBE of 27 Wm^{-2} (7.4%).

Chapter 9

SUMMARY

9.1 Introduction

This study has provided a description of radiation budget measurements on both horizontal and sloping surfaces for an alpine tundra. The high quality measurements have been used to test and derive models for estimating radiation budget components, especially on sloping surfaces. Given the paucity of alpine radiation budget research, the results of the present study represent an important addition to the present state of knowledge. Noteworthy contributions from the present study include the description of the radiation budget on both horizontal and sloping surfaces in alpine environments and the validation of physically based and empirical models for estimating hourly radiation flux densities on both horizontal and sloping surfaces.

In the following sections, the general findings regarding the radiation budget measurement and modelling are summarized. Some problems are briefly discussed and possible future directions are suggested.

9.2 Measurements of Radiation Budget Components

The results of the high quality measurements on Plateau Mountain in 1989 confirmed the conclusions of the previous study in 1985 (Bowers, 1988; Bailey et al., 1989). At this high altitude site under clear sky conditions, the daily transmissivity was as high as 0.8 and hourly averages can reach 0.85. This high transmissivity produced a very high solar radiation flux density. Due to the high altitude, the diffuse fraction of global solar radiation was 8% to 11%, which is close to that reported by Whiteman et al. (1989) and much lower than the value at sea level (0.15 - 0.20) (Miller, 1981). The large differences of global solar radiation between horizontal surface and sloping surfaces were mainly the results of the differences in the receipt of direct beam solar radiation. The two important factors affecting

the receipt of solar radiation on sloping surfaces were slope self-shading and surrounding terrain shading. During heavy cloud periods, however, this difference diminished.

The daily albedo was essentially constant during the observation period (0.18), which was similar to that observed for snow-free arctic and subarctic sites. Although the diurnal trend of albedo was a function of the incident angle of the direct beam radiation and is symmetrical about the maximum solar incident angle, it was relatively invariant when the incident angle is large. The conservative variations of daily and hourly albedo result in atmospheric transmissivity controlling mainly the global solar radiation and net solar radiation.

Compared with solar radiation, both incoming and outgoing longwave radiation were conservative. The incoming longwave radiation on the sloping surfaces and the horizontal surface has no significant difference because the sky view factor is large and the effects of cloud cover may overshadow the difference. The outgoing longwave radiation had a small diurnal trend (similar to that of global solar radiation). It was almost counter-balanced by incoming longwave radiation. Therefore, net longwave radiation was much smaller than net solar radiation. Net radiation was controlled by global solar radiation.

9.3 Modelling of Radiation Budget Components

The data obtained at Plateau Mountain allowed the testing of the applicability of models for estimating all radiation budget components on sloping surfaces. Solar radiation modelling focussed on the testing of existing models for separating diffuse and direct beam solar radiation from global solar radiation, and models for estimating slope solar radiation. The longwave radiation flux modelling focused on modelling the net longwave radiation components. Longwave radiation modelling has received minimal attention in the alpine tundra zone (Saunders, 1990) and no study has yet been undertaken on sloping surfaces. Finally, two approaches were suggested and tested for their applicability to estimate Qs^*.

In order to estimate the global solar radiation incident on sloping surfaces from its measurements on a horizontal surface, separation of the direct beam and diffuse components of global solar radiation is required. This can be done by direct measurement or modelling. Three hourly models and three daily models were tested for their applicability in this alpine environment. The results are consistent with the findings of Olyphant (1984) and Isard (1985). The large positive MBEs (systematic overestimations) suggested that none can be used in this alpine environment without prior modification. Considering this suggestion, a modified model (formulated by Erbs et al., 1982) was proposed.

By assuming an isotropic reflection from surrounding terrain, four existing models were tested for their performance in estimating solar radiation for sloping surfaces. All models produced negligible MBEs and could predict slope irradiation to an accuracy of within $\pm$ 56 Wm^{-2}, or 10.4% under clear sky conditions. Even under all sky conditions, these models could still predict slope solar irradiance to an accuracy of within $\pm$ 44 Wm^{-2}, or 15% of the measured values, with a negligible bias. Given the fact of the variable nature of the mountain clouds, the disappearance of the advantages of the anisotropic models is understood. The choice of the best model will be influenced by the limitations and relative complexity of the individual model.

Eight longwave radiation models were tested against the measurements. The results show that most traditional atmospheric radiation models can provide useful methods for estimating atmospheric radiation. The model using temperature only and the models using both temperature and vapour pressure can work equally well. Under clear sky conditions, they can predict with high accuracy (MBEs less than 14 Wm^{-2} and RMSEs no more than 22 Wm^{-2}). Under all sky conditions with the incorporation of a cloudiness correction, they still can produce high accuracy predictions.

Two longwave radiation models (one is isotropic and the other anisotropic) for estimating longwave radiation for sloping surfaces were suggested and tested with the measurements. Although highly simplified, the isotropic model showed persistently better

performance than the more complex anisotropic model. The influence of clouds and surrounding terrain may overshadow the anisotropic behavior. The results suggested that using the models will result in a MBE less than 20 Wm^{-2} (or 8%) and RMSE less than 35 Wm^{-2} (or 12%).

Outgoing longwave radiation can be calculated by a surface emissivity 0.95 and surface temperature. It can also be estimated by using screen level temperature and incoming solar radiation (Saunders, 1990). The empirical model developed with horizontal site data was successfully used for sloping sites. The results show a RMSE less than 26 Wm^{-2} and good agreement. By bringing the incoming and outgoing longwave radiation together, net longwave radiation was calculated by the flux-by-flux method. The error analysis shows a RMSE of 25 Wm^{-2} and a negligible bias.

Based on the measurement results and radiation budget component modelling, two approaches are proposed to calculate the net radiation on sloping surfaces. The results show that both approaches work adequately. Although the flux-by-flux approach explicitly accounts for the changing atmospheric and surface conditions, it is interesting to see that the empirical approach based on $Q_s^* = f(K_s\downarrow)$ gave a better performance than the flux-by-flux method on snow-free alpine tundra. The empirical method was capable of predicting hourly Q_s^* to within 53 Wm^{-2} under all sky conditions with a negligible bias. Even the flux-by-flux method can work satisfactorily (RMSE = 64 Wm^{-2}) if the errors associated with $K_s\downarrow$ are considered. The success of the empirical method suggests that the assumptions of the conservative role of longwave radiation and constant albedo are reasonable. Q_s^* can be estimated from the measurements or the estimates of solar radiation on sloping surfaces.

9.4 Further Research of the Radiation Budget

In most applications of the radiation budget, the spatial distribution of radiant energy is very important. From this study, it is apparent that mapping the spatial distribution of

radiation regime in alpine area is possible and practical, at least for the summer season when the surface is snow-free. However, the approaches for calculating radiation regimes of alpine environments will not be complete until they are tested for applicability in the winter season as well. In this study, the reflection of the surrounding terrain was assumed isotropic. This is appropriate for snow-free surfaces. In winter when the ground is snow-covered, the high albedo and its specular character should be taken into consideration.

The focus in most previous alpine longwave radiation modelling has been to test various published formulae, and has been characterized by inconclusive results (Saunders, 1990). These models again were tested for their utility in alpine environment. However, the lack of sub-zero temperature in the data indicates that further research efforts in this area would be of value.

The outgoing longwave radiation from sloping surface can be calculated by its surface temperature and surface emissivity or estimated by its screen level temperature and incoming solar radiation. The difficulties lie in how to obtain the surface temperature or screen level temperature of surrounding terrain. It is obviously impossible to directly monitor each slope. In this regard, remote sensing techniques may offer potential.

Another future research direction may be the general applications of these models. Upon the completion of refinement and testing, these models can be used to provide the spatial distribution of the net radiation. The net radiation is the driving force behind a wide range of natural processes. First, the net radiation on both horizontal and sloping surfaces will provide the basis for the energy budget of these surfaces, which in turn will assist in the study of alpine microclimatology and wildlife habitat. Secondly, the net radiation can drive snowmelt models and runoff models which could be used in the prediction of flooding and reservoir operations. In fact, the implications of the radiation budget are unlimited, which implies that research on the radiation budget is unlimited as well.

Appendix I

SYMBOLS

a	a solid angle corresponding to the circumsolar zone as seen from a slope
a_1	coefficient
A	albedo (dimensionless)
b	coefficient
b'	coefficient
c	a solid angle corresponding to the circumsolar zone as seen from a horizontal surface
Dh	diffuse solar radiation on horizontal surface (Wm^{-2})
Ds	diffuse solar radiation on a sloping surface (Wm^{-2})
e	vapour pressure ($10^{-1}kPa$)
f	sky view factor (dimensionless)
F	anisotropic function (dimensionless)
F_1	coefficient given by Perez et al. (1987)
F_2	coefficient given by Perez et al. (1987)
h	angular height (degree)
$h(\psi)$	the minimum angular height of a point in the sky at the direction of ψ (degree)
h_i	angular height in the azimuth of i * 10° (degree)
h_0	solar elevation angle (degree)
i	incident angle of solar rays on a given surface (degree)
$I(h,\psi)$	intensity of diffuse radiation in the direction of h and ψ
I_0	solar constant, 1370 Wm^{-2}
K_0	extraterrestrial radiation (Wm^{-2}, MJ $m^{-2}d^{-1}$)
K*	net solar radiation (Wm^{-2}, MJ $m^{-2}d^{-1}$)
K↓	global solar radiation (Wm^{-2}, MJ $m^{-2}d^{-1}$)

$K\uparrow$	reflected solar radiation (Wm^{-2}, $MJ\ m^{-2}\ d^{-1}$)
K_s*	net solar radiation on a sloping surface (Wm^{-2}, $MJ\ m^{-2}\ d^{-1}$)
$K_s\downarrow$	global solar radiation on a sloping surface (Wm^{-2}, $MJ\ m^{-2}\ d^{-1}$)
$K_s\uparrow$	reflected solar radiation of a sloping surface (Wm^{-2}, $MJ\ m^{-2}\ d^{-1}$)
K_t	solar radiation due to the reflection of surrounding terrain (Wm^{-2}, $MJ\ m^{-2}\ d^{-1}$)
$L*$	net longwave radiation (Wm^{-2}, $MJ\ m^{-2}\ d^{-1}$)
$L\downarrow$	incoming longwave radiation (Wm^{-2}, $MJ\ m^{-2}\ d^{-1}$)
$L_c\downarrow$	incoming longwave radiation under cloudy conditions (Wm^{-2}, $MJ\ m^{-2}\ d^{-1}$)
$L\uparrow$	outgoing longwave radiation (Wm^{-2}, $MJ\ m^{-2}\ d^{-1}$)
L_s*	net longwave radiation on a sloping surface (Wm^{-2}, $MJ\ m^{-2}\ d^{-1}$)
$L_s\downarrow$	incoming longwave radiation on a sloping surface (Wm^{-2}, $MJ\ m^{-2}\ d^{-1}$)
$L_s\uparrow$	outgoing longwave radiation on a sloping surface (Wm^{-2}, $MJ\ m^{-2}\ d^{-1}$)
L_{as}	incoming longwave radiation from the atmosphere (Wm^{-2}, $MJ\ m^{-2}\ d^{-1}$)
L_{ts}	incoming longwave radiation from surrounding terrain (Wm^{-2}, $MJ\ m^{-2}\ d^{-1}$)
n	the fraction sky covered by clouds (dimensionless)
P_0	atmospheric pressure (10^{-1}kPa)
PAR	photosynthetically active radiation (Wm^{-2}, $MJ\ m^{-2}\ d^{-1}$)
$Q*$	net radiation (Wm^{-2}, $MJ\ m^{-2}\ d^{-1}$)
Q_s*	net radiation on a sloping surface (Wm^{-2}, $MJ\ m^{-2}\ d^{-1}$)
RH	relative humidity (%)
S_h	direct solar radiation on horizontal surface (Wm^{-2}, $MJ\ m^{-2}\ d^{-1}$)
S_m	direct solar radiation to a surface normal to the solar ray (Wm^{-2}, $MJ\ m^{-2}\ d^{-1}$)
S_s	direct solar radiation on a sloping surface (Wm^{-2}, $MJ\ m^{-2}\ d^{-1}$)
t	transmissivity (dimensionless)
T_a	air temperature (K)
T_{dp}	dew-point temperature (C)
T_s	surface temperature (K)

z	elevation (meter)
Z	solar zenith angle (degree)
α	slope angle (degree)
β	binary coefficient (dimensionless)
γ_1	local terrain shading index (dimensionless)
γ_2	local terrain enhancement index (dimensionless)
δ	the sun's declination (degree)
ε	surface emissivity (dimensionless)
ε_a	atmospheric emissivity for cloudless sky condition (dimensionless)
ε_{as}	atmospheric emissivity as seen by a a sloping surface (dimensionless)
ε_c	atmospheric emissivity for cloudy sky condition (dimensionless)
κ	anisotropic index (dimensionless)
σ	Stefan-Boltzmann constant ($5.67 * 10^{-8}$ Wm^{-2} K^{-4})
ϕ	latitude (degree)
ψ	azimuth of direction (degree)
ψ_α	slope orientation (degree)
ψ_o	solar azimuth (degree)
ω	hour angle (degree)

Appendix II

DERIVATION OF TERRAIN SHADING INDEX AND TERRAIN ENHANCEMENT INDEX FOR DIFFUSE RADIATION ON SLOPE

Under the effects of surrounding terrain shading, the diffuse solar radiation on sloping surface D_s' can be expressed as

$$D_s' = \int_0^{2\pi} \int_{h'(\psi)}^{\pi/2} I(h,\psi) \cos i \cos h \, dh \, d\psi \qquad (1)$$

where $h'(\psi)$ is the shading angle of surrounding terrain which is a function of azimuth angle (ψ), $I(h,\psi)$ the intensity of radiation scattered in the direction determined by co-ordinates h (angular height) and ψ (azimuth of direction) and i the incident angle of radiation to the slope. It is determined by

$$\cos i = \cos \alpha \sin h + \sin \alpha \cos h \cos \psi. \qquad (2)$$

Under the assumption of anisotropic irradiance distribution over the sky hemisphere, equation 1 can not be integrated analytically because of the difficulty in obtaining $I(h,\psi)$. An approximation approach is proposed here. For a slope without surrounding terrain shading, its diffuse radiation D_s can always be expressed as

$$D_s = 0.5 D_h (1 + \cos \alpha) \Psi(n, \alpha, Z, \psi_\bullet - \psi_s)$$

$$= D_{os} \Psi(n, \alpha, Z, \psi_\bullet - \psi_s) \qquad (3)$$

where D_{os} is the slope diffuse radiation without terrain shading, determined by isotropic model and $\Psi(n, \alpha, Z, \psi_\bullet - \psi_s)$ is defined as correction function for anisotropic sky radiance distribution, which is affected by cloud amount (n), slope angle (α), solar zenith angle (Z) and the relative azimuth of the sun and slope ($\psi_\bullet - \psi_s$).

For a slope with surrounding terrain shading, its diffuse radiation D_s' can also be expressed as

$$D_s' = D_{os}' \Psi(n, \alpha, Z, \psi_\bullet - \psi_s) \qquad (4)$$

where D_{os}' is the slope diffuse radiation with surrounding terrain shading, determined by isotropic model. It is reasonable to assume that $\Psi(n, \alpha, Z, \psi_\bullet - \psi_s)$ without shading

equals (or approximates) the $\Psi(n, \alpha, Z, \psi_a - \psi_s)$ with terrain shading. Under this assumption, the following expression is obtained from (3) and (4)

$$\frac{D_s'}{D_s} \approx \frac{D_{os}'}{D_{os}} = \gamma_1 \tag{5}$$

where (D'_{os} / D_{os}) is defined as the local terrain shading index for sky diffuse radiation and denoted as γ_1. Then

$$\gamma_1 = \frac{D_{os}'}{D_{os}} = \frac{\int_0^{2\pi}\int_{h'(\psi)}^{\pi/2} I \cos i \cos h \, dh \, d\psi}{\int_0^{2\pi}\int_{h(\psi)}^{\pi/2} I \cos i \cos h \, dh \, d\psi} \tag{6}$$

where $h(\psi)$ in the denominator can be derived theoretically. For example, for south facing slope

$$h(\psi) = \begin{cases} 0 & 0 \le \psi \le \pi \\ \arccos\left[\cos\alpha / \left(1 - \sin^2\alpha \cos^2\psi \right)^{-0.5} \right] & \pi \le \psi \le 2\pi \end{cases} \tag{7}$$

Integrating the denominator, we can obtain

$$D_{os} = 0.5 \, \pi \, I \, (1 + \cos\alpha). \tag{8}$$

However, the $h'(\psi)$ in the numerator usually can not be given as a mathematical expression. Therefore, the numerator and denominator of equation 6 in their numerical integration forms can be written as

$$\gamma_1 = \frac{\cos\alpha \left[1 - \frac{1}{n}\sum_{i=1}^{n} \sin^2 h_i' \right] - \sin\alpha \left[\frac{1}{n}\sum_{i=1}^{n} \left(h_i' + 0.5 \sin 2h_i' - \frac{\pi}{2} \right) \left| \cos\psi_i \right| \right]}{\cos\alpha \left[1 - \frac{1}{n}\sum_{i=1}^{n} \sin^2 h_i \right] - \sin\alpha \left[\frac{1}{n}\sum_{i=1}^{n} \left(h_i + 0.5 \sin 2h_i - \frac{\pi}{2} \right) \left| \cos\psi_i \right| \right]} \tag{9}$$

Azimuth (360°) is divided into 36 equal fractions, each being 10°. Therefore, hi' and hi are respectively the surrounding terrain shading angle and slope self-shading angle in the direction (i × 10°), or (ψ_i). They can be obtained by field survey or using fine grid maps (Isard, 1983). Since $h_i' \ge h_i$, $\gamma_1 \le 1$. When there is no surrounding terrain shading, hi' =

h_i, then $\gamma_1 = 1$.

Following similar procedures, the local terrain enhancement index for ground reflection (γ_2) can also be expressed in the numerical integration form:

$$\gamma_2 = \frac{\cos\alpha\left[\frac{1}{n}\sum_{i=1}^{n}\sin^2 h_i'\right] + \sin\alpha\left[\frac{1}{n}\sum_{i=1}^{n}\left(h_i' + 0.5\sin 2h_i'\right)\left|\cos\psi_i\right|\right]}{\cos\alpha\left[\frac{1}{n}\sum_{i=1}^{n}\sin^2 h_i\right] + \sin\alpha\left[\frac{1}{n}\sum_{i=1}^{n}\left(h_i + 0.5\sin 2h_i\right)\left|\cos\psi_i\right|\right]} \qquad (10)$$

The symbols in equation 10 have the same meanings as for equation 9.

Appendix III

ERROR ANALYSIS

Any value y can be expressed as a function of a set of measurements $x_1, x_2, ..., x_n$ which have associated with them errors $\delta x_1, \delta x_2, ..., \delta x_n$, such that

$$y = f(x_1 \pm \delta x_1, x_2 \pm \delta x_2, ... x_n \pm \delta x_n). \quad (1)$$

The total error in y is then given by

$$\delta y = (\partial y/\partial x_1)\,\delta x_1 + (\partial y/\partial x_2)\,\delta x_2 + ... + (\partial y/\partial x_n)\,\delta x_n. \quad (2)$$

The probable absolute error in y is less than δy and is taken as the root mean square of equation 2

$$\delta y_{rms} = \left\{ [(\partial y/\partial x_1)\,\delta x_1]^2 + [(\partial y/\partial x_2)\,\delta x_2]^2 + ... + [(\partial y/\partial x_n)\,\delta x_n]^2 \right\}^{0.5}. \quad (3)$$

The relative error is evaluated by $\delta y_{rms}/y$ and is expressed in percentage. In this section, the error analysis for radiation balance components will be considered.

1. Errors in the Directly Measured Radiation Flux Densities

The directly measured radiation flux densities in this experiment include K↓, K_s↓, K↑, K_s↑, L↓, L_s↓, Q^*, Q_s^*, D and PAR. The flux densities are determined by

$$F = c\,m \quad (4)$$

where F denotes the flux density, c sensor calibration constant and m the measured signal from the sensor. According to equation 3, the probable absolute error in the radiation flux density measurement is given by

$$\delta F_{rms} = [(c\,\delta m)^2 + (m\,\delta c)^2]^{0.5}. \quad (5)$$

The resolution error of voltage measurement in the Campbell Scientific 21X datalogger varies with the input voltage ranges. Different ranges were used for different sensors in this experiment. Table 1 summarizes the sensors employed, calibration constants, input voltage ranges and associated resolution errors.

Table 1. Summary of Sensor and Datalogger Specifications

Radiation Component	Sensor Model	Calibration ($Wm^{-2}\ mV^{-1}$)	Input Voltage Range (mV)	21X Resolution (mV)
K↓	Eppley PSP pyranometer	106.38	± 15	± 2.0
Ks↓	Eppley PSP pyranometer	102.88	± 15	± 2.0
D	Eppley PSP pyranometer	114.03	± 15	± 2.0
K↑	Middleton CN-7 pyranometer	43.63	± 50	± 6.66
Ks↑	Middleton CN-7 pyranometer	46.49	± 50	± 6.66
PAR	Eppley PSP pyranometer with RG-695 filter	107.87	± 15	± 2.0
L↓	Eppley pyrgeometer	232.48	± 5	± 0.66
Ls↓	Eppley pyrgeometer	216.00	± 5	± 0.66
Q^*	Middleton CN-1 pyrradiometer	25.28	± 50	± 6.66
Qs^*	Middleton CN-1 pyrradiometer	54.03	± 50	± 6.66

Table 2. Error Analysis Results for Directly Measured Radiation Flux Densities

Flux density (Wm^{-2})	δx-PAR$_{rms}$ (Wm^{-2})	$\frac{\delta\text{x-PAR}_{rms}}{\text{x-PAR}}$ (%)	δD_{rms} (Wm^{-2})	δD_{rms} / D (%)	$\delta K\downarrow_{rms}$ (Wm^{-2})	$\frac{\delta K\downarrow_{rms}}{K\downarrow}$ (%)	$\delta Ks\downarrow_{rms}$ (Wm^{-2})	$\frac{\delta Ks\downarrow_{rms}}{Ks\downarrow}$ (%)	$\delta K\uparrow_{rms}$ (Wm^{-2})	$\frac{\delta K\uparrow_{rms}}{K\uparrow}$ (%)
0	0.22	—	0.23	—	0.21	—	0.21	—	0.29	—
50	0.33	0.66	0.34	0.68	0.33	0.66	0.32	0.65	2.51	5.03
100	0.54	0.54	0.55	0.55	0.54	0.54	0.54	0.54	5.01	5.01
250	1.27	0.51	1.27	0.51	1.27	0.51	1.27	0.51	12.50	5.00
500	2.51	0.50	2.51	0.50	2.51	0.50	2.51	0.50	25.02	5.00
750	3.76	0.50	3.76	0.50	3.76	0.50	3.76	0.50	37.50	5.00
1000	5.00	0.50	5.01	0.50	5.00	0.50	5.00	0.50	50.00	5.00
Flux density (Wm^{-2})	$\delta Ks\uparrow_{rms}$ (Wm^{-2})	$\frac{\delta Ks\uparrow_{rms}}{Ks\uparrow}$ (%)	$\delta L\downarrow_{rms}$ (Wm^{-2})	$\frac{\delta L\downarrow_{rms}}{L\downarrow}$ (%)	$\delta Ls\downarrow_{rms}$ (Wm^{-2})	$\frac{\delta Ls\downarrow_{rms}}{Ls\downarrow}$ (%)	δQ^*_{rms} (Wm^{-2})	$\frac{\delta Q^*_{rms}}{Q^*}$ (%)	δQs^*_{rms} (Wm^{-2})	$\frac{\delta Qs^*_{rms}}{Qs^*}$ (%)
0	0.31	—	0.15	—	0.14	—	0.17	—	0.36	—
50	2.52	5.04	0.52	1.05	0.52	1.04	2.51	5.01	2.53	5.05
100	5.01	5.01	1.01	1.01	1.01	1.01	5.00	5.00	5.01	5.01
250	12.50	5.00	2.50	1.00	2.50	1.00	12.50	5.00	12.51	5.00
500	25.00	5.00	5.00	1.00	5.02	1.00	25.00	5.00	25.00	5.00
750	37.50	5.00	7.50	1.00	7.50	1.00	37.50	5.00	37.50	5.00
1000	50.00	5.00	—	—	—	—	50.00	5.00	50.00	5.00

Errors in radiation sensor calibration arises as a result of deviations from the theoretical linear response of the sensor to changes in radiative flux density. The calibration error associated with a radiation sensor is usually expressed as a percentage of the radiative flux density being measured. For a Eppley PSP pyranometer, the manufacturer's specification of calibration error is ±0.5%. For Eppley pyrgeometer, it is ±1.0%. For Middleton CN-7 pyrradiometers and Middleton CN-1 pyrradiometers the calibration errors are assumed to be ±5%.

The calculated probable absolute errors and relative errors for a range of radiation flux density values are presented in Table 2. The results show that the error introduced by voltage measurement is only significant at low flux densities. When the flux densities are higher, the error is primarily due to sensor calibration errors.

2. Error in L↑ Measurement

Two approaches can be used in determining L↑. One is residual approach and the other is from Stefan-Boltzmann law.

(1) Error in the residual approach

The residual approach used to determine L↑ accumulates errors from other measured radiation balance components. From equation 3.1 L↑ is determined by

$$L\uparrow = K\downarrow - K\uparrow + L\downarrow - Q^* \qquad (6)$$

the probable absolute error in L↑ is given by

$$\delta L\uparrow_{rms} = [\,(\delta K\downarrow_{rms})^2 + (\delta K\uparrow_{rms})^2 + (\delta L\downarrow_{rms})^2 + (\delta Q^*_{rms})^2\,]^{0.5}. \qquad (7)$$

Since the calculated L↑ is not necessarily associated with one unique set of measured radiation flux densities, it is impossible to assign a specific error to a specific L↑ value. Here the measured half-hour average values of radiation flux densities on July 21 is used for the error analysis. The results are presented in Table 3. Table 3 shows that the error in calculated L↑ is primarily attributed to the error in Q^* measurement. However, when K↑

Table 3. Error Analysis Results for $L\uparrow$ by Residual Method (July 21, 1989)

Time (h, MDT)	$K\downarrow$	$\delta K\downarrow_{rms}$	$K\uparrow$	$\delta K\uparrow_{rms}$	Q^*	δQ^*_{rms}	$L\downarrow$	$\delta L\downarrow_{rms}$	$L\uparrow$	$\delta L\uparrow_{rms}$	$\delta L\uparrow_{rms}/L\uparrow$
06:30	27.2	0.25	9.0	0.54	-101.0	5.05	230.4	2.31	399.6	5.59	1.60%
08:00	252.0	1.28	56.0	2.82	74.0	3.70	233.4	2.34	355.4	5.36	1.51%
09:30	518.0	2.60	97.7	4.89	302.4	15.10	242.0	2.43	360.1	16.27	4.52%
11:00	750.0	3.76	130.6	6.54	488.6	24.43	257.8	2.58	388.6	25.69	6.61%
12:30	910.0	4.56	155.7	7.79	607.3	30.37	265.3	2.66	412.3	31.79	7.71%

becomes larger, the error in K↑ measurement will also be a major source for the error in L↑.

(2) Error in L↑ calculated by the Stefan-Boltzmann law

The Stefan-Boltzmann law can be expressed as

$$L\uparrow = \varepsilon \sigma T_s^4 . \qquad (8)$$

By differentiating the Stefan-Boltzmann equation, the probable absolute error in L↑ is expressed as

$$\delta L\uparrow_{rms} = [\ (\sigma T_s^4 \delta\varepsilon)^2 + (4 \varepsilon \sigma T_s^3 \delta T_s)^2 + (\varepsilon T_s^4 \delta\sigma)^2\ ]^{0.5}. \qquad (9)$$

Stefan-Boltzmann constant comes from experiments, it should have a small error. But for the convenience of this analysis, errors arising from the uncertainty of Stefan-Boltzmann constant are ignored. Hence the main error sources are error in surface emissivity estimation and error in surface temperature measurement

$$\delta L\uparrow_{rms} = [\ (\sigma T_s^4 \delta\varepsilon)^2 + (4 \varepsilon \sigma T_s^3 \delta T_s)^2 . \qquad (10)$$

For this analysis, the relative error in the estimated surface emissivity was assumed to be ±10%. Assessment of error in T_s measurement is presented in the next section. For current analysis, a range of possible error is assumed for T_s: ±1.0°C, ±5.0°C and ±10.0°C. The calculated results over a range of surface temperatures are tabulated in Table 4.

3. Error in T_s Measurement

Assessment of error in T_s measurement is difficult. Errors arise from the temperature sensor calibration, the resolution error in the data system and error due to radiative heating of the sensor. Also related is the problem of determining representative area surface temperatures from individual sensor placed on the surface. Nevertheless, if only the errors from calibration constant and resolution error are considered, quantitative error analysis is possible. The probable absolute error in T_s is given by

$$\delta T_{s_{rms}} = [(c \delta m)^2 + (m \delta c)^2]^{0.5} . \qquad (11)$$

Table 4. Error Analysis Results for $L\uparrow$ by Stefan-Boltzmann Equation

Ts (C)	Ts (K)	$L\uparrow$ (Wm^{-2})	$\delta Ts = \pm 1.0$ °C		$\delta Ts = \pm 5.0$ °C		$\delta Ts = \pm 10.0$ °C	
			$\delta L\uparrow_{rms}$ (Wm^{-2})	$\delta L\uparrow_{rms} / L\uparrow$ (%)	$\delta L\uparrow_{rms}$ (Wm^{-2})	$\delta L\uparrow_{rms} / L\uparrow$ (%)	$\delta L\uparrow_{rms}$ (Wm^{-2})	$\delta L\uparrow_{rms} / L\uparrow$ (%)
-5	268.2	275.3	27.8	10.1	34.3	12.5	50.6	18.2
0	273.2	296.4	30.0	10.1	36.7	12.4	52.5	17.7
10	283.2	342.2	34.6	10.1	41.9	12.3	59.2	17.3
20	293.2	393.2	39.7	10.1	47.6	12.1	66.5	16.9
30	303.2	449.6	45.3	10.1	53.9	12.0	74.4	16.5
40	313.2	511.9	51.6	10.1	60.7	11.9	83.0	16.2

Note: $L\uparrow$ is calculated with $\varepsilon = 0.95$.

Table 5. Error Analysis for Ts

Ts (C)	dTs_{rms}(C)	dTs_{rms} / Ts (%)
0	0.0056	--
5	0.0503	1.01
10	0.1002	1.00
20	0.2001	1.00
30	0.3001	1.00
40	0.4000	1.00

For a copper-constantan thermocouple, $c = 8.503\ ^{\circ}C\ mV^{-1}$. δc is assumed as the 1% slope error. For the 21X datalogger, over the range of voltage measurement used, $\delta m = 0.66\ \mu V$. The calculated results are tabulated in Table 5. From the analysis, it is clear that the error from resolution error is only slightly significant in low temperatures and it can be ignored. The calibration error is always important. However, the error of T_s in field arises mostly from radiative heating of the thermocouple and representativeness of the area surface temperature. These factors are not considered and remain the most troublesome.

REFERENCES

Bailey, W. G., Weick, E. J. and Bowers, J. D., 1989: The radiation balance of alpine tundra, Plateau Mountain, Alberta, Canada. *Arctic and Alpine Research,* 21: 126-134.

Barry, R. G., 1981: *Mountain Weather and Climate.* New York, Methuen, 313 pp.

Berdahl, P. and Martin, M., 1984: Emissivity of clear skies. *Solar Energy,* 32: 663-664.

Blumen, W., 1990: *Atmospheric Processes over Complex Terrain.* American Meteorological Society, Boston, 323 pp.

Bolz, H. M., 1949: Die abhangigkeit der infraroten gegenstrahlung von der bewolkung. *Zeitschrift fur Meteorologie,* 3: 201-203.

Bowers, J. D., 1988: *Surface Radiation and Energy Balance of an Alpine Tundra, Plateau Mountain, Southwestern Alberta, Canada.* M.Sc. thesis, Simon Fraser University, 200pp.

Bristow, K. L., Campbell, G. S. and Saxton, K. E., 1985: An equation for separating daily solar irradiation into direct and diffuse components. *Agricultural and Forest Meteorology,* 35: 123-131.

Brunt, D., 1932: Notes on radiation in the atmosphere. *Quarterly Journal of Royal Meteorological Society,* 58: 389-420.

Brutsaert, W., 1975: On a derivable formula for longwave radiation from clear skies. *Water Resources Research,* 11: 742-744.

Buffo, J., Fritschen, L. J. and Murphy, J. L., 1972: *Direct solar radiation on various slopes from 0 - 60 degrees North latitude,* USDA Forest Serv. Res. Pap. PNW-142. Pacific Northwest Forest and Range Experiment Station, Portland, Oregon, 74 pp.

Buglar, J. W., 1977: The determination of hourly insolation on an inclined plane using a diffuse irradiance model based on hourly measured global horizontal insolation. *Solar Energy,* 19: 477-491.

Carroll, J. J., 1985: Global transmissivity and diffuse fraction of solar radiation for clear and cloudy skies as measured and as predicted by bulk transmissivity models. *Solar Energy*, 35: 105-118.

Choudhury, B. J. and Chang, A. T. C., 1981: On the angular radiation of solar reflectance of snow. *Journal of Hydrology*, 102: 409-426.

Coombes, C. A. and Harrison, A. W., 1988: Angular distribution of overcast sky short wavelength radiance. *Solar Energy*, 40: 161-166.

Davies, J. A., 1967: A note on the relationship between net radiation and solar radiation. *Quarterly Journal of Royal Meteorological Society*, 93: 109-115.

Davies, J. A. and McKay, D. C., 1982: Estimating solar irradiation components. *Solar Energy*, 29: 55-64.

Davies, J. A., McKay, D. C., Luciani, G. and Abdel-Wahab, 1988: Validation of models estimating solar radiation on horizontal surface, IEA, Solar Heating and Cooling Programme Task IX Final Report, Atmospheric Environment Service, Downsview, Ontario, Canada.

Dirmhirn, I. and Eaton, F. D., 1975: Some characteristics of the albedo of snow. *Journal of Applied Meteorology*, 14: 375-379.

Dozier, J. and Outcalt, S. I., 1979: An approach toward energy balance simulation over rugged terrain. *Geographical Analysis*, 11: 65-85.

Eaton, F. D. and Dirmhirn, I., 1979: Reflected irradiance indicatrices of natural surfaces and their effect on albedo. *Applied Optics*, 18: 994-1008.

Erbs, D. G., Klein, S. A. and Duffie, J. A., 1982: Estimation of the diffuse radiation fraction for hourly, daily and monthly-average global radiation. *Solar Energy*, 28: 293-302.

Flint, A. L. and Childs, S. W., 1987: Calculation of solar radiation in mountainous terrain. *Agricultural and Forest Meteorology*, 40: 233-249.

Fritschen, L. J., 1967: Net and solar radiation relations over irrigated field crops. *Agricultural Meteorology*, 4: 55-62.

Fu, B., 1983: *Mountain climate*. Science Press, Beijing, 270 pp.

Garnier, B. J. and Ohmura, A., 1968: A method of calculating the direct shortwave radiation income of slopes. *Journal of Applied Meteorology*, 7: 796-800.

Halbsguth, G., Kerschgens, M. J., Kraus, H., Meindl, G. and Schaller, E., 1984: Energy flux in an alpine valley. *Arch. Meteorol. Geophys. Bioklimatol.*, 33(B): 11-20.

Hay, J. E., 1971: Computation model for radiative fluxes. *Journal of Hydrology (N.Z.)*, 10: 36-48.

Hay, J. E., 1977: *An analysis of solar radiation data for selected locations in Canada.* Climatological Studies No.32, Atmospheric Environmental Service, Toronto, 158 pp.

Hay, J. E., 1979: *A study of shortwave radiation on horizontal surfaces*. Final Report, Contract Serial Number OSB78 00053, Atmospheric Environment Service, Toronto, 140 pp.

Hay, J. E., 1986: Calculation of solar irradiance for inclined surfaces: validation of selected hourly and daily models. *Atmosphere-Ocean*, 24: 16-41.

Hay, J. E. and Davies J. A., 1980: Calculation of solar radiation incident on an inclined surface. *Proceedings First Canadian Solar Radiation Data Workshop*, Atmospheric Environment Service, Toronto, 59-72.

Hay, J. E. and McKay, D. C., 1985: Estimating solar irradiance on inclined surfaces: a review and assessment of methodologies. *International Journal of Solar Energy*, 3: 203-240.

Hay, J. E. and McKay, D. C., 1987: *Calculation of solar irradiance for inclined surfaces: verification of models which use hourly and daily data.* International Energy Agency Task IX, subtask b, Final Report, AES, Downsview, Ontario.

Hooper, F. C. and Brunger, A. P., 1980: A model for the angular distribution of sky radiance. *Journal of Solar Energy Engineering*, 102: 196-202.

Idso, S. B., 1981: A set of equations for full spectrum and 8-14 μm and 10.5-12.5 μm thermal radiation from cloudless skies.*Water Resources Research*, 17: 295-304.

Idso, S. B. and Jackson, R. D., 1969: Thermal radiation from the atmosphere. *Journal of Geophysical Research*, 74: 5397-5403.

Ineichen, P., Guisan, O. and Perez, R., 1990: Ground-reflected radiation and albedo. *Solar Energy*, 44: 207-214.

International Energy Agency, 1978: *An introduction to meteorological measurements and data. Handling for solar energy applications, Hand-book.* International Energy Agency, Dept. of Energy of USA, Washington D.C.

Iqbal, M., 1980: Prediction of hourly diffuse solar radiation from measured global radiation on a horizontal surface. *Solar Energy*, 24: 491-503.

Isard, S. A., 1983: Estimating potential direct insolation to alpine terrain. *Arctic and Alpine Research*, 15: 77-89.

Isard, S. A., 1986: Evaluation of models for predicting insolation on slopes within the Colorado alpine tundra. *Solar Energy*, 36: 559-564.

Isard, S. A., 1989: Topoclimate controls in an alpine fellfield and their ecological significance. *Physical Geography*, 10: 13-31.

Jeter, S.M. and Balaras, C.A., 1990: Development of improved solar radiation models for predicting beam transmittance. *Solar Energy*, 44: 149-156.

Kasten, F., 1966: A new table and approximation formula for the relative optical air mass. *Arch. Meteorol. Geophys. Bioklimatol.*, 14(B): 206-223.

Kierkus, W. T. and Colborne, W. G., 1989: Diffuse solar radiation: daily and monthly values as affected by snow cover. *Solar Energy*, 42: 143-147.

Klucher, T. M., 1979: Evaluation of models to predict insolation on tilted surfaces. *Solar Energy*, 23: 111-119.

Kondratyev, K. Ya., 1969: *Radiation in the Atmosphere.* Academic Press, New York, 912pp.

Kondratyev, K. Ya., 1977: *Radiation regime of inclined surfaces*. Technical Note No.152. World Meteorological Organization, WMO-No.467, Geneva, 82 pp.

Latimer, E. F., 1972: *Radiation Measurement. IFYGL,* Technical Manual Series No.2, Environment Canada, 53 pp.

LeDrew, E. F., 1975: The estimation of clear sky atmospheric emittance at high altitudes. *Arctic and Alpine Research,* 7: 227-236.

Liu, B. and Jordan, R., 1960: The interrelationship and characteristic distribution of direct, diffuse and total solar radiation. *Solar Energy*, 4: 1-19.

Loudon, A. G., 1967: The interpretation of solar radiation measurements for building problems, sunlight in buildings. *Proceedings of C.I.E. Conference*, Bouwcentrum, Rotterdam, 111-118.

Lougeay, R. and Brazel, A., 1982: A preliminary test of atmospheric emittance equations at high altitude, *Arch. Meteor. Geophys. Bioclimotol.*, 30(B): 227-237.

Marcus, M. G., Brazel, A. J., Lougeay, R. and Hyers, A. D., 1981: Longwave radiation enhancement by cirque wall emittance, Front Range, Colorado. In Brazel, A. J. (ed), *Research Papers in Climatology*, Department of Geography, Arizona State University, 21-42.

Marks, D. and Dozier, J., 1979: A clear-sky longwave radiation model for remote alpine areas. *Arch. Meteor. Geophys. Bioclimotol.*, 27(B): 159-178.

Maxwell, E.L., 1987: *A quasi-physical model for converting hourly global horizontal to direct normal insolation.* Proceedings of the ASES Annual Conference, Portland, OR. 35-40.

Miller, D. H. 1981: *Energy at the Surface of the Earth,* Academic Press, 516 pp.

Monteith, J. L., 1962: Attenuation of solar radiation: a climatological study. *Quarterly Journal of Royal Meteorological Society,* 88: 508-521.

Muller, H., 1985: On the radiation budget in the Alps. *Journal of Climatology,* 5: 445-462.

Munro, D. S. and Young, G. J., 1982: An operational net shortwave radiation model for glacier basins. *Water Resources Research,* 18: 220-230.

Murray, F. W., 1967: On the computation of saturation vapour pressure. *Journal of Applied Meteorology,* 6: 203-204.

Nkemdirim, L. C., 1972: A note on the albedo of surfaces. *Journal of Applied Meteorology,* 11: 867-874.

Nkemdirim, L. C., 1973: Radiative flux relations over crops. *Agricultural Meteorology,* 11: 229-242.

Oke, T. R., 1987: *Boundary Layer Climate.* Methuen, 435 pp.

Olyphant, G. A., 1984: Insolation topoclimates and potential ablation in alpine snow accumulation basins: Front Range, Colorado. *Water Resources Research,* 20: 491-498.

Olyphant, G. A., 1986a: Longwave radiation in mountainous areas and its influence on the energy balance of alpine snowfields. *Water Resources Research,* 22: 62-66.

Olyphant, G. A., 1986b: The components of incoming radiation within a mid-latitude alpine watershed during the snow melt season. *Arctic and Alpine Research,* 18: 163-169.

Orgill, J. F. and Hollands, K. G., 1977: Correlation equation for hourly diffuse radiation on a horizontal surface. *Solar Energy,* 19: 357-359.

Page, J. K., 1987: Methods for the estimation of solar energy on vertical and inclined surfaces. *Proceedings 5th Course on Solar Energy Conversion.* Department of Physics, University of Waterloo, Canada, 37-99.

Paltridge, G. W. and Platt, C. M. R., 1976: *Radiation Processes in Meteorology and Climatology.* Elsevier, Amsterdam, 318 pp.

Pereira, A. R., Machado, E. C. and de Camargo, M. B. P., 1982: Solar radiation regime in three cassava canopies. *Agricultural Meteorology,* 26: 1-10.

Perez, R., Seals, R., Ineichen, P., Stewart, R. and Menicucci, D., 1987: A new simplified version of the Perez diffuse irradiance model for tilted surfaces. *Solar Energy,* 39: 221-231.

Perez, R., Seals, R., Zelenka, A. and Ineichen, P., 1990: Climatic evaluation of models that predict hourly direct irradiance from hourly global irradiance: Prospects for performance improvements. *Solar Energy,* 44: 99-108.

Perez, R., Stewart, R, Arbogast, C., Seals, R. and Scott, T., 1983: An anisotropic hourly diffuse radiation model for sloping surfaces: description, performance validation, site dependance evaluation. *Solar Energy,* 36: 481-497.

Price, L. W., 1981: *Mountains and Man.* University of California Press, 506 pp.

Price, A. G., 1988: Prediction of snowmelt rates in a deciduous forest. *Journal of Hydrology,* 101: 145-157.

Puri, V. M., Jiminez, R. and Menzer, M., 1980: Total and non-isotropic diffuse insolation on tilted surfaces. *Solar Energy,* 25: 85-90.

Rao, C. R. N., Bradley, W. A. and Lee, T. Y., 1984: The diffuse component of the daily global solar irradiation at Corvallis, Oregon (USA). *Solar Energy,* 32: 637-641.

Reindl, D. T., Beckman, W. A., Duffie, J. A., 1990: Evaluation of hourly tilted surface radiation models. *Solar Energy,* 45: 9-17.

Ripley, E. A. and Redmann, R. E., 1976: Grassland. In Monteith, J. L. (ed.), *Vegetation and the Atmosphere, Vol. 2: Case Studies.* New York, Academic Press, 349-398.

Robinson, G. D., 1947: Notes on the measurement and estimation of atmospheric radiation. *Quarterly Journal of Royal Meteorological Society,* 73: 127-150.

Robinson, G. D., 1950: Notes on the measurement and estimation of atmospheric radiation. *Quarterly Journal of Royal Meteorological Society,* 76: 37-51.

Rouse, W. R., 1984: Microclimate at arctic tree line. 1. Radiation balance of tundra and forest. *Water Resources Research,* 20: 57-66.

Rowe, C. M. and Willmott, C. J., 1984: Solar irradiance on flat-plate collectors in urban environments. *Solar Energy*, 33: 343-357.

Saunders, I. R., 1990: *Radiation and Energy Budgets of Alpine Tundra, Scout Mountain, Southern British Columbia, Canada*. Ph.D. thesis, Simon Fraser University, 201 pp.

Sherry, J. E. and Justus, C. G., 1984: A simple hourly all-sky solar radiation model based on meteorological parameters. *Solar Energy*, 32: 195-204.

Skartveit, A. and Olseth, J.A., 1987: A model for the diffuse fraction of hourly global radiation. *Solar Energy*, 38: 271-274.

Stigter, C. J. and Musabilha, V. M. M., 1982: The conservative ratio of photosynthetically active to total radiation in the tropics. *Journal of Applied Ecology*, 19: 853-858.

Storr, D., 1972: Estimating effective net radiation from a mountainous watershed. *Boundary-Layer Meteorology*, 3: 3-14.

Swinbank, W. C.,1963: Longwave radiation from clear skies. *Quarterly Journal of Royal Meteorological Society*, 89: 338-348.

Szeicz, G., 1974: Solar radiation for plant growth. *Journal of Applied Ecology*, 11: 617-636.

Temps, R. C. and Coulson, K. L., 1977: Solar radiation incident upon slopes of different orientations. *Solar Energy*, 19: 179-184.

Terjung, W. H., Kickert, R. N., Potter, G. L. and Swarts, S. W., 1969: Terrestrial, atmospheric and solar radiation fluxes on a high desert mountain in mid-July: White Mountain Peak, California. *Solar Energy*, 12: 363-375.

Unsworth, M. H., 1975: Longwave radiation at the ground: II: Geometry of interception by slope, solids, and obstructed plane. *Quarterly Journal of Royal Meteorological Society*, 101: 25-34.

Unsworth, M. H. and Monteith, J. L., 1975: Longwave radiation at the ground: I: Angular distribution of incoming radiation. *Quarterly Journal of Royal Meteorological Society*, 101: 13-24.

Walton, D. W. H., 1982: Instruments for measuring biological microclimates for terrestrial habitats in polar and high alpine regions: a review. *Arctic and Alpine Research,* 14: 275-286.

Weiss, A and Norman, J. M., 1985: Partitioning solar radiation into direct and diffuse, visible and near-infrared components. *Agricultural and Forest Meteorology*, 34: 205-213.

Whiteman, C. D., Allwine, K. J., Fritschen, L. J., Orgill, M. M. and Simpson, J. R., 1989: Deep valley radiation and surface energy budget microclimates, part I: radiation. *Journal of Applied Meteorology,* 28: 414-426.

Williams, L. D., Barry, R. G. and Andrews, J. T., 1972: Application of computed global radiation forecast of high relief. *Journal of Applied Meteorology,* 11: 526-533.

Willmott, C. J., 1982: Some comments on the evaluation of model performance. *Bulletin American Meteorological Society*, 63: 1309-1313.

Yefimova, N. A., 1972: Geographical distribution of the sums of photosynthetically active radiation. *Soviet Geography,* 66-74.